Alma Mater Studiorum - Università di Bologna

SCUOLA DI SCIENZE
Dipartimento di Chimica Industriale
"Toso Montanari"

Corso di Laurea Magistrale in
Chimica Industriale
Classe LM-71 - Scienze e Tecnologie della Chimica Industriale

Studying the alignment of 5-cyanobiphenyl on a polydimethylsiloxane surface through Molecular Dynamics simulations

Tesi di laurea sperimentale

CANDIDATO
Matteo Babbi

RELATORE
Chiar.mo Prof. Claudio Zannoni

CORRELATORE
Lara Querciagrossa

Anno Accademico 2017/2018

Contents

Abstract

In the last decades, computer technology has undergone a drastic development, which was absolutely unpredictable at the half of the twentieth century. Just think about that nowadays a little pocket-size object as a smartphone is much more powerful than a 70's computer which needed a whole room to contain it for how big it was, despite of its ridiculous performances, we could say at present. Technological devices are continuously getting smaller and more effective, becoming able to fulfill more and more complex tasks. Almost every field has taken advantage of this improvement, leading to a radical change of our lives. Scientific research has particularly benefited of informatics, in a way that no one could imagine, thanks to the advent of supercomputers. The traditional laboratory experiment has in many cases been replaced by virtual simulations through powerful computational engines. These allowed to well reproduce, employing the suitable algorithms, what happens in real life. The advantages brought by this new way of making research are various. Certainly, having your whole laboratory behind a computer display makes you avoid the costs related to the instrumentation you need for a real experiment. All the risks which could arise from the handling of potentially dangerous substances or tools are completely cut out. Moreover, experiments that could be difficult to follow, due for example to the size (too small) of the sample or its complexity, are potentially feasible through a simulated experiment. Nevertheless, computer resources are not for free: the more accurate the simulations results, the more powerful, and so more expensive, machines are needed. Virtual research has anyway become widespread thanks to the undeniable benefits it brought, and chemistry is one of the main fields that make use of it. The classical image of the chemist with the white lab coat and the protecting glasses has recently been juxtaposed by the new image of the computational chemist, pioneer of the emergent branch of computational chemistry. The task of this unusual kind of scientist is, as a first step, to develop methods to faithfully represent a phenomenon which occurs in the reality in the digital dimension, that means modeling atoms or molecules and parameterizing their interactions and, as

second step, try to explain the phenomenon observed through virtual analysis. It is quite clear that computational techniques play an important role in those cases where the systems studied are particularly complex: the most common example is the study of proteins, which are very sophisticated molecules, often composed of hundred thousands atoms, assuming spatial conformations that play a fundamental role in determining their interaction with the substrate, and so their catalytic function. It is no coincidence if biochemistry was the first branch of chemistry to make use of the powerful tool of computer simulations, as underlined by the fact that in many of the softwares available a lot of terms bring a name which refers to this kind of systems. Afterwards, simulations spread in other fields of chemistry. For 40 years, at the University of Bologna, a group of researchers coordinated by professor Claudio Zannoni has been studying liquid crystals (LCs) by employing computational techniques. Through the years, they have developed effective models of these interesting, and still far from being completely understood, systems, becoming a point of reference for the other groups dealing with liquid crystals all over the world. They were able to reproduce with simulations important features of some molecules presenting the liquid crystalline phase, such as transition temperature [1]. Then they focused on the interactions that these molecules have with different kinds of surface, and how these interactions affect the alignment of liquid crystals. This is a crucial point if we take into account that the technological importance of liquid crystals is due to the possibility for them to exhibit, in some conditions, a directional order, while preserving positional freedom, typical of normal liquid phase. For example, liquid crystals have been employed in the development of displays [2] thanks to the fact that polarized light is allowed to be transmitted or not through a film of these molecules depending on their alignment with respect to polarizing direction, and the alignment can be easily controlled through an external stimulus, such as an electric field. Nevertheless, also the surface in contact with liquid crystal molecules can affect the orientation of these ones. Zannoni and his group studied the behaviour of liquid crystals in contact with different kinds of surfaces, from silica, either amorphous and crystalline [3], to organic self assembled monolayers (SAMs) [4] and even some common polymers, such as polymethyl-methacrylate (PMMA) and polystyrene (PS) [5]. Anyway, a library of typical surfaces is still far from being complete, and a lot of work must be done to investigate the cases which have not been analyzed yet. A hole that must be filled is represented by polydimethylsiloxane (PDMS), a polymer on which the interest of industry has enormously grown up in the last years, thanks to its peculiar features, allowing it to be employed in many fields of applications. It has been

observed experimentally that PDMS causes 4-cyano-4'-pentylbiphenyl (well known as 5CB), one of the most common liquid crystal molecules, to align homeotropically (i.e. perpendicular) with respect to a surface made of this polymer [6, 7, 8]. Even though some hypothesis have been presented to rationalize the effect, a clear explanation of this phenomenon has not been given yet. The dissertation that follows shows the work I did during my internship in the group of professor Zannoni at the department of Industrial Chemistry *"Toso Montanari"*, University of Bologna. The challenge that I had to tackle was to investigate, via Molecular Dynamics (MD) simulations, the reasons of 5CB homeotropic alignment on a PDMS surface, as the group had previously done for other surfaces.

Chapter 1

Introduction

1.1 Computer Simulations

The great challenge that computational chemistry has to face is the development of a description of reality through calculation resources that are not unlimited. This means that an infinitely accurate reproduction of real phenomena is not possible; approximations are necessary in order to study a system via computer simulations. First of all, a degree of detail in particles representation must be chosen, according to the accuracy one needs [9]. A better and deeper description of a system is reached moving from lattice models to molecular models to atomistic models. Of course, this is not costless, but affects the calculations efforts required. Depending on the aspects one wants to study, different approaches are possible. If the aim of the study is to compute the properties of a single molecule, such as electronic density, dipole moment, orbitals occupation and so on, quantum mechanics (QM) methods represent the best choice, giving the most complete and accurate results. These methods consist of the approximated solution, in some way, of the Schrödinger's equation, obtaining the eigenstates of the system, and hence all the other properties. QM methods are not the only possibility: for systems of many molecules and condensed phase, a classical approach is also feasible. In this case, atoms and molecules are treated as classical objects (even if their properties are obtained by QM methods), subjected to Newtonian laws [10]. While for QM methods it is not possible to study systems made of more than a few molecules, because of the huge calculation efforts, classical methods allow to study both a single molecule or a group of molecules. The choice is obviously driven by the aim of the study. In classical methods it is necessary to create a virtual model of atoms constituting a molecule, meaning that every kind of interaction has to be quantified in terms

of energy. This difficult task is accomplished by building a Force Field (FF) [11]. This is a set of parameters that describe the entity of the bonding and non-bonding interactions among atoms involved in a simulation, that are stretching, bending, torsion, electrostatic and dispersion forces. Each of these interactions contributes to the overall energy of the system. The analytical forms of the various potentials are not univocal, but can vary from a simulation software to another. However, in general two kinds of parameters are required for intramolecular terms, force constants and equilibrium values (those for which energy is a minimum). In the next section, the form of the FF employed in the simulation program NAMD [12] (the one I used for my research) will be described in detail. A good FF should be able to reproduce the properties of a molecule as well as possible. Force Field parameters are obtained by quantum mechanics calculations. A deeper overview on the procedure adopted will be shown in Chapter 5, where the method for the calculation of torsion parameters of the $Si\text{-}CH_2\text{-}CH_2\text{-}Si$ dihedral of cross-linked PDMS is discussed.

When the evolution of a system of particles in time has to be studied, a crucial point resides in how to compute the movement of particles in time or, in other words, their trajectories. As it is obvious, it would be not possible to follow trajectories in a continuous manner; instead time must be sampled, meaning that a photograph of the system is taken with a certain frequency [11]. What happens between two snapshots is unknown, but it does not matter if the frequency of sampling is small enough. A question that could arise is how to follow a trajectory, i.e. how to "jump" from a certain step to the following one. One way is purely stochastic: the system, that is in a certain configuration, will evolve into a new configuration according to the probability of all possible events to occur. The event endowed with the highest probability, will be the most probable one. Methods following this approach are called Monte Carlo (MC), from the name of the quarter of the little Principality of Monaco, well known for its casinos. In Figure 1.1, the typical procedure of a MC method is shown: as it can be seen, a new configuration, randomly generated, is evaluated to occur according to a probability factor (represented by a Boltzmann's factor) and hence it is accepted or discarded. In order to be effective, such a method has to grant that, regardless of the initial configuration, the algorithm must lead to the same equilibrium state after a high number of steps.

  The use of statistics is not the only possible solution to the problem of the determination of the evolution of the system in time. The phase space can also be explored with a deterministic approach, starting from a certain configuration (i.e. positions and velocities of all particles of
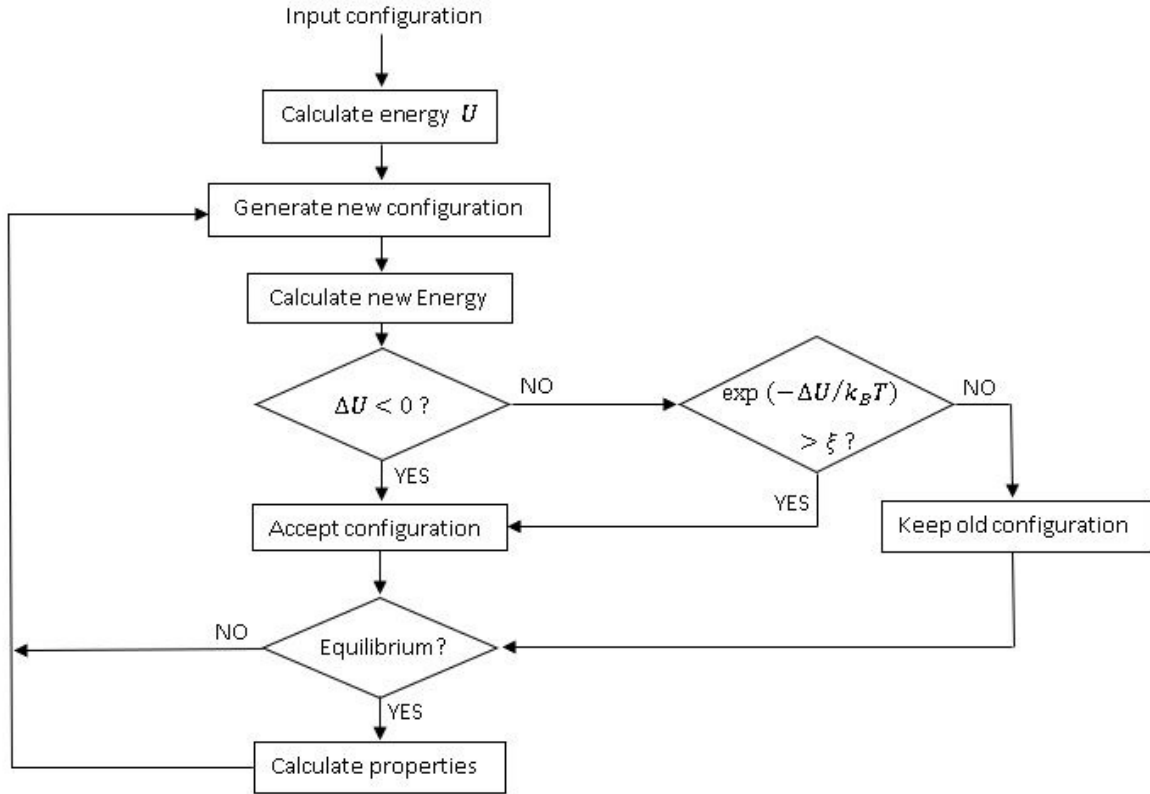
Figure 1.1: Monte Carlo flow-chart.

the sample), calculating forces and then computing the displacement of particles after a certain small time lapse through the equations of motion. Methods employing this strategy are grouped under the name of Molecular Dynamics (MD). Mathematical aspects regarding MD simulations will be treated in the next section. It should be easy to realize that MD simulations are more demanding than MC ones in terms of computer resources, since trajectory is followed solving mathematical equations, and not guessed from probability factors. Moreover, while in MC the true dynamics is not followed, and hence only static equilibrium values but not time-dependent properties, in MD techniques velocities are mandatory to be calculated in order to find the trajectory of particles. As a consequence, time-dependent properties can be obtained only using MD simulations. Apart from this difference, in both MC and MD methods, properties are computed as a mean of the property itself measured at each time step:

$$\langle A \rangle = \frac{1}{M} \sum_{j=1}^{M} A(X^{(j)}) \tag{1.1}$$

where M is the number of timesteps (i.e. the number of "snapshots") and $A(X^{(j)})$ is the value

of the property A corresponding to the configuration X of the system at the j-th timestep. The bigger is the number of timesteps, M, the more accurate is $\langle A \rangle$. In the limit of an infinite number of timesteps, the previous equation gets the form of an integral:

$$\langle A \rangle = \int dX p(X) A(X) \tag{1.2}$$

where $dX p(X)$ is the probability to find the system in the configuration $\{X, X + dX\}$. The probability $p(X)$ to find the system in a certain configuration is itself related to the energy $U(X)$ that the system has in that configuration, as stated by the equation:

$$p(X) = \frac{1}{Z_N} e^{-\frac{U(X)}{k_B T}} \tag{1.3}$$

where Z_N is a normalization factor.

Once $U(X)$ has been calculated, $p(X)$ can be computed, and then the mean properties of the system can be obtained, as stated by equation 1.2. Approximation of integrals as a sum of discrete intervals in which a property can be considered constant (discretization) is the method adopted in MD simulations, while in Monte Carlo the so-called "monkey method", as we are now going to describe, is employed for the resolution of integrals. Let us consider the case of a one-variable function $y = f(x)$ (which in turn can be represented in a plane). Imagine we want to calculate the integral $\int_a^b f(x) dx$. A pair of random numbers x_n and y_n are generated, so that $a \leq x_n \leq b$ and $\min[f(x)] \leq y_n \leq \max[f(x)]$. If $y_n \leq f(x_n)$, then we will add 1 to a variable called SUM, which is 0 at the beginning. We repeat this procedure M times. At the end of this process, the esteem of the integral is:

$$\int_a^b f(x) dx \approx \frac{SUM}{M} max[f(x)](b - a) \tag{1.4}$$

The term SUM/M represents the probability for the point $(x_n; y_n)$ to lie below the curve $f(x)$ and, if the number M of points extracted is big enough, it roughly corresponds with the ratio between the area below the curve and the total area.

Molecular Dynamics

In MD simulations, trajectories are followed by computing positions and velocities of all particles at each timestep [13]. Several algorithms have been developed in order to fulfill this nothing but easy task. From the configuration of the system at each timestep it is possible to compute a property as a mean that runs over the timesteps. As said in the previous paragraph, discretization of time is unavoidable, which means that the position $\mathbf{r}_i(t)$ and velocity $\mathbf{v}_i(t)$ of the i-th particle are replaced by $\mathbf{r}_i(n\Delta t)$ and $\mathbf{v}_i(n\Delta t)$, respectively. Figure 1.2 shows the loss of information moving from a continuous time variation to a discrete one.

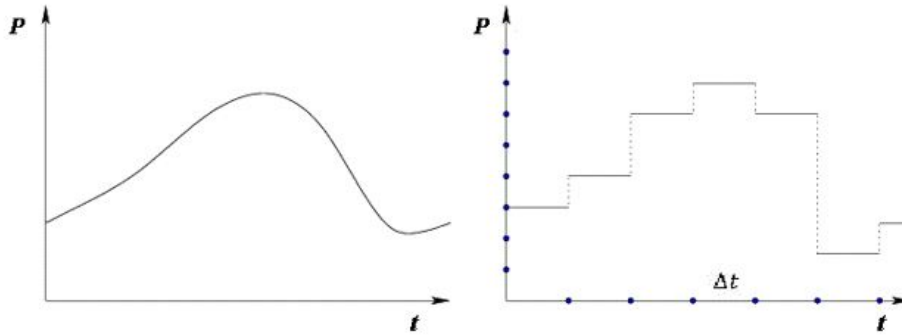The problem involved in computing a trajectory is how to calculate, starting from a certain

Figure 1.2: A generic property P followed in time continuously (left) and discretely (right).

configuration $\{\mathbf{r}_i(t), \mathbf{v}_i(t)\}$ at time t of the system studied, the configuration after a time lapse of a timestep Δt, thus $\{\mathbf{r}_i(t + \Delta t), \mathbf{v}_i(t + \Delta t)\}$. The way is to solve the equations of motion, which are differential, using a numerical algorithm such as the finite difference method. Let us consider the definition of acceleration and velocity as follows:

$$\mathbf{a}(t) = \frac{d[\mathbf{v}(t)]}{dt} \tag{1.5}$$

$$\mathbf{v}(t) = \frac{d[\mathbf{r}(t)]}{dt} \tag{1.6}$$

We can now replace these equations with the definition of derivative as the limit of the difference quotient. For example, in the case of acceleration, it becomes:

$$\mathbf{a}(t) = \lim_{\Delta t \to 0} \frac{\mathbf{v}(t + \Delta t) - \mathbf{v}(t)}{\Delta t} \tag{1.7}$$

From this equation it follows that, if Δt is small enough, then:

$$\mathbf{v}(t + \Delta t) \approx \mathbf{v}(t) + \Delta t \cdot \mathbf{a}(t) \qquad (1.8)$$

The latter approximation states that, if velocity and acceleration at a certain instant t are known, then velocity at the instant $t + \Delta t$ can be estimate. The smaller Δt is, the better the accuracy will be. Analogously for velocity, we obtain:

$$\mathbf{r}(t + \Delta t) \approx \mathbf{r}(t) + \Delta t \cdot \mathbf{v}(t) \qquad (1.9)$$

The problem connected with such a kind of algorithm is quite evident: since every iteration brings an approximation in the computation of $\mathbf{v}$ and $\mathbf{r}$, the error will be substantial after few steps. The maximum accuracy would be achieved writing $\mathbf{v}$ and $\mathbf{r}$ as Taylor's expansions with an infinite number of terms. For a general function $f(t)$ nearby $t = t_0$, it corresponds to:

$$f(t_0 + \Delta t) = f(t_0) + \Delta t \left(\frac{\delta f}{\delta t} \right)_{t_0} + \frac{(\Delta t)^2}{2!} \left(\frac{\delta^2 f}{\delta t^2} \right)_{t_0} + \frac{(\Delta t)^3}{3!} + ... + \frac{(\Delta t)^n}{n!} \left(\frac{\delta^n f}{\delta t^n} \right)_{t_0} . \quad (1.10)$$

The Taylor's expansion can be more or less truncated depending on the accuracy one wants to reach.

Let us apply the expansion to obtain an expression for $r(t + \Delta t)$. Truncating at the 2nd order (i.e. after the term containing the second derivative), we have:

$$\mathbf{r}(t + \Delta t) = \mathbf{r}(t) + \Delta t \frac{\delta \mathbf{r}(t)}{\delta t} + \frac{(\Delta t)^2}{2} \frac{\delta^2 \mathbf{r}(t)}{\delta t^2} \qquad (1.11)$$

We say that equation 1.11 has an error of the third order because it has been truncated after the term containing the second derivative. In general, the error in a Taylor's equation truncated at the n-th term, is of the $(n+1)$-th order. It is quite easy to realize that the higher the order of the error, the smaller the error is. In fact, since we are considering Δt to be an infinitesimal time lapse, it will be certainly verified that $\Delta t \ll 1$ (in natural units). For this reason, also $(\Delta t)^n$ will be much smaller than 1. In particular, the higher n is, the smaller $(\Delta t)^n$ will be. Now we know that the first derivative of position with respect to time is the velocity, while the second derivative of position with respect to time is the acceleration. Thus, the previous equation can be written as:

$$\mathbf{r}(t + \Delta t) = \mathbf{r}(t) + \Delta t \cdot \mathbf{v}(t) + \frac{(\Delta t)^2}{2} \cdot \mathbf{a}(t) \tag{1.12}$$

Analogously, it is possible to apply the expansion using $-\Delta t$ instead of Δt, obtaining the position at the previous timestep:

$$\mathbf{r}(t - \Delta t) = \mathbf{r}(t) - \Delta t \cdot \mathbf{v}(t) + \frac{(\Delta t)^2}{2} \cdot \mathbf{a}(t) - (3^{rd}Order) + (4^{th}Order) - ... + ... \tag{1.13}$$

The expansion of $\mathbf{r}(t - \Delta t)$ is similar to that of $\mathbf{r}(t + \Delta t)$, the only difference is that in the first, all signs are +, while in the second + and - alternate. If we sum member to member the Taylor's expansions of $\mathbf{r}(t - \Delta t)$ and $\mathbf{r}(t + \Delta t)$, we obtain the removal of odd order terms. The 1st, 3rd, 5th ... $(2n + 1)^{th}$ order terms will be 0. This means that we can truncate at the third order, with a 4th order error, even if we practically do not need to calculate the third order term, since it is 0.

$$\mathbf{r}(t + \Delta t) + \mathbf{r}(t - \Delta t) = 2\mathbf{r}(t) + 0 + (\Delta t)^2\mathbf{a}(t) + 0 + (4^{th}Order) \tag{1.14}$$

We can know rearrange the previous equation in order to obtain an expression for the computation of the position at the instant $t + \Delta t$:

$$\mathbf{r}(t + \Delta t) = -\mathbf{r}(t - \Delta t) + 2\mathbf{r}(t) + (\Delta t)^2 \cdot \mathbf{a}(t) + [Error \propto (\Delta t)^4] \tag{1.15}$$

The advantage is clear: we gained an order in the error, thus the approximation is more accurate with respect to the case in which we simply use the Taylor's expansion for $\mathbf{r}(t + \Delta t)$ alone (3rd order error). Such an algorithm is known as Störmer-Verlet algorithm [14]. As it can be noticed, if we want to calculate the position of a particle at the time $t + \Delta t$ we need both position at time t and $t - \Delta t$. This feature represents an inconvenience when the system is at time $t = 0$, since $\mathbf{r}(-\Delta t)$ does not exist. For this reason the Störmer-Verlet algorithm is not "self-starting", and a different approach is needed for the first step. In Figure 1.3, the mechanism of this algorithm is shown.

Acceleration is calculated using the Newton's equation $\mathbf{F} = m \cdot \mathbf{a}$. The problem is how to
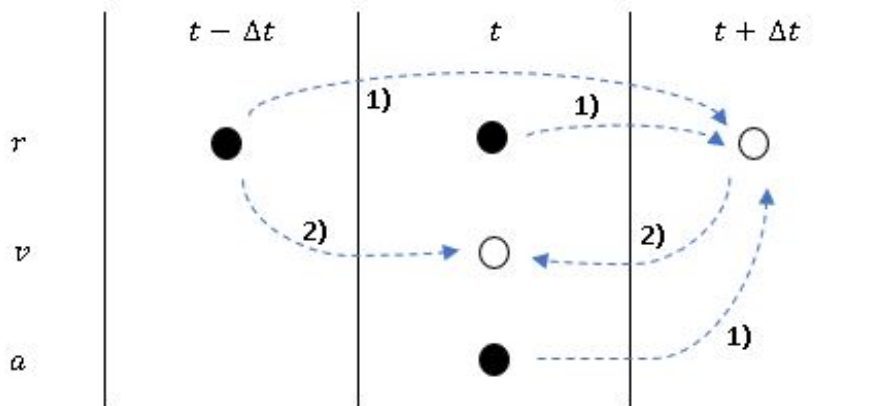
Figure 1.3: Graphical representation of Störmer-Verlet algorithm. Black circles indicates variables known at the beginning.

obtain the force acting on each particle. Since it represents a very difficult task, approximations are necessary. The main and most drastic approximation is called "pair potential": it means that particles interact with each others only in couples. For example, let us consider three particles, called A, B and C. Then consider particles A and B's positions fixed. The potential energy associated to the couple A and B does not change if C moves and changes its position. Thus, the potential energy competing to the i-th particle will be the sum of several couple contributes:

$$U_i = \sum_{j \neq i}^{M} U_{ij} \tag{1.16}$$

where M is the total number of particles and U_{ij} is the potential energy between the particles i and j.

As known form physics, the force is minus the gradient of the potential energy with respect to the position:

$$\mathbf{F} = -\nabla U(\mathbf{r}) \tag{1.17}$$

Once the force has been calculated, acceleration can be obtained through the Newton's equation.

Another feature of the Störmer-Verlet algorithm is that velocity does not appear at all, but it is esteemed afterwards through the different quotient:

$$\mathbf{v}(t) \approx \frac{\mathbf{r}(t + \Delta t) - \mathbf{r}(t - \Delta t)}{2\Delta t}. \tag{1.18}$$

As a consequence, the accuracy of the esteem on velocity is worse than that on position.

An improvement of the Störmer-Verlet algorithm is represented by the velocity Verlet algorithm, which employs Hamilton's equations instead of Newton's equation ($\mathbf{F} = m \cdot \mathbf{a}$).

$$\frac{d\mathbf{r}_i}{dt} = \dot{\mathbf{r}}_i = \frac{\mathbf{p}_i}{m_i} \tag{1.19}$$

$$\frac{d\mathbf{p}_i}{dt} = \dot{\mathbf{p}}_i = \mathbf{F}_i \tag{1.20}$$

where $\mathbf{p}_i$ is the momentum of the i-th particle.

The advantage of the velocity Verlet algorithm is that position and velocity can be obtained at the same time with the same accuracy, while the Störmer-Verlet algorithm the error on velocity esteem is bigger, due to the fact that it is calculated afterwards, as explained above. A little complication is given by the need to introduce a fictitious timestep between two instants t and $t + \Delta t$. The procedure is the following. First of all, $\mathbf{p}(t)$ evolves into $\mathbf{p}(t + \frac{1}{2}\Delta t)$ (the momentum at the fictitious time):

$$\mathbf{p}(t + \frac{1}{2}\Delta t) = \mathbf{p}(t) + \frac{1}{2}\Delta t \cdot \dot{\mathbf{p}}(t) = \mathbf{p}(t) + \frac{1}{2}\Delta t \cdot \mathbf{F}(t). \tag{1.21}$$

As second step, position is evolved from instant t to instant $t + \Delta t$:

$$\begin{aligned} \mathbf{r}(t + \Delta t) =& \mathbf{r}(t) + \Delta t \cdot \dot{\mathbf{r}}(t) + \frac{1}{2}(\Delta t)^2 \cdot \ddot{\mathbf{r}}(t) = \\ =& \mathbf{r}(t) + \Delta t \cdot \frac{\mathbf{p}(t)}{m} + \frac{1}{2}(\Delta t)^2 \cdot \frac{\mathbf{F}(t)}{m} = \\ =& \mathbf{r}(t) + \frac{\Delta t}{m}[\mathbf{p}(t) + \frac{\Delta t}{2} \cdot \mathbf{F}(t)] = \\ =& \mathbf{r}(t) + \frac{\Delta t}{m} \cdot \mathbf{p}(t + \frac{1}{2}\Delta t). \end{aligned} \tag{1.22}$$

At this point, position at time $t + \Delta t$ is known, but the momentum at that instant has still to be determined, even if $\mathbf{p}(t + \frac{1}{2}\Delta t)$ is known. From the final position $\mathbf{r}(t + \Delta t)$ it is possible to obtain the force at the instant $t + \Delta t$:

$$\mathbf{F}(t + \Delta t) = -\nabla U(\mathbf{r}). \tag{1.23}$$

Now both $\mathbf{r}(t + \Delta t)$ and $\mathbf{F}(t + \Delta t)$ are determined. Only $\mathbf{p}(t + \Delta t)$ is unknown. In order to obtain it, we will consider the reversibility of time, which means that we can run backwards across the trajectory, replacing Δt with $-\Delta t$. In practice, we compute $\mathbf{r}(t)$ considering it as $\mathbf{r}[(t + \Delta t) - \Delta t]$, through the Taylor's expansion:

$$\mathbf{r}(t) = \mathbf{r}[(t + \Delta t) - \Delta t] = \mathbf{r}(t + \Delta t) - \frac{\Delta t}{m}\mathbf{p}(t + \Delta t) + \frac{(\Delta t)^2}{2m}\mathbf{F}(t + \Delta t) \tag{1.24}$$

Summing up equation 1.24 with equation 1.22 obtained at the second step and rearranging, we finally find an expression to calculate $\mathbf{p}(t + \Delta t)$, where all terms but this one are known:

$$\cancel{\mathbf{r}(t+\Delta t)} + \cancel{\mathbf{r}(t)} = \cancel{\mathbf{r}(t)} + \cancel{\frac{\Delta t}{m}}\mathbf{p}(t + \frac{1}{2}\Delta t) + \cancel{\mathbf{r}(t+\Delta t)} - \cancel{\frac{\Delta t}{m}}\mathbf{p}(t + \Delta t) + \frac{(\Delta t)^{\cancel{2}}}{2\cancel{m}}\mathbf{F}(t + \Delta t) =$$

$$= \mathbf{p}(t + \Delta t) = \mathbf{p}(t + \frac{1}{2}\Delta t) + \frac{1}{2}\Delta t \cdot \mathbf{F}(t + \Delta t)$$

$$\tag{1.25}$$

The velocity Verlet method can be represented graphically, as shown in Figure 1.4.

When dealing with a MD simulation, it is interesting to study the spatial arrangement of particles, since it gives information about the order of the system, and hence the kind of phase that occurs in those particular conditions. The structure of a system of particles can be analyzed through the computation of the radial distribution function, $g(r)$. This function "counts" how many particles are included in a spherical shell of thickness dr distant r from a particle taken as the center (Figure 1.5).

 Thus, in some way $g(r)$ represents the density of the system at a certain distance r from the origin, but in terms of number of particles and not of mass ($g(r)$ is in fact dimensionless). Since the volume of the shell increases by enlarging the radius (i.e. moving far from the center), it
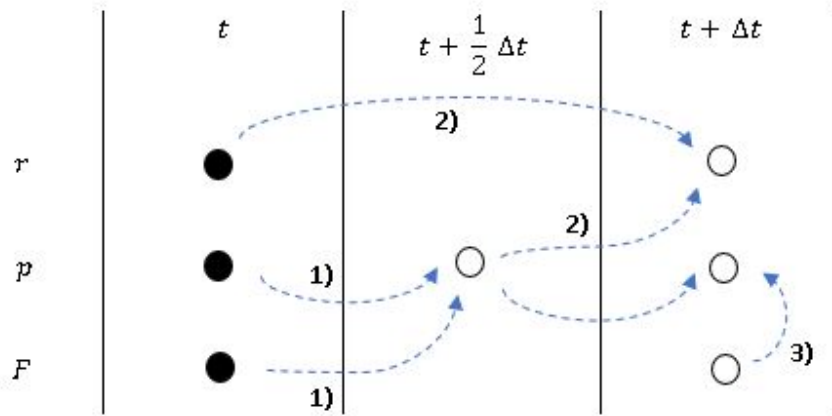
Figure 1.4: Graphical representation of velocity Verlet algorithm. Black circles indicate variables known at the beginning.
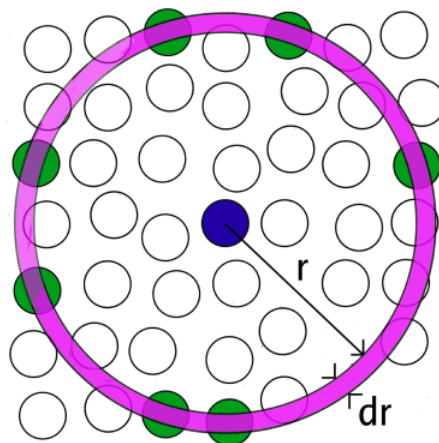

Figure 1.5: Graphical representation of radial distribution function meaning [15].

is necessary to make a sort of normalization that takes into account this factor. The solution is to divide the number of particles inside the shell of radius r for the number of particles in the shell at a distance $r \rightarrow \infty$. In fact, what is expected is that, far from the origin, correlation with the central particle is lost, and the density of particles gets constant with respect to r.

$$g(r) = \frac{\langle \rho(r) \rangle}{\langle \rho \rangle} \tag{1.26}$$

where $\rho(r) = n(r)/V(r)$ is the density at a distance r, while ρ is the density at infinite distance from the origin. The brackets indicates a mean of the density over all particles. In Figure 1.6

, typical trends of the $g(r)$ of a solid, a liquid and a gas are shown. As we can see, in all of these cases, for $r \to 0$, $g(r) = 0$. This is a universal feature of the radial distribution function, due to the fact that particles occupy a non-zero volume, so it is obvious that below a certain value of r no particle can be found, otherwise it would overlap with the central particle, which would result in a infinite potential (not possible!). In the trend of the solid, some high peaks are visible. To explain this observation we can imagine that the particle taken as the origin is surrounded by several coordination shells, each of them corresponding to a peak in the $g(r)$ plot. Between two peaks, the probability to find a particle is low, since it would collide with those of the two shells: hence, the value of $g(r)$ falls down. As r increases, the height of the peaks gets lower because the correlation with the central particles is less strong. Little by little the $g(r)$ function flattens and reaches the constant value 1. In a solid system, particles positions are fixed, and coordination shells are well defined. In a liquid, instead, particles are allowed to move, and this is the reason why coordination shells are larger than in solids. Moreover, correlation with the central particle is lost much faster. Usually only the first peak is quite high and sharp, while the successive ones are very low and wide. The more the particles are free to move, the more the curve representing $g(r)$ will be flat. Thus, we could expect that for gas phases, peaks will be almost negligible, as it is shown in Figure 1.6. Taking into account this fact, the shape of the radial distribution function trend could represent a useful tool for determining the phase of the system studied. For example, making a temperature scan, observing the g(r) at different temperatures, it is possible to determine when the phase transition occurs.

1.1.1 NAMD

As already said, my work has focused on the study of 5CB alignment on a PDMS surface employing the tool of atomistic MD simulations. The software I used for this purpose is NAMD [12], a code developed by researchers belonging to the National Institute of Health (NIH), Center for Macromolecular Modeling Bioinformatics, USA. This software was born for the study of biological systems, such as proteins, viruses, bacteria, cell membranes and so on, but its use has later spread to other fields of research too. NAMD simulations can be performed through parallel computing (i.e. the execution of the program on more than one processor at the same time), ensuring faster results, which is a fundamental feature, considering the high
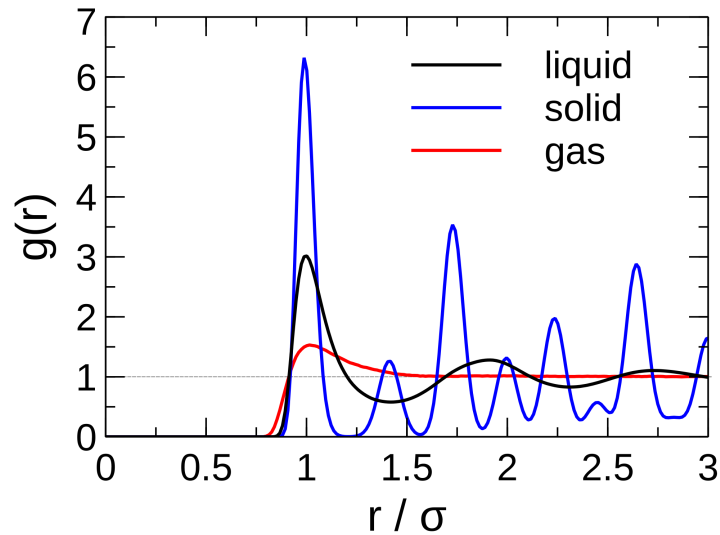
Figure 1.6: Typical radial distribution function trends of a solid (blue line), a liquid (black line) and a gas (red line) [16].

time demand that atomistic simulations require, especially in case of a high number of atoms composing the system. Regarding this aspect, a great limit of the simulation is the finite size of the sample: studying samples wider than 10^{-6} m would be almost impossible for nowadays computers, due to the huge calculation effort. It could be a problem if the aim of the simulation is to study the properties of particles in a bulk. A way to overcome this inconvenient is to adopt the periodic boundary conditions (PBC). In practice, once a simulation box, in which the particles of the sample are included, has been defined, the box is replicated in all directions so that the particles of the "mother box" are not isolated any more, but surrounded by other particles. Let us consider a particle in the "mother box": if the position of the particle is, in a cartesian coordinate system, defined as (x, y, z), then we will find a copy of it in all the points of the space with coordinates $(x + n \cdot a, y + m \cdot b, z + l \cdot c)$, where a, b and c are the box dimensions along x, y and z directions, respectively, while n, m and l are integer numbers, positive or negative. A better comprehension of PBC can be achieved looking at Figure 1.7. Periodic boundary conditions allow to compute bulk properties without increasing the amount of calculation, since the trajectories of the "clone" particles are simply translated with respect to those of the particles in the "mother" box.

 Another important aspect that affect the accuracy of the results obtained from the simulation is the choice of the timestep, which in turn determines how big the approximation in the integration of the equations of motion is [13]. It easy to understand that the higher the timestep is, the bigger the error in the integration will be. Let us consider, for example, a function $f(x)$
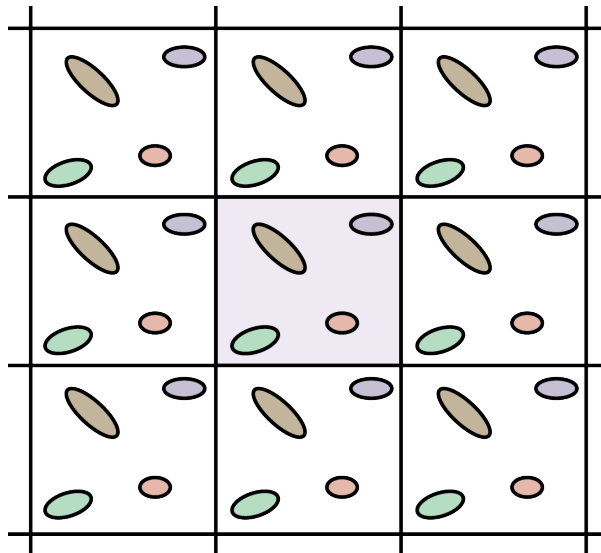
Figure 1.7: Periodic boundary conditions representation [17].

and imagine we want to calculate its integral from a to b, $\int_a^b f(x)$. Now imagine that it is not possible to solve that integral analytically: we have to employ some numerical method. To calculate the area below the curve (i.e. the integral), we divide the interval $a - b$ in n intervals of width:

$$\Delta x = \frac{b - a}{n} \tag{1.27}$$

We now build n rectangles which have, as base, the n segments in which the interval $a - b$ has been divided, and as height $f(a + i \cdot \Delta x)$, where $i = 0, 1, 2...(n - 1)$. The integral we would like to calculate can be approximated to the sum of the areas of the n rectangles:

$$\int_a^b f(x)dx \approx \sum_{i=0}^{n-1} f(a + i \cdot \Delta x)\Delta x \tag{1.28}$$

In Figure 1.8, a generic function $f(x)$ is numerically integrated from a to b using 8 rectangles. As it can be seen, the approximation is quite rough. The area below the curve is better approximated for high values of n. With $n \to \infty$, the sum of the area of the rectangles is exactly equal to the integral of $f(x)$ between a and b.

A comparison can be made between this example and the integration of the equation of motion in MD simulations. The lower the timestep Δt is, the higher the accuracy on the determination
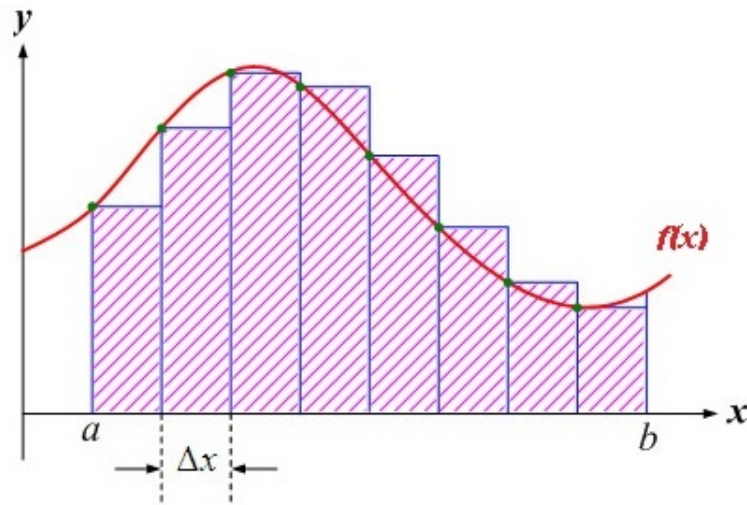
Figure 1.8: The area below the function $f(x)$ (red line) is approximated as a sum of rectangles.

of trajectory will be. Obviously, a lower Δt means also huger computation costs, so it is not possible to choose the timestep as little as desired. NAMD allows the user to control separately the frequency of computation of different variables, in order to save calculation time. The item *timestep* defines the frequency positions and velocities (i.e. trajectories) are computed with. Its magnitude is around a few femtoseconds, usually 1 or 2 fs. The simulation time will be equal to *number of timesteps × timestep* (it typically results in an order of magnitude of ns). A different frequency can be chosen for the computation of non-bonded interactions: since they are typically smaller than the bonded interactions (which are computed every *timestep*), they are generally calculated less frequently. The relative parameter is *nonbondedFreq*, whose value usually ranges from 2 to 4 fs. The frequency of computation of electrostatic energy, *fullElectrFrequency*, is chosen depending on the nature of the particles forming the system: if charged species are present, it is better to calculate the electrostatic interactions more frequently, while for neutral particles, a higher *fullElectrFrequency* can be chosen.

It is possible, with NAMD, to perform simulations keeping some thermodynamic variables constant, employing a particular so-called thermodynamic ensemble. If the simulation is carried on keeping the number of particles N, the pressure P and the temperature T constant, we say that the simulation is performed in a NPT ensemble. In such a kind of simulation, the volume of the box will vary in order to maintain the pressure at a target value, chosen by the user. On the order hand, if the simulation is carried on keeping N, T and the volume V

of the simulation box constant, then the system is running in a NVT ensemble, also called canonical. In such an ensemble, the volume of the box does not change during the simulation, while the pressure do, as a consequence. The crucial point is how to control parameters such as temperature and pressure, and maintaining them constant during the simulation. In my work, the method I employed for the control of temperature is the so called Velocity Rescale [18]: as the name says, in this algorithm, velocities of all particles are rescaled with a certain frequency by a factor λ in order to keep the temperature at the target value:

$$\lambda = \left(\frac{K_{target}}{K}\right)^{\frac{1}{2}} \text{ with } K_{target} = \frac{1}{2}Nk_BT_{target} \tag{1.29}$$

where N is the number of degrees of freedom in the system, K_{target} is the kinetic energy associated to target temperature, while K is the current kinetic energy. In NAMD, two parameters have to be specified, *rescaleTemp*, which is the target temperature, and *rescalefreq*, the rescaling period.

For what concerns pressure, the tool I have used mostly is the Berendsen barostat [19]. In this algorithm, the system acts as if it were in contact with a "bath of pressure" (it sounds funny, but the term helps to catch the concept, in analogy with the better know thermal bath met in the canonical ensemble). The variation of the bath pressure in time is given by:

$$\left(\frac{dp}{dt}\right)_{bath} = \left(\frac{p_0 - p}{\tau_p}\right) \tag{1.30}$$

where $1/\tau_p$ represents the coupling intensity of the system with the bath. Now remind that the pressure of the system is related to the kinetic energy and positions of the particles by:

$$p = \frac{2}{3V}(E_k - \Xi) \tag{1.31}$$

where Ξ is called virial, that is:

$$\Xi = -\frac{1}{2}\sum_{allcouples} \mathbf{r}_{lm}\mathbf{F}_{lm} \tag{1.32}$$

where r_{lm} is the distance between the centers of mass of particle l and particle m, while F_{lm} is the force acting between their centers of mass.

In order to keep pressure constant, a rescale of the distance between particles is needed, since they appear in the virial term (equation 1.32). As a consequence, coordinates will vary, and hence the volume too. Putting together the latter results with the velocity Verlet algorithm, it can be demonstrated that the rescaled position of a particle i will be:

$$\mathbf{r}_i(t) = \mu \cdot \tilde{\mathbf{r}}_i(t) \text{ with } \mu = \frac{1}{1 + \frac{\beta(p_0-p)}{3\tau_p}\Delta t} \tag{1.33}$$

where β represents the isothermal compressibility (i.e. the resistance of a material to compression, at constant temperature), supplied by the user (*BerendsenPressureCompressibility*). In addition, as for the velocity rescale thermostat, the frequency of position rescale (*BerendsenPressureFreq*) must be specified, which can be equal or greater than the timestep Δt.

Now we will focus on the form of the Force Field employed in NAMD. As said before, a FF must describe the intra- and intermolecular interactions that occurs among the particles of the system studied. First of all, let us consider bonded interactions, which involve atoms linked by chemical bonds. For two atoms bonded, the potential energy is related to the interatomic distance. The shape of the potential is well represented by a Morse's curve (Figure 1.9), which goes to ∞ when the distance r tends to 0, while is 0 when the two atoms are at infinite distance, and owns a minimum, which corresponds to the equilibrium distance.

$$V_{Morse}(r) = D_e[1 - e^{-\alpha(r-r_0)}]^2 \tag{1.34}$$

where r_0 is the equilibrium distance, D_e is the hole depth and α is a parameter that defines the hole width. However, in NAMD, the stretching potential is described by a simple parabolic curve (Figure 1.9), which is still good when the interatomic distance is not too far from equilibrium distance.

$$V_{stretch}(r) = k_{stretch}(r - r_0)^2 \tag{1.35}$$

where $k_{stretch}$ is the force constant for that particular bond: the higher it is, the steepest the curve will be, which means that atoms are forced to be close to the equilibrium distance,
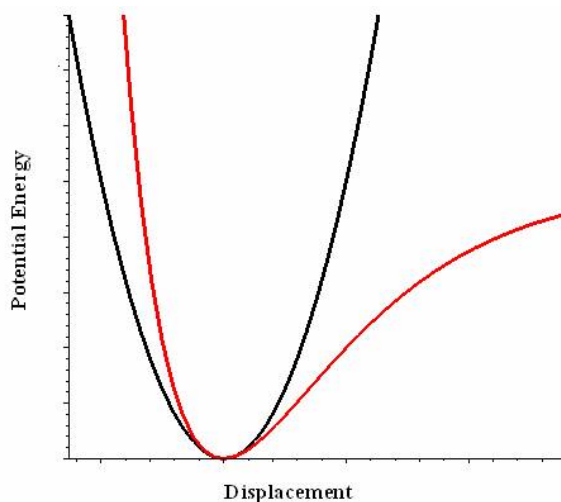
Figure 1.9: Morse curve for stretching potential (red line) and approximated parabolic stretching potential (black line).

without allowing big fluctuations.

An analogous potential can be defined also for a three-atoms interaction. Here the variable is not the bond length, but the amplitude of the angle formed by the three atoms. The expression of the bending potential, in NAMD, is:

$$V_{bend}(\theta) = k_{bend}(\theta - \theta_0)^2 \qquad (1.36)$$

where k_{bend} is the force constant for a particular triad of atoms, and θ_0 is its equilibrium angle. Another kind of interaction is the torsion of a dihedral angle, which involves four atoms. Contrary to the stretching and the bending potentials, the torsional potential has a periodic trend, with a period of 360° or lower, if the molecule has any kind of symmetry with respect to the bond over which torsion occurs. Maxima in the curve are related with conformations where the substituents are as close as possible, so that energy rises up due to steric hindrance, while minima correspond to conformations where the substituents are as far as possible, hence repulsion is low. In NAMD the torsional potential (Figure 1.10) is represented by the following expression:

$$V_{torsion}(\phi) = \sum_{i=1}^{6} k_{torsion,i}[1 + \cos(n_i\phi - g_i)] \qquad (1.37)$$
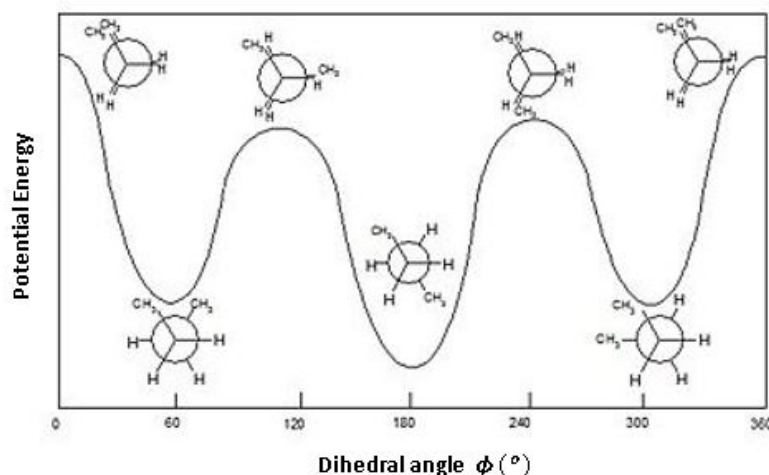
Figure 1.10: Torsional potential trend of butane [20].

where $k_{torsion,i}$ is the force constant for that particular dihedral angle, ϕ is the value of the dihedral, n_i is a multiplying factor that affects the period of the function ($T = 2\pi/n$), and g_i is the phase. As equation 1.37 shows, the torsional potential is a six-terms sum. Actually it is up to the user to choose how many terms to use, taking into account that six is the upper limit allowed by NAMD. Of course, the choice will depend on the complexity of the function to be represented.

Nonbonded interactions are responsible for the bigger part of computational costs of the simulations. This is the reason why, if it is possible, they are computed with a frequency that is lower than the timestep. They include electrostatic and dispersion contributes. Electrostatic potential between two atoms i and j is described by the well known Coulomb's law:

$$V_{electr}(r_{ij}) = \epsilon_{14} \frac{k_e q_i q_j}{r_{ij}} \tag{1.38}$$

where $k_e = 8.987 \cdot 10^9$ N m^2 C^{-2} is the Coulomb constant, q_i and q_j are the charges of the atoms i and j, respectively, and r_{ij} is the distance between the two particles. The term ϵ_{14} is a scaling factor whose value is 1, except when the interaction is between two atoms separated by three bonds. In this case, the atoms are involved in a torsion, and $0 \leq \epsilon_{14} \leq 1$.

Dispersion interactions, instead, occur even among neutral particles, and are represented by the Lennard-Jones (LJ) potential:
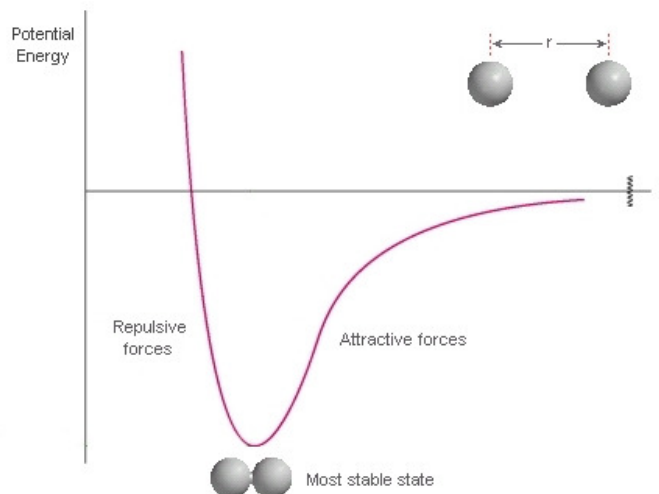
Figure 1.11: Lennard-Jones potential [22].

$$V_{LJ}(r_{ij}) = \epsilon_{ij} \left[\left(\frac{\sigma_{ij}}{r_{ij}} \right)^{12} - 2 \left(\frac{\sigma_{ij}}{r_{ij}} \right)^6 \right] \qquad (1.39)$$

A graphic representation of a LJ potential is shown in Figure 1.11. In equation 1.39 the term proportional to $1/r^{12}$ accounts the repulsion that occurs when atoms are at short distance each others, while the term proportional to $-1/r^6$ represents the weak attraction due to Van der Waals forces, which prevails at long distances. The terms ϵ_{ij} and r_{ij} describe the depth and position of the minimum in the curve, respectively. They are obtained through Lorentz-Berthelot combining rules, as follows:

$$\epsilon_{ij} = \sqrt{\epsilon_{ii}\epsilon_{jj}} \qquad (1.40)$$

$$\sigma_{ij} = \frac{\sigma_{ii} + \sigma_{jj}}{2} \qquad (1.41)$$

Since $V_{LJ}(r_{ij})$ rapidly tends to 0 as r_{ij} increases, it is approximated to 0 after a certain cutoff value of r_{ij}. Instead, the electrostatic potential, which goes as $1/r$, approaches to 0 much more slowly than the LJ potential, thus introducing a cutoff radius could seriously affect the accuracy of results [21].

 The FF of species involved in the simulation are included in a parameter file, which has to be read as an input by NAMD for the simulation to start. Other files NAMD requires as inputs are

the Protein Data Bank (pdb) file, where coordinates, atom type and residue type of all atoms are specified, and a Protein Structure File (psf), which tells the program among which atoms the various kinds of interactions have to be computed.

1.2   Liquid Crystal Mesophases

Everyday experience induces us to think that matter is present in nature just in three aggregation states, which are solid, liquid and gas, depending, we would say, on the strength of intermolecular attraction with respect to thermal energy ($k_B T$, where k_B is the Boltzmann's constant, 1.381×10^{-23} m^2 kg s^{-2} K^{-1}, and T is temperature): while the first aims at making particles get closer each others, the latter causes them to repulse. The balance between these kinds of interaction determines the aggregation state of matter. As thermal energy is proportional to temperature, warming a system brings thermal agitation to prevail on attraction forces, causing the distance among the particles to increase, resulting in a less condensed phase of matter. Even if very intuitive, it would be quite an understatement to consider the density as a criterion to classify the states of matter. A more accurate outlook is based on looking for some kinds of order, either positional and orientational. From this point of view, we can say that a crystalline solid is the most ordered material, as particles occupy well defined positions in a lattice and have particular orientations: they are constrained in a particular configuration, and no degree of freedom exists. On the other side, in liquids and gases, particles are allowed to change their position and orientation very easily, so neither positional nor orientational order is present. Thus liquid and gas are substantially the same phase, differing only for density, higher for liquids, lower for gases. Nevertheless, we are used to refer to both liquid and gas using the term "fluid". What is strange, adopting this perspective, is that also an amorphous solid can be seen as a liquid, as it does not own any kind of order, but with the particles frozen in a certain configuration. So, summarizing what said above, a phase of matter can be identified through its positional and orientational order: solid crystals own both, while fluids own none of them. Since there is not a physical law that forbid the existence of other aggregation states, we could say that, at least theoretically, phases different from crystals and fluids are possible, even if not present in nature. This idea pushed scientists to look for materials exhibiting new phases in addition to the conventional ones, and they found them. In Table 1.1, a (not complete) list of matter phases is shown, and the kind of order is specified.

It is very interesting to note that between crystals, which represents the most ordered phase, and fluids, which are instead the most disordered phase, there are other phases characterized by an intermediate degree of order. For example, in plastic crystals, particles are constrained in a well defined position, but at the same time they are allowed to rotate changing their orientation. This phase of matter is peculiar of some molecules endowed with a spherical shape.

Phase	Positional order	Orientational order
Crystal	yes (3D)	yes
Plastic Crystal	yes (3D)	no
Smectic A Liquid Crystal	yes (1D)	yes
Nematic Liquid Crystal	no	yes
Liquid	no	no
Gas	no	no

Table 1.1: Some of the most common phases of matter.

Liquid crystals have instead an orientational order. These phases are typical of molecules owning an elongated shape, which are able, in some conditions, to align each others. Moreover, if the molecules preserve a positional order in one direction, thus placing themselves on parallel planes, they are called smectic, otherwise, if no positional order exists, the phase they form is called nematic. As it has been stated just above, not every substance exhibits all the phases described, it depends on the chemical nature and the shape of the molecules, as well as on the conditions to which the system is subjected. As regards the latter point, just think about carbon bioxide (CO_2) [23], which, at atmospheric pressure, undergoes sublimation when a piece of solid CO_2, at low temperature, is warmed, becoming gas without passing through a liquid phase (Figure 1.12). In order to observe liquid phase it is necessary to work at a pressure higher than 5 atm.

We will now focus our attention on the liquid crystal phase, since I had to deal with the nematic 5CB as subject of my investigation during the internship I have made in professor Zannoni's group. As the name suggests, liquid crystals are an intermediate phase between solid crystals and isotropic liquids, exhibiting properties that are partly those of one and partly those of the other. Let us consider the behaviour that a crystal shows when crossed by a beam of polarized light: what happens is that it changes the plane of propagation of polarized light. This can be proved by placing a crystal sample between two polarizers, perpendicular to each others, and then irradiate the sample with a light source. When the unpolarized light beam passes through the first polarizer, only one plane of oscillation of the electric field is selected. If there were void between the two polarizers, this polarized light beam would arrive on the second polarizer as it came out from the first one, and so it could not cross the second polarizer, because the two filters are perpendicular to each others. The screen beyond the second polarizer would
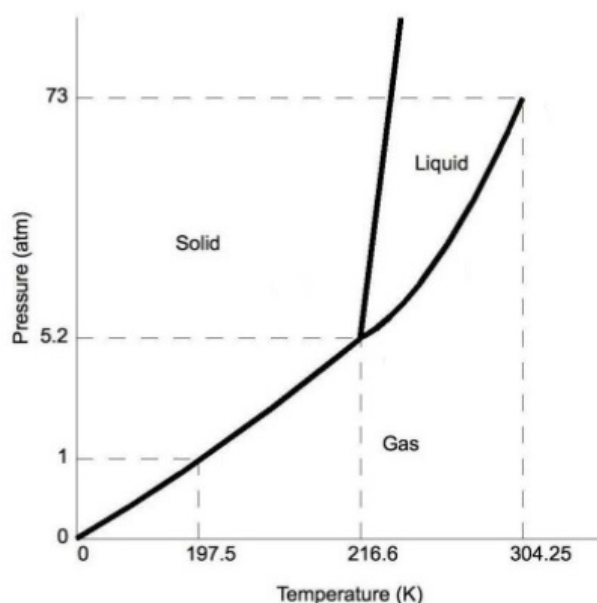
Figure 1.12: Phase diagram of CO_2 [24].

result dark (Figure 1.13). Instead, because of the presence of the crystal sample, the plane of polarization of the beam is rotated, and light can pass through the second polarizer, so that the screen is no more completely dark.

On the other hand, if an isotropic liquid is placed between the two polarizers, no light passes through the second polarizer, and the screen results dark. Indeed, in an isotropic medium, molecules are randomly arranged in the space, so each of them rotates the polarization plane of light in a way that is independent from the others. The overall effect is that no rotation results, and when the beam reaches the second polarizer, it is completely deleted. Liquid crystals, despite being liquid, are anisotropic medium, since molecules exhibit some kind of order, causing them to be able to rotate the plane of oscillation of polarized light, just as solid crystals do. The image projected on the screen by the light coming out from the second polarizer is peculiar for each class of liquid crystals. It would be very time demanding to make an accurate classification of all the classes, since plenty of them have been discovered in the last decades, so what follows is just a short summary of the most common classes of liquid crystals, including nematics, which were the ones I dealt with in my work.

First of all, it must be pointed out that LCs can be divided in two big categories, thermotropic and lyotropic. The first ones are so called because the transition from solid phase to liquid crystalline phase, and from this to isotropic liquid phase is determined by temperature. The
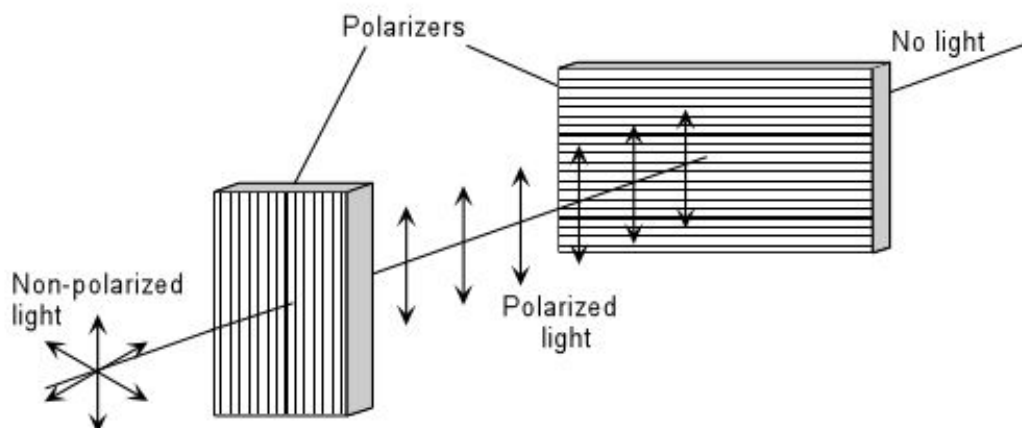
Figure 1.13: Cross-polarizers experiment [25].

second ones, instead, occur in a certain range of concentration of the molecules in a solvent.

1.2.1 Nematic Liquid Crystals

Nematic liquid crystals (NLCs) are the simplest class of thermotropic LCs. They own only orientational order, while not having a positional order at all. Nematogen molecules are similar to sticks, thus they can align with their axis (the *director*) parallel to each others, generating an anisotropic system. The consequence is that, as said above, they are able to rotate the oscillation plane of polarized light. The imagine obtained at the cross polarizers is shown in Figure 1.14 .

The particular imagine that results, very similar to fingerprints, is partly bright and partly dark:
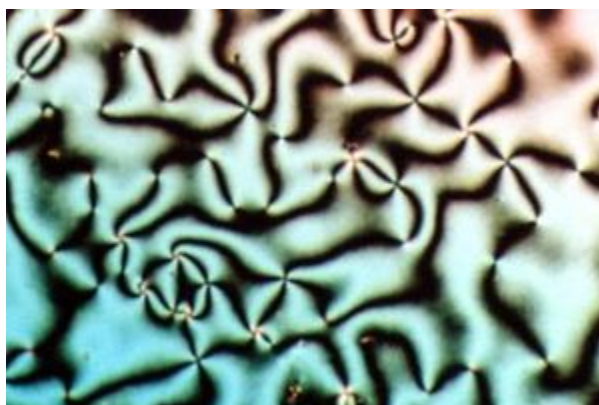

Figure 1.14: Typical texture of a nematic liquid crystal at polarizing microscope [26].

this phenomenon is due to the fact that molecules form domains of the order of hundreds of nanometers. These domains can rotate the plane of polarized light only if they are not aligned with any of the two polarizers, otherwise light is blocked. Since domains are differently aligned to each others, both situations can occur in different parts of the sample of LC, which results in the strange "fingerprints" image. In Figure 1.14, some black points are present: they are called "hot spots", i.e. zones where temperature is high enough to cause molecules to be in the isotropic liquid phase. The existence of domains is also the reason why LCs appear opaque. Their size is indeed that of visible light, so when light hits them, scattering occurs, just like in the case of milk (which is a colloidal suspension of fatty particles in water). It is sufficient to heat the system above the nematic to isotropic transition temperature to destroy the domains, obtaining a transparent isotropic liquid.

Technological applications of liquid crystals require the various domains to align each others. If the molecules own a dipole moment, it is possible to reach this alignment by applying a magnetic field **B**. The dipolar moment of the molecules is related to the field applied by the equation:

$$\mathbf{M} = \frac{\chi \mathbf{B}}{\mu_0} \tag{1.42}$$

where χ represents the magnetic susceptibility, and μ_0 is the magnetic permeability of free space ($\approx 12.57 \times 10^{-7}$ kg m s^{-2}). The energy molecules acquire when subjected to the field is give by:

$$U = -\mathbf{M} \cdot \mathbf{B} = \frac{-\mathbf{B}\chi\mathbf{B}}{\mu_0} \tag{1.43}$$

In order to obtain alignment, this energy must be greater than the thermal energy $k_B T$ (where k_B is the Boltzmann's constant and T is temperature), which is responsible for molecules agitation and thus hinders orientational order. The constraint that has to be satisfied is thus:

$$\frac{U}{k_B T} \geq 1 \Rightarrow \frac{\chi B^2}{k_B T} \geq 1 \Rightarrow B \geq \sqrt{\frac{\mu_0 k_B T}{\chi}} \tag{1.44}$$

If domains did not exist, the magnitude of the field B required to align molecules would be very high, greater than 1000 Tesla. However, since molecules are grouped in domains within which they have the same orientation, the strength of the field needed lowers of some orders of magnitude, as the described by the equation:

$$B \geq \sqrt{\frac{\mu_0 k_B T}{n\chi}} \tag{1.45}$$

where n is the number of molecules per domain.

A simpler way to obtain the domains alignment is to place the LC molecules on a surface that has been rubbed along a certain direction: the occurrence of microgrooves [27] on the surface induces the alignment within the rubbing direction, as can be seen from scanning electron microscopy (SEM). This technique has been largely employed in displays technology, as it will be shown further on.

Probably the most important family of NLCs is represented by cyanobiphenyls (nCBs) (Figure 1.15, top): these molecules consist, as the name suggests, by two bonded phenyl rings, subsituted, in the positions in para with respect to the C atoms involved in the bond, with a nitryl on one side and an alchyl chain (with variable length) on the other one. The elongated shape, and the high dipolar moment granted by the CN groups are fundamental features in order to obtain the nematic mesophase. Among the n-alchyl cyanobiphenyl series, 4-cyano-4'-pentylbiphenyl (5CB) (Figure 1.15, bottom) is the first that was discovered (in 1972 [28]) and certainly the most studied: this is the reason why I have employed it in one of my works. Its transition from crystal to nematic occurs at about 291 K [28], while its nematic to isotropic transition temperature (T_{NI}) is 308 K [29]. Being 5CB in a nematic phase at room temperature, a wide employment as a liquid crystal in technological applications is possible.

At the University of Bologna, the liquid crystals group, coordinated by professor Claudio
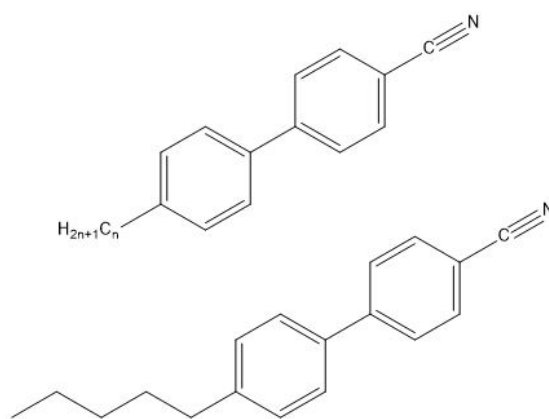

Figure 1.15: Chemical structure of a generic cyano-biphenyl molecule (left) and 5CB (right).

Zannoni, developed a Force Field which can predict the T_{NI} and other physical properties of nCB series with such a great accuracy [1]. Computing T_{NI} for n-CB molecules for n from 4 to 8, the values they obtained are in good agreement with experimental ones, with an error of

2-3 K at most [29]. The parameters of this Force Field are shown in Table 1.2. Atom labels
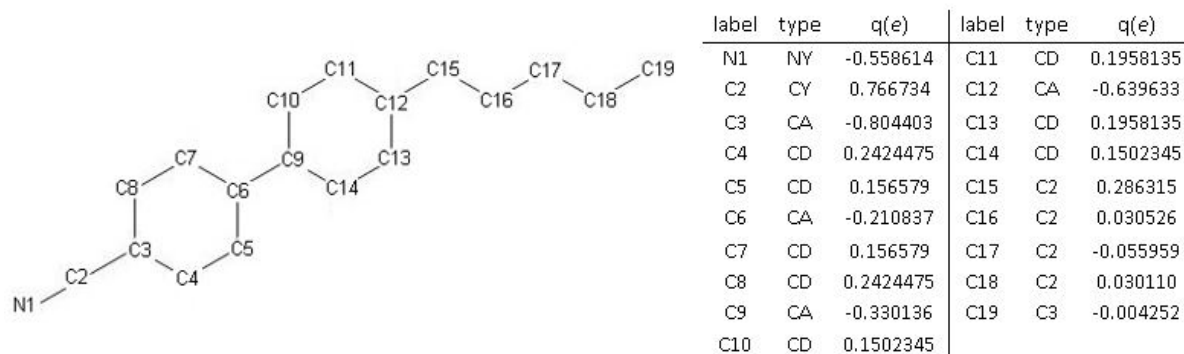with related atom types and electric charges are defined in Figure 1.16.

label	type	q(e)	label	type	q(e)
N1	NY	-0.558614	C11	CD	0.1958135
C2	CY	0.766734	C12	CA	-0.639633
C3	CA	-0.804403	C13	CD	0.1958135
C4	CD	0.2424475	C14	CD	0.1502345
C5	CD	0.156579	C15	C2	0.286315
C6	CA	-0.210837	C16	C2	0.030526
C7	CD	0.156579	C17	C2	-0.055959
C8	CD	0.2424475	C18	C2	0.030110
C9	CA	-0.330136	C19	C3	-0.004252
C10	CD	0.1502345			

Figure 1.16: Legend for 5CB atom labels.

interaction type	potential equation and parameters
bond stretching	$V_{stretching}(l) = k_l(r - r_o)^2$

bond	k_l (kcal mol^{-1} Å^{-2})	r_o(Å)
CA-CY	95.9	1.42
CD-CD	469.0	1.41
CA-CD	469.0	1.41
CA-CA	469.0	1.48
C2-C2	95.9	1.54
C2-C3	95.9	1.54
CY-NY	600.0	1.16
CA-C2	317.0	1.51

bond bending	$V_{bending}(\theta) = k_\theta(\theta - \theta_o)^2$

bond angle	k_θ (kcal mol^{-1} deg^{-2})	θ_o (°)
C2-C2-C2	63.0	112.4
C2-C2-C3	62.1	114.0
C3-C2-C3	62.1	114.0
CA-CA-CD	85.0	120.0
CD-CA-CD	85.0	120.0

CA-CD-CD	85.0	120.0
CY-CA-CD	85.0	120.0
CA-CY-NY	79.5	180.0
CD-CA-C2	70.0	120.0
CA-C2-C2	63.0	112.4

dihedral angles
$$V_{dihedral} = \sum_{i=1}^{3} k_{\phi,i}[1 + \cos(n_i\phi - g_i)]$$

dihedral angle	$k_{\phi,i}$(kcal/mol)	n_i	g_i (°)
X-CA-CD-X	2.65	2 ($i=1$)	180.0 ($i=1$)
X-CD-CD-X	5.3	2 ($i=1$)	180.0 ($i=1$)
X-C2-CA-X	0.5	6 ($i=1$)	0.0 ($i=1$)
NY-CY-CA-CD	0.0	1 ($i=1$)	180.0 ($i=1$)
X-C2-C2-X	0.6706	1 ($i=1$)	0.0 ($i=1$)
X-C2-C2-X	0.1365	2 ($i=2$)	0.0 ($i=2$)
X-C2-C2-X	0.14042	3 ($i=3$)	0.0 ($i=3$)
X-CA-CA-X	0.386681	0 ($i=1$)	0.0 ($i=1$)
X-CA-CA-X	0.061370	2 ($i=2$)	180.0 ($i=2$)
X-CA-CA-X	0.707914	4 ($i=3$)	0.0 ($i=3$)
X-CA-CA-X	0.215734	6 ($i=4$)	0.0 ($i=4$)

non bonded

Lennard-Jones
$$V_{LJ}(r_{ij}) = -\epsilon_{ij}\left[\left(\frac{\sigma_{ij}}{r_{ij}}\right)^{12} - 2\left(\frac{\sigma_{ij}}{r_{ij}}\right)^{6}\right]$$

atom type	σ(Å)	ϵ(kcal/mol)
C2	-0.0705	2.035
C3	-0.1050	2.050
CA	-0.0708	1.950
CD	-0.0708	1.950
CY	-0.0860	1.908
NY	-0.1700	1.824

non bonded

electrostatic $$V_{el}(r_{ij}) = \frac{q_i q_j}{4\pi\epsilon_o r_{ij}}$$

Charges are reported in Figure 1.16

Table 1.2: Force Field parameters for nCB series developed by the liquid crystals group at University of Bologna.

Nematics have been fundamental for the birth of the third generation of displays: after cathode ray tube (before) and plasma technology (after), now this is the time of Liquid Crystal Displays (LCD) [30]. As every digital display, they consist of a grid of pixels, each of them activated by an electric stimulus. Controlling separately each pixel allows to build an image, which can be formed and disrupted very quickly.

A common kind of LCD is the Twisted Nematic Liquid Crystal Display (TN-LCD). The typi-
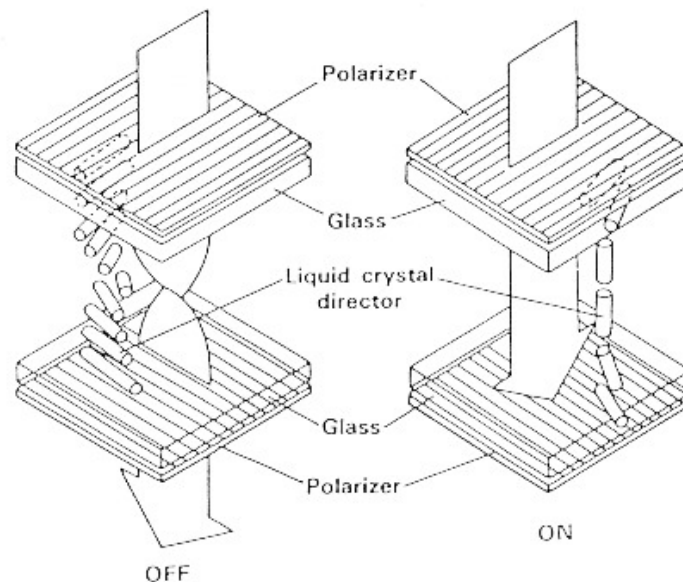

Figure 1.17: Behaviour of a TN-LCD pixel when the field is off (left) and on (right) [31].

cal structure of a TN-LCD pixel is presented in Figure 1.17. A thin film of few micrometers of a nematic phase is placed between two glass surfaces, with a polaroid leaning on the external side of both of them. The two polaroids are perpendicular one another. On the internal side, the two glass surface have been rubbed in order to obtain microgrooves, which are responsible for the alignment of nematic molecules nearby the surface. The rubbing direction is the same as the polaroids. In this way, molecules on one side are aligned in a certain direction, which is perpendicular to that of molecules on the other side. For this reason, molecules in the middle of the nematic film, will arrange generating a helix: in each plane (parallel to the two glass

surfaces), molecules will be parallel to each other, but oriented differently from molecules on other planes. This system is able to rotate polarized light plane, so light can be transmitted through the pixel despite of the presence of cross polarizers. When an electric field is applied, molecules align within the field direction: light cannot pass any more, and the pixels results black. Varying the field magnitude, it is possible to control in what extent the helix is disrupted, and so the amount of light transmitted: a greyscale is thus obtained. If colours are desired, a polychromatic light source must be employed, and coloured filter are required to allow only some wavelength to pass.

Another class of LCDs is represented by In Plane Switching Liquid Crystal Displays (IPS-LCD) (Figure 1.18). The functioning of this device is very similar to that of TN-LCD, but in this case the two glass surfaces are rubbed along the same direction. When the electric field is off, molecules are all parallel inside and among every plane. This means that light cannot be transmitted through the pixel. In order to form the helix and hence make light pass, an electric field is applied only on one face of the pixel. With respect to TN-LCD, light passes when the field is on, while dark results when the field is off.

LCDs are not exclusively based on the formation and disruption of the helix. For example, in
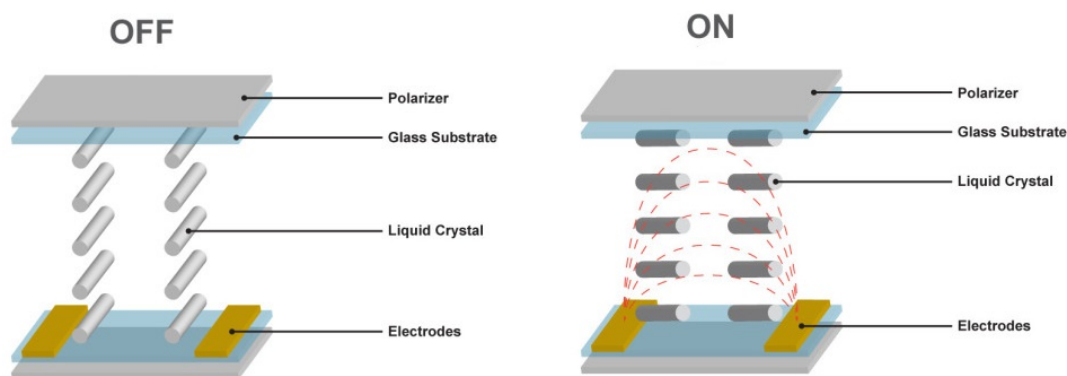

Figure 1.18: Behaviour of a IPS-LCD pixel when the field is off (left) and on (right) [32].

Vertical Aligned (VA) displays, if molecules are parallel or perpendicular to the incident light, then the pixel will be dark, otherwise, for any other tilt, light passes. In order to vary the tilt angle, an electric field is applied, as shown in Figure 1.19. Molecules must have a dipole moment perpendicular to the their axes. When the field is off, molecules must orient perpendicular to the surface. To achieve the vertical alignment surfaces can be treated with some reactants to induce the formation of protuberances that act as a comb for the LC molecules to orient. For

this kind of displays it would be great to find materials that induces vertical alignment of LC molecules by their own, without needing a chemical treatment.
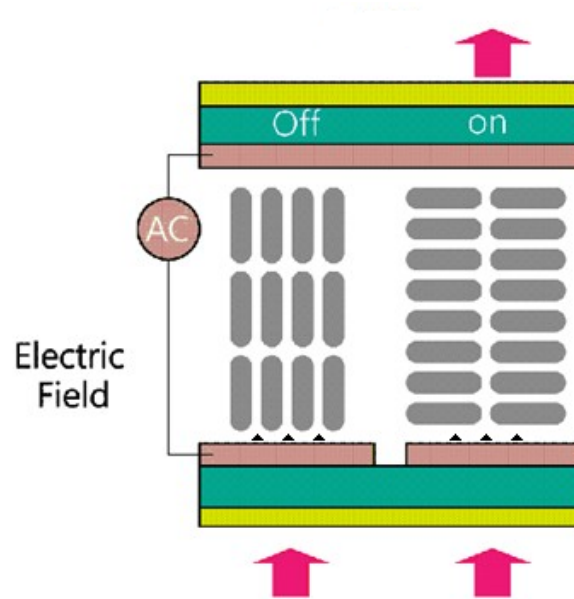

Figure 1.19: Behaviour of a VA-LCD pixel when the field is off (left) and on (right) [33].

1.2.2   Smectic A Liquid Crystals

As nematics, this family of thermotropic LCs has an orientational order, and moreover it owns a positional order in one direction: it means that molecules are arranged in planes parallel to each others, while being aligned within the same axis, perpendicular to the direction of extension of planes. In another kind of smectics, the type C, molecules are tilted with respect to the normal to the planes. The planes can be completely separate, or they can interdigit, depending on the chemical nature of molecules. The image obtained with a polarizing microscope from a smectic A liquid crystal (shown in Figure 1.20) is called "fan": dark zones are due to defects, which are caused by the fact that the planes tend to suit the surface, without losing parallelism. Molecules that show a smectic A phase are cyanobiphenyls, as for nematics, but usually with a longer alchyl chain.

In smectics, as well in nematics, orientational order is a crucial point that determines the properties of these phases. Thus, it becomes fundamental to establish a method to quantify the degree of alignment of molecules. This was done by introducing a parameter that varies
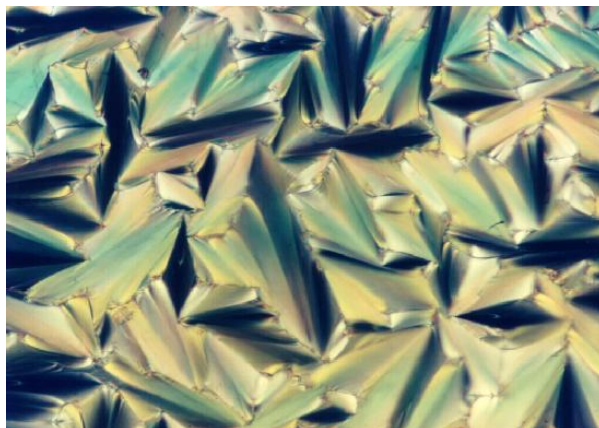
Figure 1.20: Typical texture of a nematic liquid crystal at polarizing microscope [34].

from 0 to 1. It is 0 when the system is completely disordered, 1 when molecules are perfectly aligned, and assumes intermediate values in case of partial order. The equation of the order parameter is:

$$\langle P_2 \rangle = \frac{3}{2} \langle \cos^2 \theta \rangle - \frac{1}{2} \tag{1.46}$$

where θ is the angle between the principal axes of a molecule and a reference direction called director. The use of angle brackets means that a mean is computed over all the molecules composing the system. It is easy to verify that, when molecules are parallel to the director, $\theta = 0°$ for each of them, then the mean $\langle \cos^2 \theta \rangle$ is 1, and the order parameters results 1. On the other hand, when the system is perfectly disorder (i.e. isotropic) every value of θ is equally probable, and $\langle \cos^2 \theta \rangle$ is $1/3$, so that the order parameter becomes 0. The notation of $\langle P_2 \rangle$ with angle brackets is due to the fact that the equation of order parameter is that of the mean of the second Legendre polynomial $P_2 = (3cos^2\theta - 1)/2$.

1.2.3 Discotic Liquid Crystals

Not only stick-shaped molecules are suitable to generate liquid crystalline phases. An important class of thermotropic LCs is represented by discotic liquid crystals, which are obtained from flat molecules, extended in a plane. The most common molecule employed is triphenylene [35], substituted in some extent with alchyl chains (not to affect electronic properties) or polar groups. Disk-shape molecules stack one on the other spontaneously, generating columnar structures (Figure 1.21). It is possible to enhance the easiness the columns form with by employing two different kinds of triphenylenes, one subsituted with electron-withdrawing groups and the other with electron-donor groups: in this way, electronic effects will make the assem-

bling faster, by alternating the two types of molecules. Conductivity of columns is obviously anisotropic, being considerably higher along the axis of the columns. For this reason, discotics have been thought to be employed as "molecular electric wires".
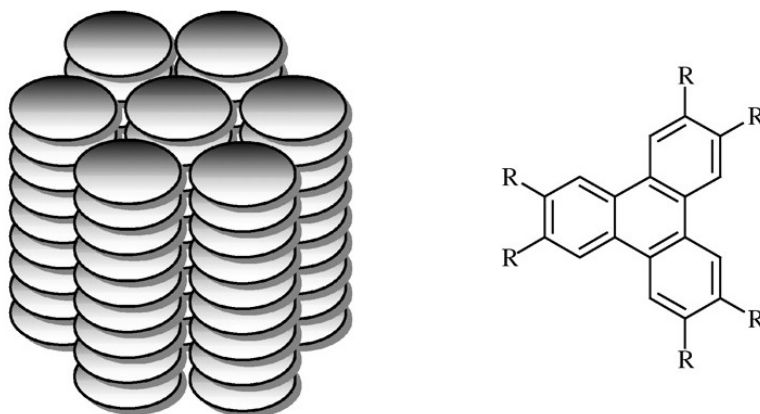

Figure 1.21: Graphic representation of a columnar (hexagonal) mesophase (left) and chemical structure of triphenylene (right) [36].

1.2.4   Cholesteric Liquid Crystals (Chiral Nematics)

It was observed that, in solution, cholesterol molecules, dispose generating a helix, with a pitch p comparable to wavelength of visible light (Figure 1.22). If one imagines to dissect a cholesterol solution sample at different heights, what is expected to be seen is that in each plane, the molecules are parallel to each other, but rotated of a certain angle with respect to molecules in different planes. Lately, other molecules were observed to exhibit this behaviour, showing orientational order only inside a plane, and varying the orientation angle moving from one plane to another. This class of liquid crystals is called cholesteric or chiral nematic.

Cholesterics find an important role in photonics, since having a periodic structure in one direction, with period equal to the pitch, they work as Bragg's grid: depending on the pitch p of the helix, a cholesteric permits only certain wavelengths to be reflected, while deleting the others, as stated by the famous Bragg's law (Figure 1.23). The wavelength selected is the one for which constructive interference occurs, according to Bragg's equation:

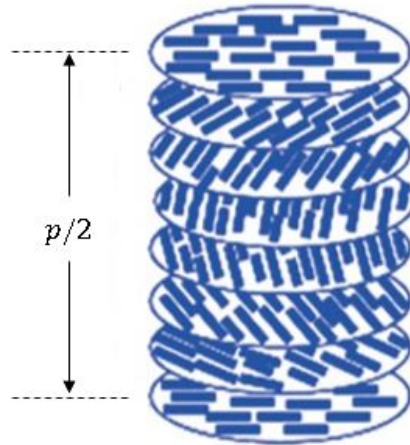$$2d\sin\theta = n\lambda \qquad\qquad (1.47)$$

Figure 1.22: Cholesteric liquid crystalline mesophase [37].

where d is half pitch, θ is the angle that the incident beam of light forms with the planes of the cholesteric, λ is the wavelength of light and $n = 1, 2, 3, 4....$ Since $2d \sin \theta$ is a constant, provided that θ has been fixed, then also $n\lambda$ must be constant. This means that only the sub-multiples of a certain wavelength (the one corresponding to $n = 1$) will be reflected. However, the greater n is, the lowest the intensity of the wavelength reflected will be. In practice, Bragg's law states that, if white light crashes into the cholesteric, only some wavelengths (principally just one) are reflected, thus the light that outcomes is coloured.

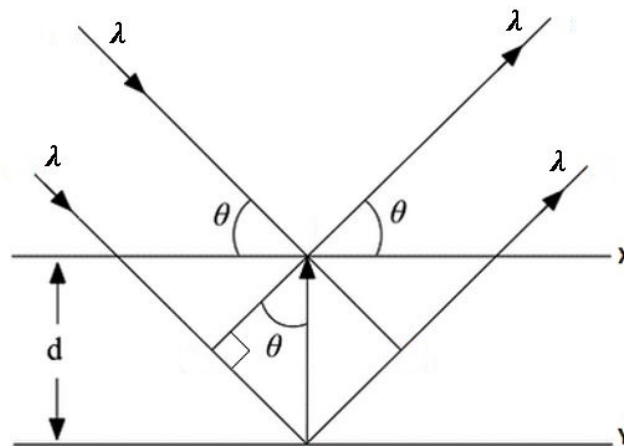What is more interesting is that the pitch of the helix can vary depending on temperature,

Figure 1.23: Bragg's law acting on two parallel planes X and Y.

through the relation:

$$p(T) = p_0[1 + \alpha(T - T_0)] \tag{1.48}$$

where p_0 is the pitch at a certain temperature T_0, and α is a multiplying factor. By heating or cooling the cholesteric, the pitch changes, and consequently the reflected wavelength changes too. This phenomenon has been employed for technological applications, such as optical thermometers: a thin film of cholesteric is placed on a support slab of plastic or paper. Each part of the slab assumes a colour that depends on the temperature in that point. Through a colorimetric scale it is possible to get the values of temperature.

An even more interesting application of cholesteric LCs is represented by cholesterics lasers [38]. Here, the classical cavity where photons bounce back and forth is replaced with a cholesteric medium, in which phluorescent molecules are drown. As seen above, there is a little range of wavelengths, $\Delta\lambda$, that is reflected. Other wavelengths are transmitted. If the phluorescent molecule is chosen suitably, so that its phluorescence spectrum is inside the reflection band gap of the cholesteric, with just a little part out of it, then only this thin band will be transmitted outside the cholesteric, while the rest of phluorescence light will remain trapped.

1.2.5   Lyotropic Liquid Crystals

This class of liquid crystals are based on the fact that, when a suspension of some molecules in liquid reach a certain concentration, they can organize in a ordered phase. It was observed, for example, that carbon nanotubes in water form an isotropic phase if their concentration is low, but increasing this one, molecules start to align within the same direction, obtaining a liquid crystalline phase, which is able to rotate the plane of polarized light. Usually, a lyothropic mesophase is obtained employing an amphiphilic molecule, i.e. a molecule possessing in its structure both a hydrophilic and a hydrophobic (lipophilic) part. The hydrophilic part is usually an electrically charged group, while the hydrophobic part could be a long alchyl chain. Fatty acids employed in soaps and phospholipides of cell membranes are just two examples of amphiphilic molecules. When these molecules are in contact with a polar solvent like water, they organize in order to minimize the exposure of their lipophilic part to water. The structure they assume depends on the concentration and the nature of the molecules. When the concentration overcomes a crucial concentration called critical micelle concentration (CMC), the molecules, previously disordered, form spherical structures (micelles), exposing their polar head to the external water, while leaving the hydrophobic tail inside, far from water. If the concentration of amphiphile increases, micelles will not be the most stable structure any more,

because they would be too big, with a huge cavity at the center of the sphere. Thus, molecules adopt new structures, for example cylindrical or cubic. If concentration is even higher, double layer formation occurs.

1.3 Polydimethylsiloxane

PDMS is a polymer belonging to the family of siloxanes, which are characterized by the silicon-oxygen (-Si-O-) bond. Its repeating unit is shown in Figure 1.24, together with the general structure of a polysiloxane.

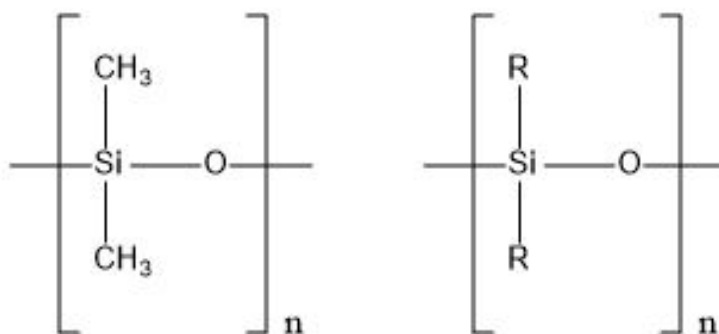The synthesis of PDMS is carried out starting from the monomer dimethyldichlorosilane

Figure 1.24: PDMS chemical formula (left) and generic polysiloxane chemical formula (right).

(DMS-Cl) through a step-growth polymerization: DMS-Cl is hydrolized by adding water, forming dimethylsiloxane, which is the real reacting species of the reaction. From the process, hydrochloric acid evolves [39]. Because of dangerousness, an alternative process, in which chloride is replaced with an acetate group, has been developed. As an inconvenient, the reaction is much slower. The reaction that occurs is shown in Figure 1.25 below:

A common feature of these compounds is the incredible flexibility of the backbone, which is

$$n\ Si(CH_3)_2Cl_2 + (n+1)\ H_2O \longrightarrow HO\left[Si(CH_3)_2O\right]_n H + 2n\ HCl$$

Figure 1.25: PDMS synthesis reaction.

allowed by the fact that oxygen is bivalent, hence it makes only two chemical bonds with the silicon atoms that precede and follow it, respectively. There are no substituents on it, as occurs instead in carbon chain polymers. As a consequence, polysiloxane chains are much more free to rotate over Si-O bonds, even at very low temperatures. Nevertheless, polysiloxanes are one of the families of polymers with the lowest glass transition temperatures (T_g). The glass transition temperature is in fact the temperature above which the polymeric material behaves as a gum, since main chain movements are allowed, while below it the material has a glass behaviour (torsional movements are blocked). The T_g of PDMS is about $-125°$C [40], which is incredibly low with respect to conventional polymers such as polyethylene (PE) ($T_g \approx -40°$C) [41], polypropylene (PP) ($T_g \approx -10°$C) [42], polyvinyl chloride (PVC) ($T_g \approx 90°$C) [43] and polyethyleneterephthalate (PET) ($T_g \approx 85°$C) [44]. This means that PDMS keeps elastic properties in conditions when other polymers would be hard and fragile. Thanks to this feature, PDMS has been employed for a long time in technological applications where fluidity and elasticity is required, such as glues, sealants, lubricants and adhesives (low molecular weight is necessary). In these cases, PDMS acts like a viscous liquid material, with very low Young's modulus. On the other hand, this polymer finds a huge application as an elastomer, provided it has been previously cross-linked. Elastomers are a class of polymeric materials endowed with a great capability to deform when subjected to a tensile stress, recovering their original dimension once the stress has been removed. This unique feature is due to the presence of chemical or physical bonds among chains, preventing the material to get permanently deformed when a tensile force is applied. In the case of PDMS, reticulation is obtained adding to the linear PDMS a certain amount of vynil-terminated oligomers (depending on the desired degree of cross-linking) [40]. The reaction is carried out at relatively low temperatures, and catalyzed by platinum (Figure 1.26).

 Due to its high flexibility, together with good thermal resistance, chemical inertness, antibiotic nature and atoxicity, PDMS elastomer has great potentialities in many fields of applications, such as cookware, toys, prothesis and medicine in general, electronics, coatings and optics, as a material for building wave-guides [45], just to cite some examples, without forgetting its leading role in soft lithography [46]. Cross-linking causes T_g to increase (according to the degree of reticulation), and PDMS to get more rigid.

Due to its wide employment in such a plenty of fields, PDMS has increasingly caught the attention of scientific research, whose purpose is to better understand why this polymer is so
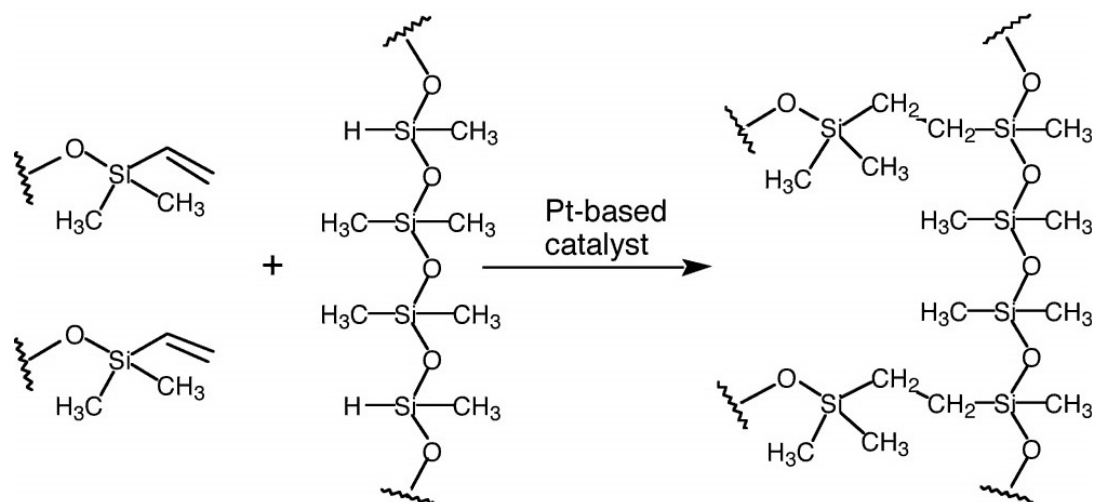
Figure 1.26: The cross-linking reaction of PDMS [40].

unique. A big effort was made by computational chemists, who found in MD simulations a powerful tool for the investigation of PDMS properties. In the last years, many groups tried to develop a Force Field for this polymer. The first attempt was made by Sok et al. [47]: they developed a FF to compute solubility and diffusion coefficient of methane (CH_4) and Helium (He) in PDMS melt, obtaining results that agree with experiments with respect to diffusion coefficient but not to solubility. A better agreement with experimental data on PDMS melt was reached by Frischknecht et al. [48]. Afterwards, Sun [49] developed an explicit atom (i.e. hydrogen atoms are represented separately) Force Field based on QM calculations carried out on oligomers, and Smith et al. [50] improved this FF through more accurate counts. One of the latter works was that of the group of Makrodimitri [51], which developed a United Atom (UA) Force Field. Here, hydrogen atoms are not represented explicitly, but rather merged with the carbon atoms they are bonded to. In this way, a huge amount of computational cost is saved, since the system simplifies: every repeating unit is composed of 4 atoms, and not 10, as in a explicit atoms model. As a consequence, the number of degrees of freedom is reduced. In Makrodimitri's FF, bonded, electrostatic and LJ parameters for silicon and oxygen are those calculated by Sok [47], while parameters related to CH_3 were adjusted in order to make simulated density match with experimental one, measured at ambient conditions. The Force Field developed was then employed for the computation of solubility of some substances (n-alkanes, n-perfluoroalkanes, noble gases, N_2 and O_2) in PDMS melt. Values of the parameters and po-

tential functions of Makrodimitri's Force Field are shown in Table 1.3.

The group ran simulations on samples composed of three 80 units chains, using periodic boundary conditions. The timestep was chosen to be 0.5 fs, equilibration phases last 1 ns, while production phases were 5 ns long. Simulations were carried out at three different temperatures, 300 K, 375 K and 450 K, and for each of them, at pressure 0.1 MPa, 10 MPa and 40 MPa. Best results with respect to experiments were obtained for simulations at 0.1 MPa, while bigger errors arose from higher pressures. Radial distribution function was computed, showing a very good agreement with experimental data obtained through X-ray scattering, for both peaks intensity and position.

A very interesting phenomenon regarding PDMS which is still unclear, is the fact that this polymer induces some liquid crystals molecules, such as the ones belonging to the cyanobiphenyls family, to align perpendicularly to a surface made of this polymer. Many experimental works in which LCs perpendicular (homeotropic) alignment on PDMS is observed have been published. For example, Xia et al. [8] studied the alignment of LC molecules inside PDMS micropores, in order to realize nematic liquid crystal elastomers (NLCE). They carried out experiments on (4"-acryloyloxybutyl)-2,5-di(4'-butyloxybenzoyloxy)benzoate (LCM4) and 5CB simultaneously (the first because it is a monomer for LC polymer, the second because it is the best known LC molecule). In both cases, a planar anchoring with respect to the PDMS pore walls was observed, finding a possible reason in the low surface tension of PDMS (~ 20 mJ/m^2).

In another experimental work, Suh et al. [52] studied the control of nematic LCs alignment on a glass surface through a technique called thermo-transfer printing. It consisted in putting in contact the glass surface with a PDMS slab, at high temperature, for a certain period, after which the PDMS slab is lifted, leaving a PDMS layer deposited on the glass surface. Placing E7 (a mixture of cyanobiphenils with long aliphatic chains employed in LCDs) on the glass surface, they found that the amount of PDMS transferred on the glass (which in turn depended on the temperature and the processing time) affected the orientation of LC molecules. For untreated glass, planar anchoring was observed, while a homeotropic anchoring was obtained for a 100% covered glass surface. Intermediate tilt angles occurred for lower degrees of coverage. Surface tension was found to decrease from 65.2 mJ/m^2 (0 % PDMS) to 21.9 mJ/m^2 (100% PDMS).

Again, Ahn et al. [6] published an article where they describe the possibility to control LCs alignment placing them on a hybrid surface made of PDMS and poly(vinyl cinnamate) (PVCi).

interaction type	potential equation and parameters
bond stretching	$V_{stretching}(r) = \frac{1}{2}k_l(r - r_o)^2$

	bond	k_l (kcal mol^{-1} Å^{-2})	r_o (Å)
	Si-O	700.2	1.64
	Si-CH$_3$	379.3	1.90
	O-CH$_3$ (terminal)	700.2	1.64

interaction type	potential equation and parameters
bond bending	$V_{bending}(\theta) = \frac{1}{2}k_\theta(\theta - \theta_o)^2$

	bond angle	k_θ (kcal mol^{-1} deg^{-2})	θ_o (°)
	O-Si-O	0.0575	109.5
	O-Si-CH$_3$	0.0304	109.5
	CH$_3$-Si-CH$_3$	0.0304	109.5
	Si-O-Si	0.0153	144.0
	Si-O-CH$_3$ (terminal)	0.0153	144.0

interaction type	potential equation and parameters
dihedral angles	$V_{dihedral} = \frac{1}{2}k_\phi(1 - \cos 3\phi)$

	dihedral angle	k_ϕ (kcal/mol)
	Si-O	1.8

interaction type	potential equation and parameters
non bonded Lennard-Jones	$V_{LJ}(r_{ij}) = 4\epsilon_{ij}\left[\left(\frac{\sigma_{ij}}{r_{ij}}\right)^{12} - \left(\frac{\sigma_{ij}}{r_{ij}}\right)^6\right]$

	atom type	σ(Å)	ϵ(kcal/mol)
	Si	3.385	0.585
	O	2.955	0.203
	CH$_3$	4.170	0.160

interaction type	potential equation and parameters
non bonded electrostatic	$V_{el}(r_{ij}) = \frac{q_i q_j}{4\pi\epsilon_o}\left(\frac{1}{r_{ij}} + \frac{(\epsilon - 1)r_{ij}^2}{(2\epsilon_s + 1)r_c^3}\right)$

	Si	O	CH$_3$
q (e)	0.3	-0.3	0.0

Table 1.3: Makrodimitri's parameters for PDMS potential.

The first polymer induces homeotropic anchoring, while the second one causes planar anchoring. Varying the ratio between PDMS and PVCi, it is possible to obtain all tilt angles from $0°$ to $90°$.

As told above, the homeotropic anchoring of LC molecules on a PDMS has not been clearly explained yet, despite several hypothesis have been presented. The purpose of my work at the liquid crystals group was to employ MD simulations to understand better the origin of this phenomenon. Since the calculation of a Force Field for PDMS would have been too time demanding, we decided to employ the one obtained by Makrodimitri [51]. Since that FF was developed for linear PDMS, it does not contain parameters concerning the new bonds formed during reticulation process, hence they had to be obtained from other sources. Some of them were taken from the universal MM2 Force Field [53], some others from a previous work of Roscioni et al. [4] regarding the study of 5CB alignment on alkylsilane self-assembled monolayers. Parameters inherent to Si-CH_2-CH_2-Si dihedral were instead computed through quantum mechanic calculations, as it will be described in Chapter 5.

Chapter 2

Samples preparation and analysis

2.1 Samples features

The first step consisted in preparing three different PDMS samples, differing from each other for chain length and number of chains (but with a similar total number of atoms), as described below:

- PDMS7: 250 chains, each made of 7 repeating units (28 atoms), total number of atoms 7000;

- PDMS13: 135 chains, each made of 13 repeating units (52 atoms), total number of atoms 7020;

- PDMS20: 90 chains, each made of 20 repeating units (80 atoms), total number of atoms 7200.

Samples were prepared with the software Packmol [54], after having generated a single chain (through a script that allowed a fast and automated procedure). Then the psf file was obtained using Psfgen [55], provided it was given the topology file (i.e. a file containing information about the bonds among atoms forming a molecule) as input. Before starting an equilibration phase, it is usually convenient to do few steps of minimization: in this phase, the geometry of molecules is adjusted according to the FF in order to set energy at minimum. Then the real simulation can take place: in the equilibration phase, the system is let evolve and trajectories of molecules are computed.

Our simulations were performed with NAMD employing a NPT ensemble, inside a box which

was initially 90 Å× 90 Å× 90 Å. Equilibration was preceeded by a 150000 steps minimization phase. Temperature was controlled through Velocity Rescale [18] while a Berendsen barostat [19] was employed to keep pressure constant. The chosen timestep was 2 fs, while frequencies of 4 fs and 8 fs were used to compute non-bonded and electrostatic interactions, respectively. Our aim was to simulate these samples at room conditions, i.e at 300 K and 1 bar. Since we dealt with a polymer (even if composed by short chains), we thought it was better to move towards ambient conditions little by little starting from high temperature and pressure, in order to reach equilibrium conformations of chains faster (and avoiding the risk of getting stuck in a metastable state). To achieve that, we started simulations from samples at 400 K and 400 bar and then, after leaving the systems run for some time (about from 20 to 50 ns), pressure had been slowly decreased to 100 bar. After some time of production in these conditions, pressure was lowered again to 1 bar, then a cooling phase from to 400 K to 350 K was performed. Finally, after a production run of about 50 ns at 350 K and 1 bar, they were brought to 300 K (Figure 2.1). Temperature and pressure decreasing protocol consisted in diminishing them of 5 units in 30 ps. It is worth to underline that slow temperature and pressure decreasing protocols and quite long production phases between every operative conditions change allowed to make systems reach thermodynamic equilibrium, which in turn means better simulations. Nevertheless, this process took us a large amount of time.
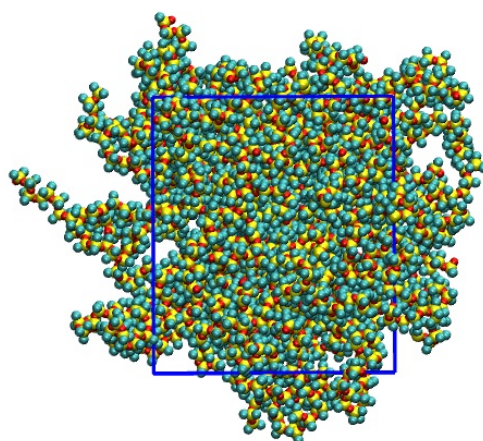

Figure 2.1: PDMS20 sample equilibrated at 300 K and 1 bar. Silicons are shown in yellow, oxygens in red, carbons in light blue. Simulation box is shown in blue.

2.2 Radial distribution function

The various PDMS samples were analyzed computing several properties that gave us information about the structure. First of all, $g(r)$ trends were obtained. Regarding this property, it is possible to decide whether taking into account all atoms or not. A quite common usage is to compute radial distribution function of a certain atom type with respect to another atom type, being them the same or different ones. In our case, it has consisted in computing $g(r)$ for the couples Si-Si, O-O, CH_3-CH_3, Si-O, Si-CH_3 and O-CH_3. The $g(r)$ among centers of mass have been computed as well. In addition, since the molecule we dealt with was a polymer, we had to distinguish intermolecular and intramolecular contributes. As a consequence, three different kinds of $g(r)$ have been calculated: a total $g(r)$, which took into account for both intermolecular and intramolecular contributions, an intermolecular $g(r)$, and an intramolecular $g(r)$. The total $g(r)$ was obtained with *Outside*, a software developed from some members of the liquid crystal group of University of Bologna. Intermolecular and intramolecular radial distribution functions were instead computed by a script taking advantage of "measure gofr", a radial distribuction function tool of VMD [55], a software for graphic visualization and analysis of molecules and particles trajectories obtained through MD simulations. Figure 2.2 shows a comparison of $g(r)$ for PDMS7, PDMS13 and PDMS20 samples (at 300 K and 1 bar) and Makrodimitri's [51] trend (at 300 K and 0.1 MPa).

As it can be seen in Figure 2.2, no difference arises from the three samples we analyzed (their curves are perfectly superimposed). In addition, comparing our results to Makrodimitri's [51], we can state that positions of peaks is approximately the same, but in Makrodimitri's trend they are higher and more detailed. For example, in the region between 1 Å and 2 Å our samples show only one peak, while Makrodimitri observed two peaks. Reminding that operative conditions were nearly the same (temperature 300 K and pressure 0.1 MPa $\approx$ 1 bar), chain length and sample size could have affected the results. Makrodimitri's chains are in fact 80 units long, and the sample is composed of only three chains. Chain length effect could be negligible when the length difference is little, as it is the case of our samples. However, the trend we obtained is that typical of a liquid, with only one high peak and a low second one. On the contrary, Makrodimitri's total $g(r)$ could resemble to that of a solid.

In Table 2.3 intramolecular $g(r)$ of PDMS7, PDMS13 and PDMS20 samples, at 300 K and 1 bar, for all possible couples of atoms, are reported. Makrodimitri's trend at 300 K and 0.1 MPa are also shown for a comparison.
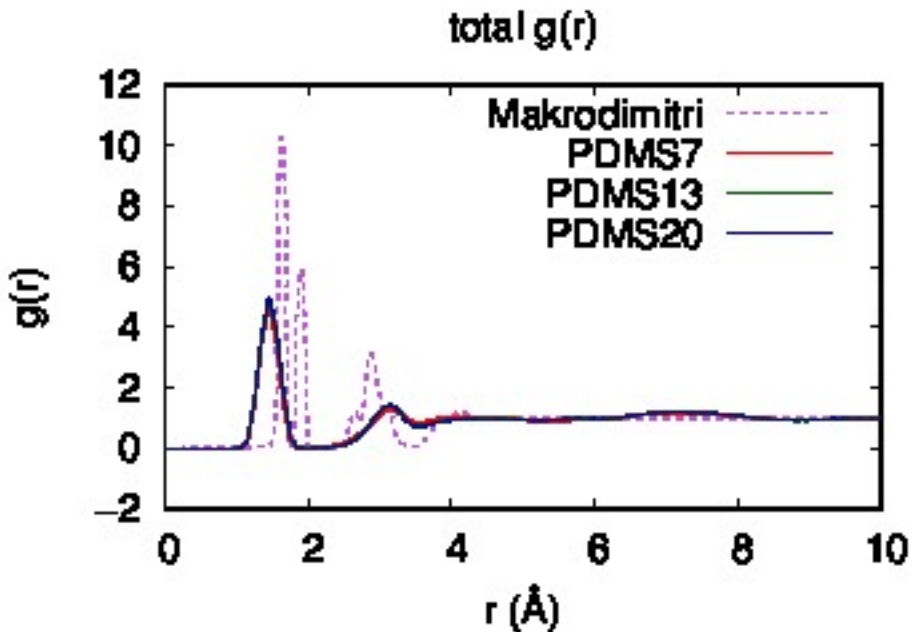
Figure 2.2: Total $g(r)$ of PDMS7, PDMS13, and PDMS20 samples and Makrodimitri's.

It is worth to point out that Makrodimitri's trends have been obtained from the original article by digitalizing plots using the software WebPlotDigitizer [56]. A problem we met is that in the article, highest peaks are cut, so we did not know their real height. Moreover, Makrodimitri's intramolecular $g(r)$ functions are not normalized (the function does not tend to 1 for $r \to \infty$), so we had to adapt our curves to those of Makrodimitri, in order to make a comparison. As it can be observed, peaks height increases within shortening of chains, highlighting that, the more little molecules are, the more ordered the system is. This is clearly visible in the plot related to CH_3-CH_3 in Figure 2.3, where PDMS7 curve is the highest, while PDMS20 curve is the lowest among our samples. Makrodimitri's trend is even lower, since this sample is composed of 80 units long chains. In Figure 2.4 intermolecular $g(r)$ of PDMS7, PDMS13 and PDMS20 samples, at 300 K and 1 bar, for all possible couples of atoms, are reported, as well as Makrodimitri's curve (at 300 K and 0.1 MPa).

Intermolecular $g(r)$ curves computed in our work well match those resulting from Makrodimitri's simulations for what concerns both peaks shape and position. Once again, peaks enhance moving from PDMS20 to PDMS7.
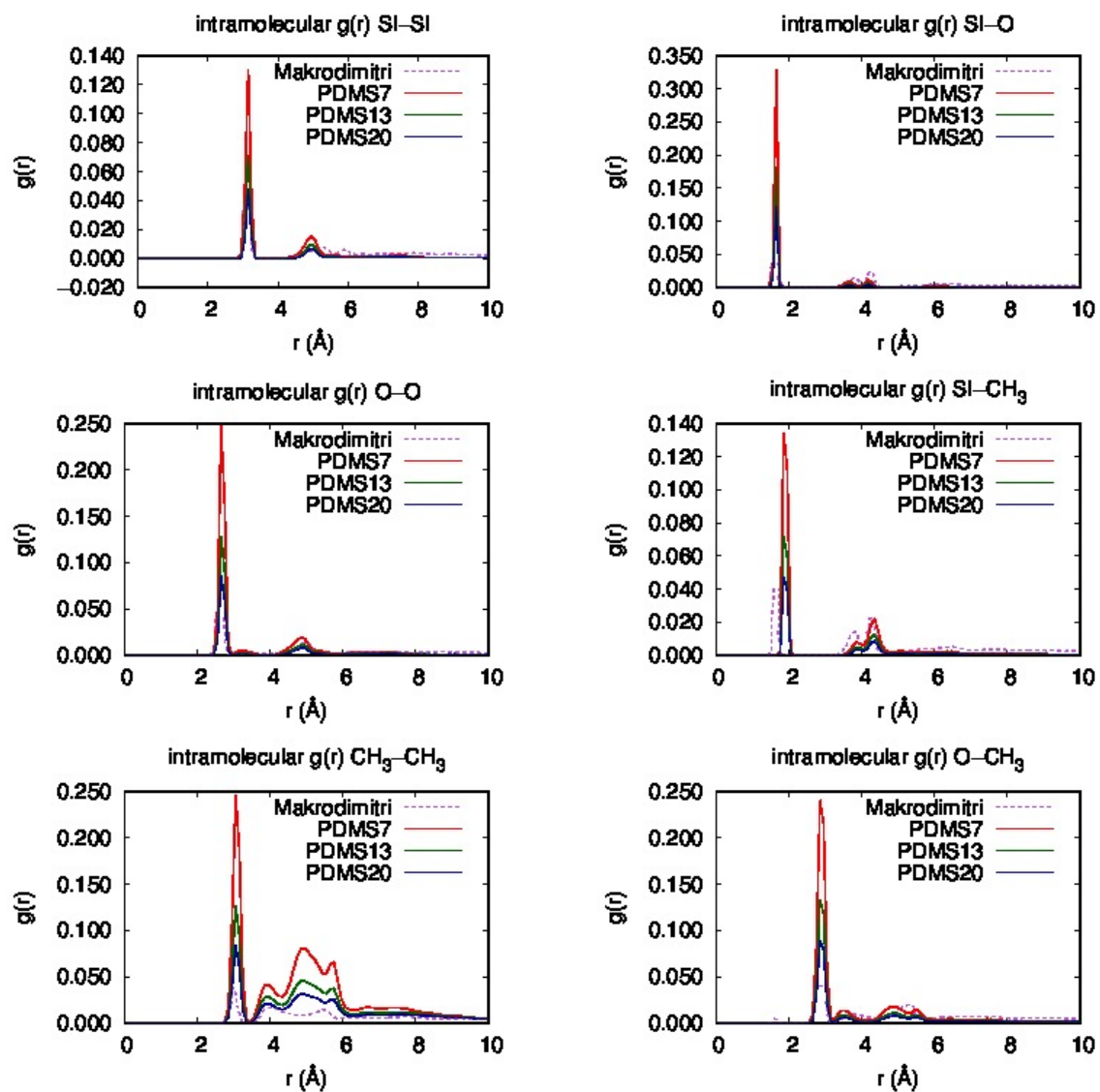
Figure 2.3: Intramolecular $g(r)$ for each possible atom types couples, for PDMS7, PDMS13 and PDMS20 samples, and Makrodimitri's.
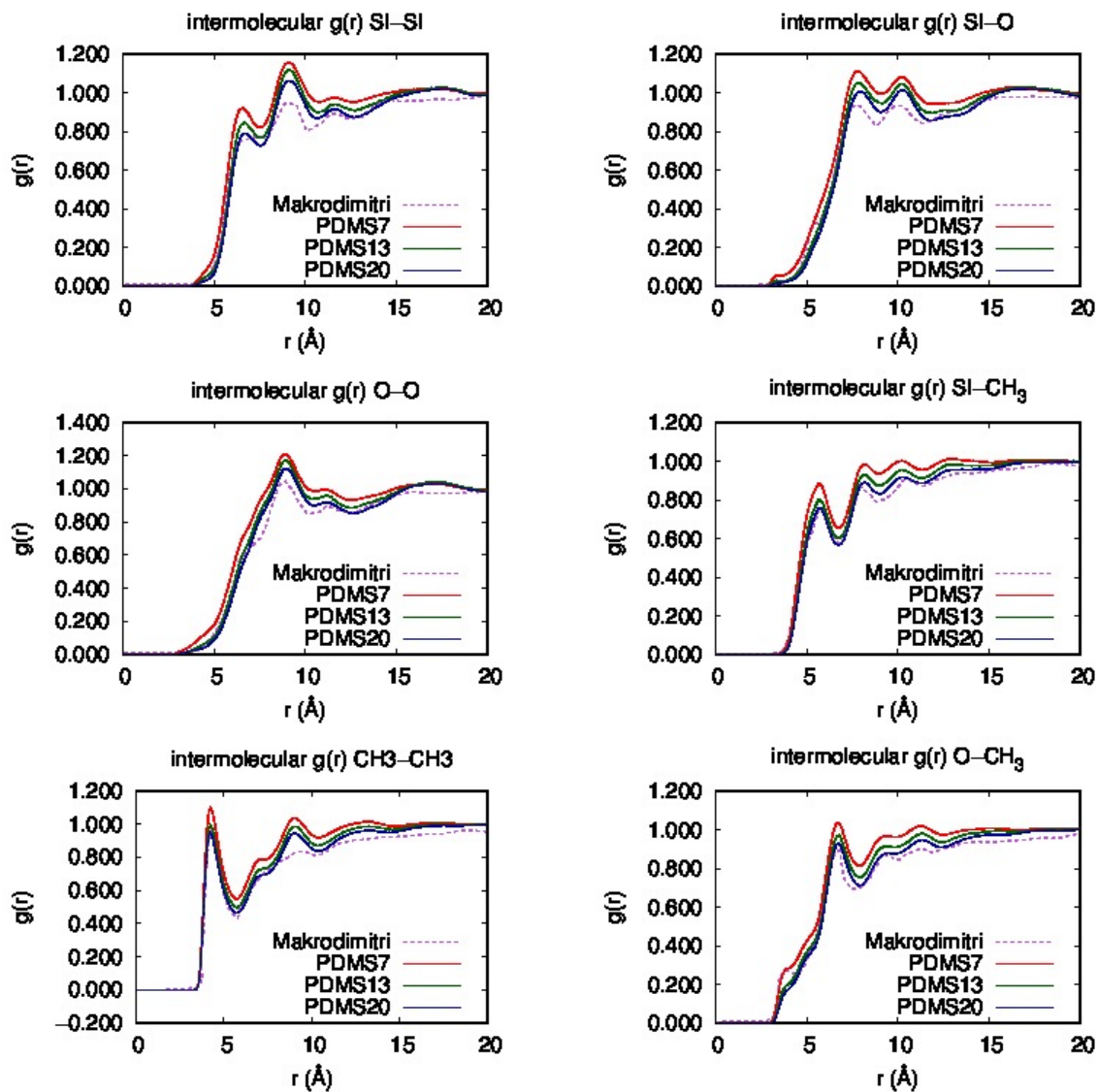
Figure 2.4: Intermolecular $g(r)$ for each possible atom types couples, for PDMS7, PDMS13 and PDMS20 samples, and Makrodimitri's.

2.3 End-to-end distance distribution

In order to understand chains conformation, end-to-end distance has been calculated, defining it as the distance between the Si atom of the first residue of a chain and the O atom of the last residue of the same chain. Taking 1.64 Å for SI-O distance and 109.5° for O-Si-O angle (i.e. values of Makrodimitri's FF), we would ideally have, for straight chains, the following lengths:

- PDMS7: 17.41 Å

- PDMS13: 33.48 Å

- PDMS20: 52.23 Å

For each sample, the measurement has been done on all chains and then distribution of values was computed, counting the number of chains lying in a certain range of distance (it is not a real probability, since it is not normalized). The calculation of end-to-end distance was performed by a script that, for each chain of the sample, takes coordinates related to the Si atom of the first residue and those of the O atom of the last residue, than computes:

$$r_{Si-O} = \sqrt{(x_{Si,1} - x_{O,n})^2 + (y_{Si,1} - y_{O,n})^2 + (z_{Si,1} - z_{O,n})^2} \qquad (2.1)$$

where n is the number of residues per chain (7, 13 or 20). Histograms in Table 2.5 show end-to-end distribution for the samples of PDMS7, PDMS13 and PDMS20 at 300 K and 1 bar. As we expected, chains folded in some extent, giving, on average, lower end-to-end distances than those predicted for linear chains. For PDMS7 sample the maximum is about at 11 Å, for PDMS13 it lies at 20 Å, while for PDMS20 it is not easy to find a most probable end-to-end distance value. Maybe it is due to the fact that, being the chains longer, a huge number of conformations is possible, thus a larger range of end-to-end distance is allowed, resulting in a uniform probability of occurrence.
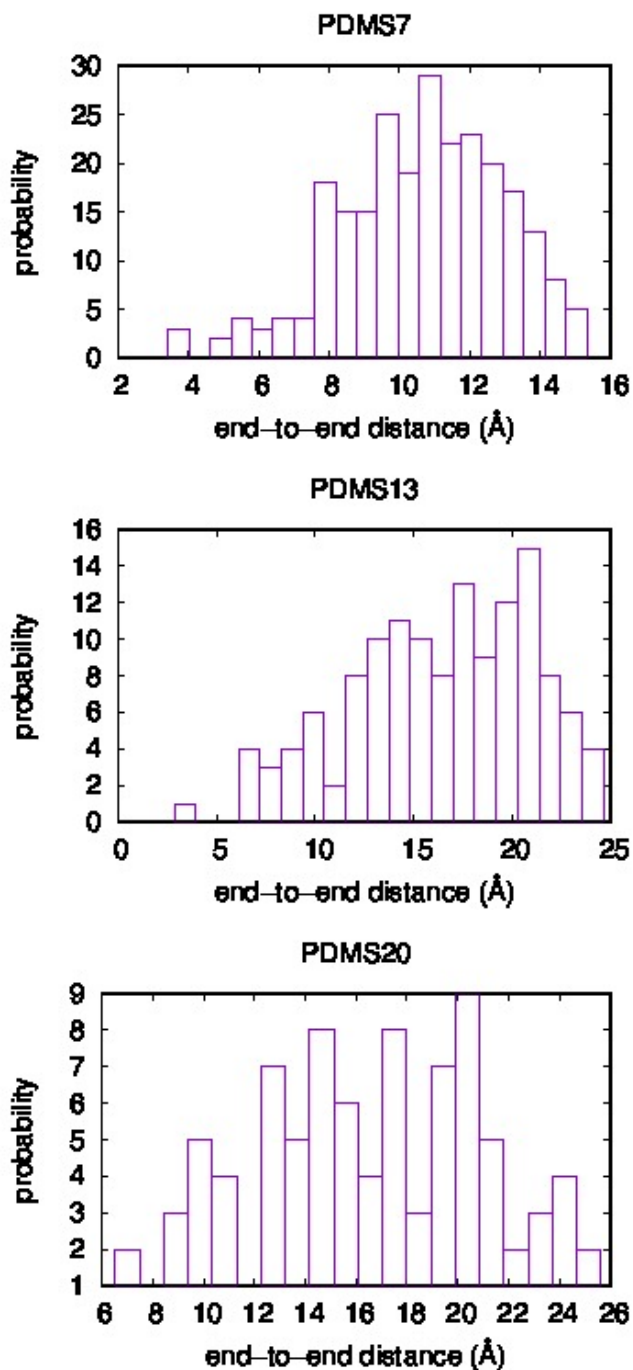
Figure 2.5: End-to-end distance distribution for PDMS7 (top), PDMS13 (center) and PDMS20 (bottom) samples, at 300 K and 1 bar.

2.4 Radius of gyration distribution

In addition to end-to-end distance, another parameter useful for getting information about conformation of a polymeric chain is the gyration ratio [5], defined as:

$$R_g^2 = \frac{1}{n} \sum_{i=1}^{n} (\mathbf{R}_i - \bar{\mathbf{R}})^2 \tag{2.2}$$

where $\mathbf{R}_i$ is the position of the center of mass of the i-th monomer, while $\bar{\mathbf{R}}$ is the average position of the centers of mass of the n monomers composing the chain. Analogously to end-to-end distance, high R_g^2 values state that the chain is straight, while low values of R_g^2 mean that the chain is in a folded conformation. Also for gyration ratio, a distribution profile has been computed. However, while end-to-end distance takes into account only the first and the last residue of a chain, neglecting other residues, gyration ratio considers all residues, giving information on how close they are with respect to the center of mass of the whole chain. In other words, while end-to-end distance represents how near the head and the tail are, the gyration ratio defines the volume occupied by the chain. Results from our simulations are reported in Table 2.6 below. As it can been seen, for PDMS7, the histogram is quite bell-shaped, with a maximum at 16 Å. PDMS13 exhibits a more fluctuating trend, with an absolute maximum at 44 Å. In PDMS20, instead, distribution seems to be bimodal, with maxima at 50 Å and 80 Å.
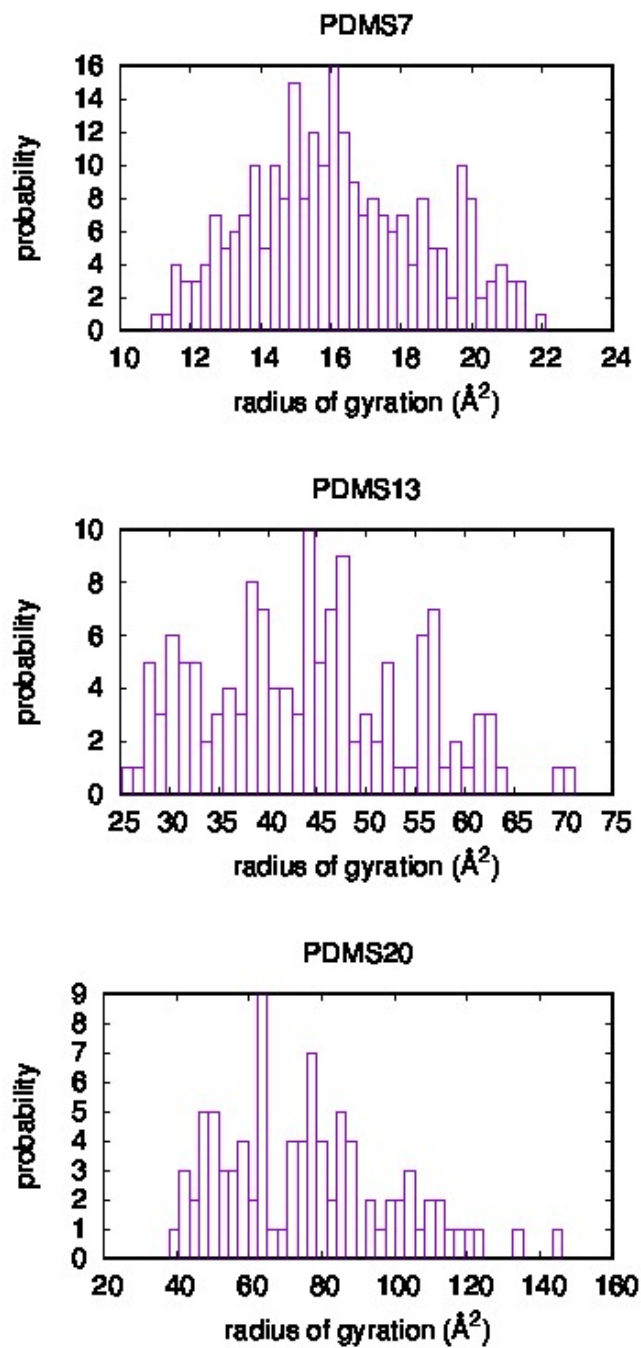
Figure 2.6: Gyration ratio distribution for PDMS7 (top), PDMS13 (center) and PDMS20 (bottom) samples, at 300 K and 1 bar.

2.5 Dihedral angles distribution

Another important aspect that was investigated is the dihedral angles distribution: the presence of substituents on atoms belonging to the main chain is one of the reasons why polymeric macromolecule are not linear, but folded. Steric hindrance caused by side groups obliges single monomers to rotate one respect to the other in order to increase the distance between side groups themselves. This effect is negligible only in the case of polyethylene, where side groups are hydrogens. In other cases, rotation of monomers occurs. This mirrors in dihedral angles values. In the specific case of PDMS, side groups are methyls, quite hindered. On the other hand, on the contrary of organic main chain polymers, in PDMS main chain an alternation of Si and O atoms is observed. Since oxygen has not ligands, silicon side groups are far from each others. This feature balances big size of methyls. In our work, we computed Si-O-Si-O dihedrals through VMD, taking data from about the last 10 ns for each simulation. As we did for end-to-end distance and radius of gyration, we did not calculate a real distribution, instead we simply divided the range from -180° to 180° in gaps wide 2° and counted the number of dihedral angles lying in each gap. Results are shown in Figure 2.8. For all samples, it can be observed that the region around 0°, which corresponds to a *cis* conformation is the less populated. Interestingly, the absolute maximum is not at -180° and 180°, i.e. the *trans* configuration, instead it is around -120° and 120°, which corresponds to gauche^{-} and gauche^{+} conformations, respectively (Figure 2.7). It is worth noticing that, moving from PDMS7 to PDMS20, local maxima at -160° and 160° appear. Moreover, in PDMS7 local maxima at -50° and 50° are observable, while they gradually get lower moving from this sample to PDMS13 to PDMS20.
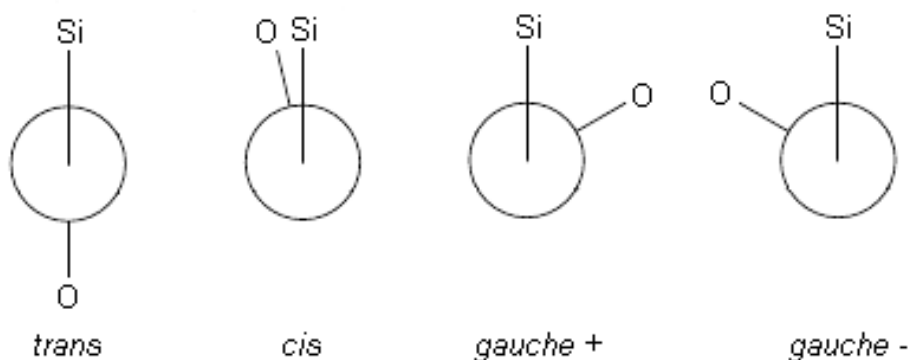

Figure 2.7: Newman's projections of some dihedral configurations for PDMS.
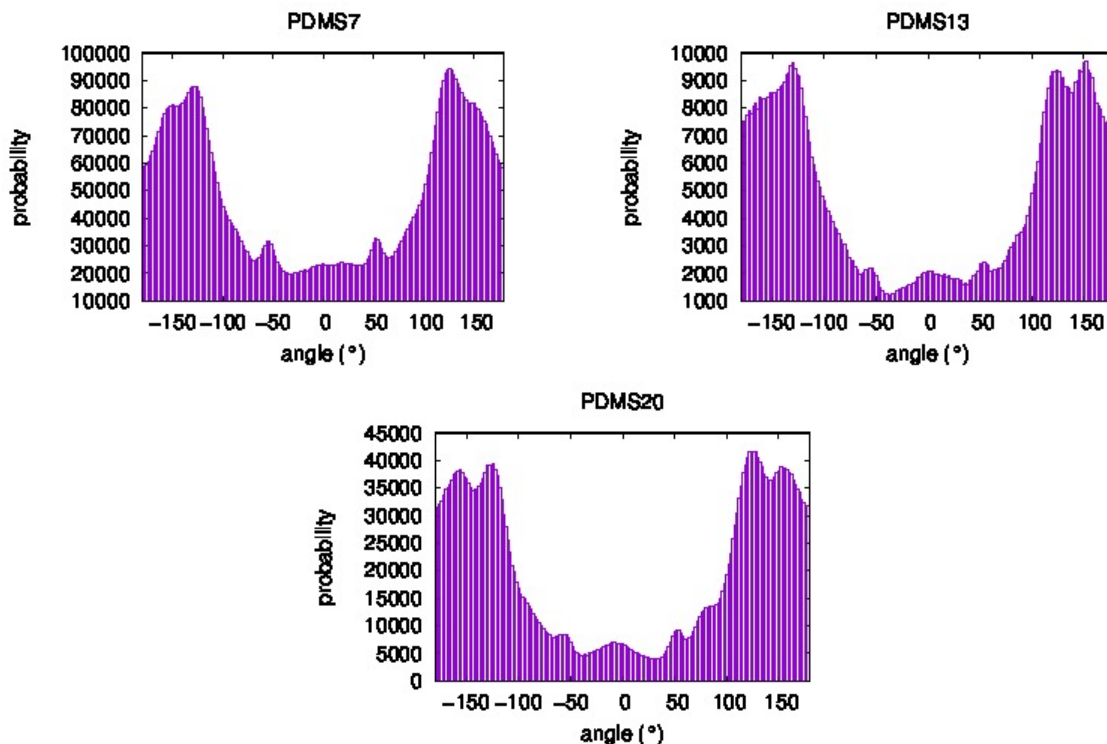
Figure 2.8: Dihedral angles distribution for PDMS7 (top left), PDMS13 (top right) and PDMS20 (bottom) samples, at 300 K and 1 bar.

2.6   Surface roughness computation

Previous works carried out by our group showed how important surface morphology is in order to determine the overall effect on liquid crystal molecules interaction with the surface itself. A particular superficial feature can affect LCs orientation as well as energetic aspects do. In a simulation regarding interaction between 5CB and PMMA and PS surfaces, respectively, Palermo et al. [5], from University of Bologna, discovered that, if the surfaces are rubbed along a direction, two different phenomena can be observed. In both cases anchoring is planar, but PMMA induces 5CB alignment along the rubbing direction, while in the case of PS, alignment is perpendicular with respect to the rubbing direction. The reason was found in the presence of phenyl groups, which create kinds of channels where 5CB takes place. In another work carried out inside our group, Roscioni et al. [4] found that the alignment of 5CB on self-assembled monolayers (SEMs), formed from octadecyl- and/or hexyltrichlorosilane (OTS and HTS) attached to glassy silica, depends on the ratio between OTS and HTS. A full coverage of OTS induce planar alignment, since 5CB "sees" a flat surface. On the other hand, if the coverage is performed through a mixture of OTS and HTS, homeotropic anchoring arises, due

to the fact that the surface generated by differently long alkyl chains acts as a comb where 5CB can penetrate. Both these publications cited highlight that it is the surface morphology, and not an energetic aspect, that affects the LC orientation observed. This consideration suggested to analyze the surface of our PDMS samples, in order to understand if a relation exists between its structure and the 5CB homeotropic anchoring observed in experimental works. Maybe the most important feature regarding a surface is roughness, which can be defined as the average height of the points on the surface with respect to a plane, taken as reference, i.e. points belonging to the plane have a height equal to 0, (Figure 2.9):

$$R_a = \frac{\sum_{i=1}^{n} |y_i - y_{plane}|}{n} \tag{2.3}$$

where n is the number of points considered on the surface, while y_i is the height of the i-th point and y_{plane} is the height of the reference plane. Roughness computed through this expression is called "mean roughness" [57]. Anyway, other definitions are possible, one of which is the "mean square roughness" [57], calculated as:

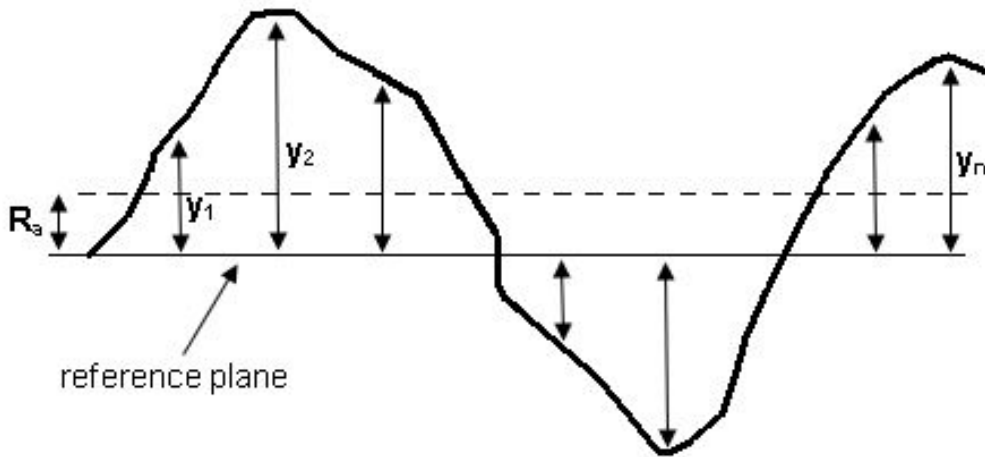$$R_q = \sqrt{\frac{\sum_{i=1}^{n} (y_i - y_{plane})^2}{n}} \tag{2.4}$$

Figure 2.9: Graphic representation of mean roughness (Equation 2.3). A vertical section of a surface is shown. Reference plane is perpendicular to the sectioning plane.

Whatever equation is used, it is clear that the bigger n is, the better the roughness computed will be. The exact value would be obtained with $n \to \infty$. In practice, a sampling of the surface is performed, building a grid (with a certain pitch p) on it, and considering only the nodes of
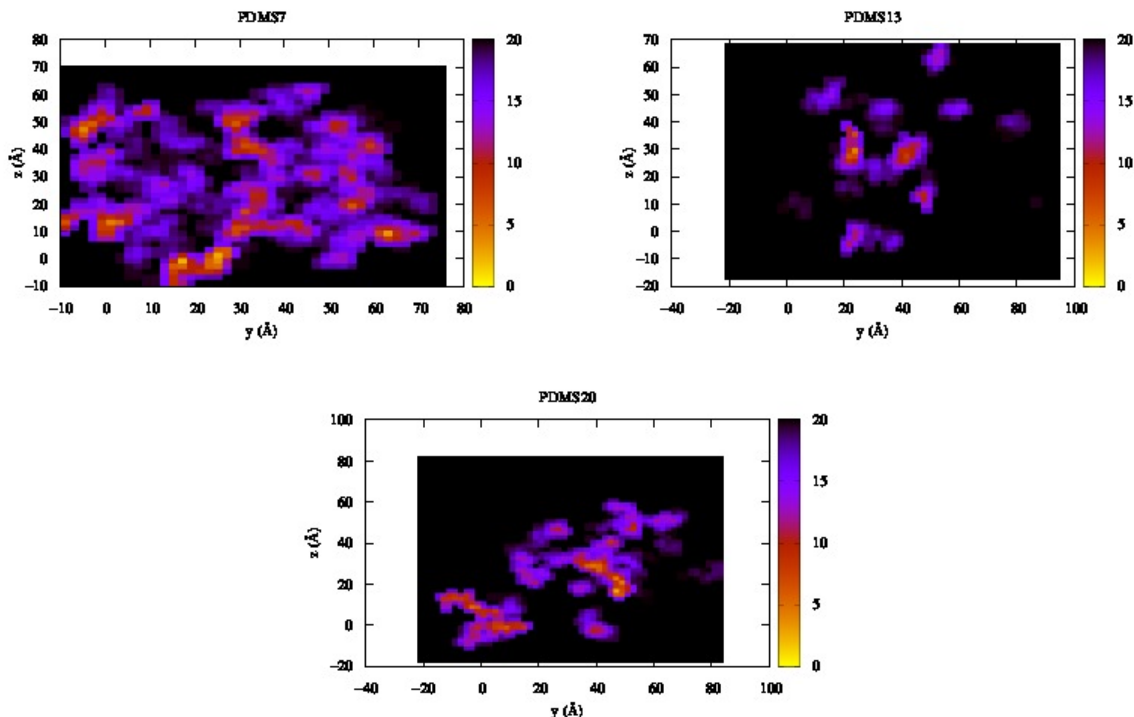
Figure 2.10: Surface coloured map for PDMS7 (top left), PDMS13 (top right) and PDMS20 (bottom) samples, at 300 K and 1 bar. Depth is codified by the palette beside each plot: black is for maximum depth (20 Å in our case), yellow is for the minimum depth (0 Å).

the grid for the computation of roughness. Since lower p values mean higher n, it is obvious that a little pitch ensures better results. In our work, we applied this method, using a pitch of 2 Å. The choice was suggested by the fact that, in AFM techniques for surface analysis, probes of such dimension are usually employed. Reference plane was set at a depth of 20 Å with respect to the box side. Roughness was computed on every side of the simulation box, using the same parameters reported above. In Table 2.10, coloured maps of top x surfaces of each sample are shown, where colours denote a specific depth. In Table 2.1, instead, values of R_a and R_q for the three samples are reported. As we expected, PDMS7 is the sample with the lowest roughness. Since chains are shorter, a better packing can be achieved, which in turn results in a flatter surface. Increasing chain length prevents an optimal volume occupation, hence the surface will result more rambling (and roughness gets higher). On the other hand, no substantial change in surface roughness is observed passing from PDMS13 to PDMS20. Nevertheless, R_a and R_q decrease a little.

Analysis carried out on the three samples highlighted that shorter chains are responsible

	R_a (Å)	R_q (Å)
PDMS7	47.3872	29.6811
PDMS13	176.742	64.2815
PDMS20	162.273	61.5371

Table 2.1: R_a and R_q values for PDMS7, PDMS13 and PDMS20 samples at 300 K and 1 bar.

for a more ordered bulk structure, as shown from the computation of radial distribution function. Increasing chain length causes steric hindrance to get higher, thus a lower freedom for molecule to move. This reflects in a worst packing ability, as came out from surface roughness calculation. On the other hand, greater length also means a huger number of conformations possible, as shown by end-to-end, radius of gyration and dihedrals distribution.

Chapter 3

Interaction between PDMS and water

3.1   Surface tension

As previously said, both Xia [8] and Suh [52] stressed out the fact that PDMS low surface tension could be the reason of homeotropic anchoring of 5CB, however without giving any evidence. Surface tension of a material is defined as the mechanical work that has to be done in order to make the surface of that material increase of an infinitesimal extent [58]:

$$\gamma = \frac{dW}{dA} \tag{3.1}$$

where dW is an infinitesimal work, and dA is a infinitesimal change in surface area. Hence, despite of its name, surface tension is not a tension (i.e. a force), but it is measured as an energy per unit area (J/m^2) or, analogously, as a force per unit length (N/m). Thinking about a liquid, the definition of γ given in Equation 3.1 is quite clear. Everyone has certainly seen a water drop lying on a leaf (Figure 3.1): the shape of the drop is approximately spherical, neglecting the soft flattening due to gravity.

The sphere is the shape with the lowest surface area: in absence of external forces, liquids aim

Figure 3.1: A water droplet lying on a leaf. Spherical shape is due to surface tension effect [59].

at reaching this shape, since the lowest surface area also means the lowest surface energy. The reason of this phenomenon lies on the particular condition of particles at the surface. While bulk molecules are subjected to attraction forces in all directions by neighboring molecules, which results in a null resultant force, surface molecules are overall attracted inwards, since there are no molecules above them. Thus, the resultant force acting on them will not be 0 (Figure 3.2). As a consequence, the system will evolve to expose the lowest number of molecules at the surface as possible. [58]. In other words, the reason of surface tension existence lies in cohesion forces, i.e. attraction forces acting on particles of the same type.

However, a surface is always an interface between two distinct materials. This means that
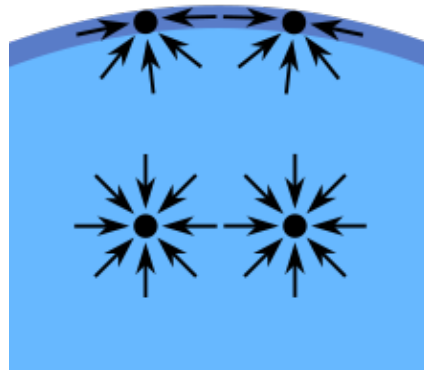

Figure 3.2: Graphic representation of surface tension origin. Black arrows represent intermolecular forces [60].

surface molecules are not only subjected to cohesion forces generated by molecules of the same material, but also adhesion forces due to the other material will act. Depending on which of these two interaction prevails, two different cases can arise. Let us consider again the water drop on the leaf. In this case, the attraction performed by molecules constituting the leaf surface is negligible with respect to cohesion forces among water molecules. For this reason, spherical shape occurs. On the other hand, if the water drop is placed on a glass surface, the drop is observed to flatten. This is due to the fact that, this time, silica molecules attraction towards water is not negligible, and competes with cohesion forces, causing the sphere to deform [58]. Consequently, the contact area between the two materials increases. A criterion to establish if water will wet or not a surface made of a certain material is to compare their surface tensions. If $\gamma_{water} > \gamma_{material}$, then cohesion forces will prevail on adhesion, and the water drop will not wet the surface. On the other side, if $\gamma_{water} < \gamma_{material}$, water molecules will be greater attracted by the material than by themselves, thus the drop will wet the surface.

Materials with a surface tension lower than water are called *hydrophobic*, while the ones with a greater surface tension than water are defined *hydrophilic*. Since PDMS γ is about 20 mJ/m^2, as reported by Xia et al. [8], while water γ is known to be 73 mJ/m^2, we expect PDMS to have a hydrophobic behaviour.

Wettability of a solid surface can be quantified defining the contact angle [58], which is the angle formed from the solid surface and the straight line tangent to the liquid drop in the point of coexistence of gas, liquid and solid phases, as shown in Figure 3.3. Contact angle can be obtained through Young's equation:

$$\gamma_s = \gamma_{sl} + \gamma_l \cos \theta_0 \tag{3.2}$$

where γ_s, γ_l and γ_{sl} are the surface tension of solid phase, liquid phase and at the solid-liquid interface, respectively, while θ_0 is the contact angle.
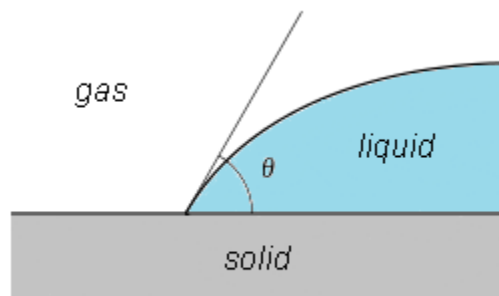

Figure 3.3: Contact angle of a liquid droplet on a solid surface.

3.2 Simulation features

In our work, we studied the interaction occurring between PDMS samples generated before and a water droplet, in order to verify if Makrodimitri's FF [51] is able to reproduce hydrophobic behaviour of PDMS. Some computational works on this point had already been carried out. For example, Ismail et al. [61], after having developed a home-made FF for PDMS melt, performed MD simulations placing a spherical water droplet on a PDMS surface. The results they obtained were in good agreement with experimental data, giving a contact angle of 108°, while values comprised between 98° and 112° arise from experimental measurements.

In their work, water was parameterized through the Extended Single-Point Charge (SPC/E) model [62], and a spherical shape was chosen for the droplet. In our work, we chose, from the several computational models available for water, the Transferable Intermolecular Potential with 3 Points (TIP3P) [63], described in Table 3.1 (in comparison with SPC/E). In this model, force constants for stretching and bending potential are really high: for this reason big fluctuations from equilibrium distances and angles are prevented. In other water models instead, such as the SPC/E one, force constants are chosen to be infinite, which means that in single water molecule, hydrogens and oxygen are fixed with respect to each other, being forbidden to move out their equilibrium geometry [62]. Nevertheless, such a potential is called rigid, while models as TIP3P, where molecular geometry can change, are known as flexible. In addition to

	stretching		bending		electrostatic		Lennard-Jones	
	r_{O-H} (Å)	$k_l \left(\dfrac{\text{kcal}}{\text{mol Å}^2} \right)$	θ_{H-O-H} (°)	$k_\theta \left(\dfrac{\text{kcal}}{\text{mol rad}^2} \right)$	q_O (e)	q_H (e)	A $\left(\dfrac{10^3 \text{kcal Å}^{12}}{\text{mol}} \right)$	B $\left(\dfrac{\text{kcal Å}^6}{\text{mol}} \right)$
TIP3P	0.9572	450.0	104.52	55.0	-0.834	+0.417	582.0	595.0
SPC/E	1.0	/	109.47	/	-0.8476	+0.4238	629.4	625.5

Table 3.1: TIP3P and SPC/E parameters for water.

the different Force Field we employed for water with respect to Ismail [61], our simulations differed also for the initial shape of the droplet. We decided to start from a cubic droplet (instead of spherical), which is a very unstable shape, since edges represent zones where energy is very high. The purpose, starting with this condition, was to follow the change in time of the droplet shape.

Simulations were carried out by taking one of the PDMS samples described in Chapter 2 and using it to generate a surface. The method followed is quite simple, taking advantage of PBC of MD simulation. It consisted in building a simulation box with x and y sides equal to x and y dimensions of the sample, while for z side a length 100 Å greater than z dimension of the sample was chosen. Then the sample was centered with respect to z direction, so that there were 50 Å void above and below it. In this way, replicas within the xy plane were in contact with each others, creating a unique surface, while replicas along z direction were 100 Å distant one to the other. The overall effect was that PDMS chains formed layers parallel to z direction and far enough not to interact with each other even if PBC were used for all three axes. Starting from a sample of size 60 Å× 60 Å× 60 Å, the simulation box resulted 60 Å× 60 Å× 160 Å. Of course, such a simulation had to be performed in NVT ensemble, since box

size must remain unchanged in time. As a consequence, pressure varied in order to keep volume constant. Before running the simulations, the water sample had to be generated. A single water molecule was drawn with Avogadro [64], than Packmol [54] was employed to create a sample of 2000 molecules. A NPT simulation was carried out on this sample at 300 K and 1 bar until it reached constant volume (and hence a constant density). Then, through Outside, a cubic droplet containing 400 molecules was cut from the equilibrated sample. The resulting cube side was 20 Å. On one hand, choosing a more little cube would have made it difficult to appreciate the shape of the droplet. On the other, a bigger cube could have interacted with its replicas on the xy plane. The droplet was then placed on the PDMS surface and simulations were performed in NVT at 300 K, with a production time of 100 ns.

3.3 Results

As first attempt, we tested surfaces prepared from PDMS7 and PDMS20 samples, respectively. Figure 3.4 shows the evolution in time of the system composed by the PDMS7 surface and the water droplet. Before running the simulation, the water cube lied on the polymeric layer. What unexpectedly happened, as soon as the simulation started, the droplet exploded, causing water molecules to spread all over the box. Then, after some production time, water molecules began to condense on the PDMS surface, forming spheroidal clusters. The fact that two water masses arose was due to PBC, which caused water molecules to disappear from the top of the box and reappear on the bottom. The explosion of the droplet has not been well understood. However, a negative pressure of about -54 bar has been recorded at the beginning of the simulation, which justifies the phenomenon occurred. With that pressure, and at 300 K, liquid water is not in a stable state, so the explosion could be due to the initial conditions inside the box. What is maybe even surprising is that water spheres formed do not remain on the PDMS surface, but penetrate partly inside the polymer, creating a basin in PDMS, however without mixing with it. It could be seen as a kind of emulsion where, despite of conventional emulsions, water acts as dispersed phase, while PDMS represents the bulk phase. Nevertheless, we have to take into account that, at 300 K, linear PDMS is substantially a liquid (even if quite viscous), so it is possible for it, in some extent, to be penetrated. Moreover, chains length is only 7 units, which is an additional reason for chain themselves to flow quite easily. The absence of mix-

ing between water and PDMS states, in some way, that PDMS has a hydrophobic behaviour. However, it is not clear why the two substances do not remain completely separate one from the other. What is evident is that water-PDMS interaction is preferred (energetically convenient) to water-void interaction. It is not fully absurd to observe such a phenomenon between a hydrophobic material and water, since van der Waals forces are always present, and they are attractive. In addition, we must not forget that the system studied is nanosized: we are used to observe the macroscopic behaviour of water on a hydrophobic surface, but we do not know what the result would be employing a microscopic droplet. The great difference lies in the fact that the latter sees molecular roughness, not perceivable by a macroscopic object.

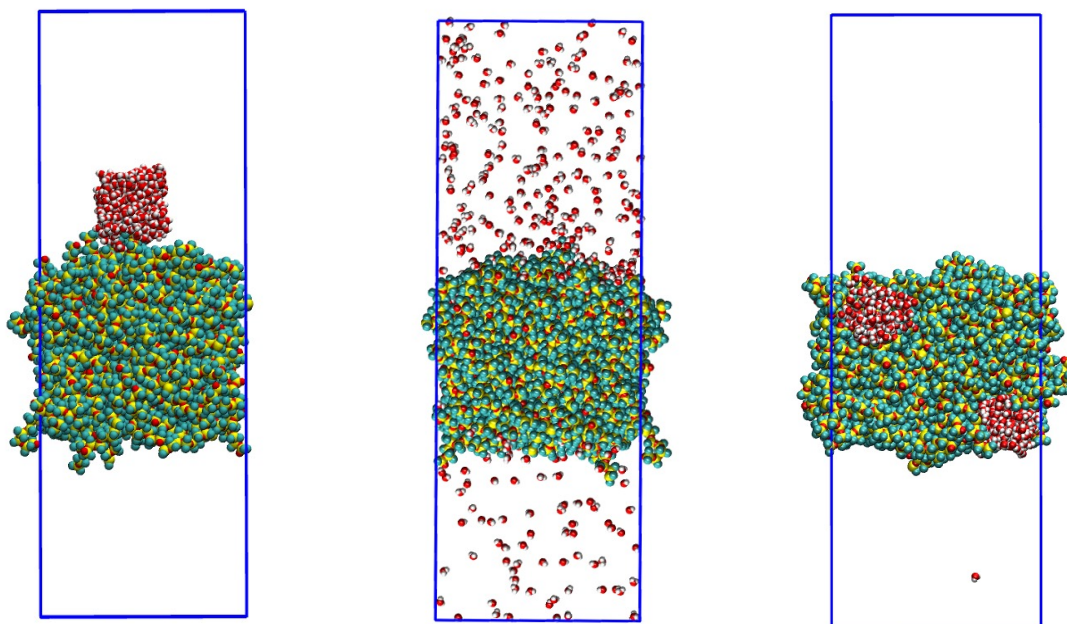A slightly different situation arises from the simulation carried on with PDMS20 instead of

Figure 3.4: Evolution in time of the system PDMS7-water. Left: system before starting the simulation. Middle: system after few ps of simulation. Right: system at the end of the simulation. Silicons are shown in yellow, oxygens in red, carbons in light blue, and hydrogens in gray.

PDMS7. Since chains are longer, their motion is more hindered. This feature mirrors in a lower ability of water spheres to penetrate inside PDMS. On the other side, PDMS20 surface is rougher than PDMS7, exhibiting by its own some dells where water can take place. As happened for PDMS7, also in this case, water cube explosion occurred as soon as simulation began. Then water molecules condensed on the PDMS20 surface. Figure 3.5 shows a detail of the system PDMS20-water at the end of the simulation: as it can be seen, the water droplet has
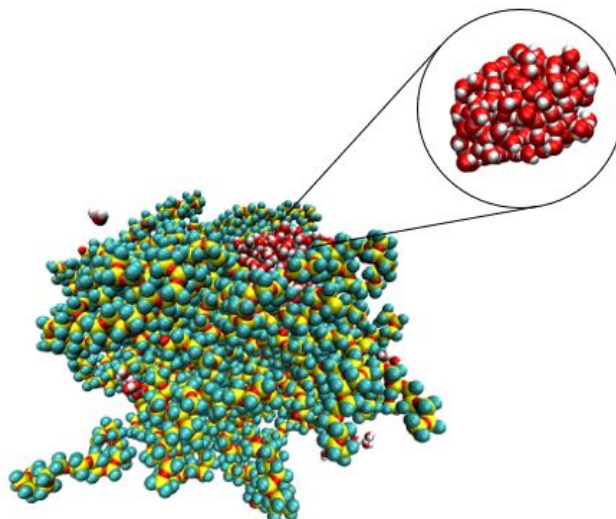
Figure 3.5: Detail of PDMS20-water system at the end of the simulation and the water droplet shape that arose. Silicons are shown in yellow, oxygens in red, carbons in light blue, and hydrogens in gray.

about half penetrated in PDMS, while the other half is exposed to void. The isolated droplet is also represented, in order to take a better look at its shape.

In order to understand the behaviour of water in contact with a solid PDMS surface, we decided to repeat the simulation, this time keeping the position of PDMS chains backbones fixed. This option has been pursued indicating in NAMD [12] input file to fix silicon and oxygens atoms belonging to PDMS. Preventing backbones movement is a fast and simple way to "solidify" PDMS, without needing to modify its structure through cross-linking. At this purpose, a linear chains PDMS sample was prepared. In order to fulfill this operation, a single chain, 26 units long, was generated in the same way the "mother" chains of PDMS7, PDMS13 and PDMS20 samples have been generated. Through another script, this chain (oriented along x direction) has been replicated 17 times along y direction and 3 times along z direction, so that, at the end, the sample was made of $17 \times 3 = 51$ chains. Length of chains and number of replicas along y and z direction were chosen in order to have a sample with about the same dimensions of the ones prepared previously. For this new sample (which we will call PDMS26 from now on), no equilibration phase has been carried out, since the aim was to keep chains straight, but just a minimization. Then, the water droplet (the same used for other simulations) was placed on it, and a NVT simulation was performed for about 60 ns. As for other cases, the water cube exploded at the beginning of the simulation, then molecules began to aggregate. What occurred in this simulation is shown in Figure 3.6. As it can be observed, water

molecules do not form a cube anymore, but the shape that resulted is a squashed sphere. The fact that a not perfect sphere has been obtained suggests that some attraction between water and PDMS occurs anyway. However, since water molecules did not look for wetting the widest PDMS surface as possible, we can definitely state that PDMS has a hydrophobic behaviour.
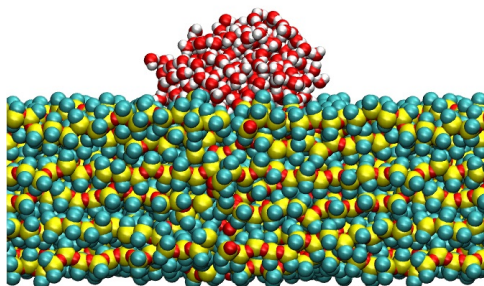

Figure 3.6: Water droplet on PDMS26 surface (with backbones fixed). Silicons are shown in yellow, oxygens in red, carbons in light blue, and hydrogens in gray.

Since in this case we dealt with a flat surface, it was reasonable to measure the contact angle (Figure 3.7). For this purpose, we selected a section from the water droplet along y direction, taking into account oxygen atoms lying on that xz plane. We then fitted their coordinates with a polynomial function of degree 3 (employing Microsoft Excel) and calculated the first derivative at the point of coexistence of water, PDMS and void: an angle of 133 ° resulted. Of course, such a method is quite sketchy, thus the value obtained can not be taken as an accurate esteem. This is indeed quite different from the angle of 108 ° obtained by Ismail [61]. It is rather worth to put in evidence that the angle computed is greater than 90 °, corroborating the hydrophobic nature of PDMS.
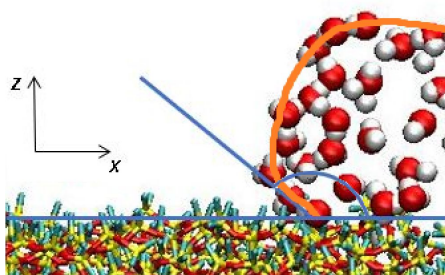

Figure 3.7: Contact angle of water on PDMS26 surface.

Chapter 4

Interaction between PDMS and 5CB

4.1   5CB sample preparation and Simulation features

In a way similar to that adopted for the analysis of water interaction with a PDMS surface, we prepared the systems composed by PDMS and 5CB. First of all, a 5CB sample of 250 molecules was generated with Packmol, and equilibrated at 300 K and 1 bar. The Force Field employed is the one developed by our group [1]. Since the nematic to isotropic transition (T_{NI}) of 5CB is about 308 K [29], and operating temperature was lower than this, a nematic phase resulted after equilibration. Figure 4.1 shows an image of 5CB bulk obtained by our simulations. As it can be observed, molecules are oriented along a preferential direction (molecules represented with the same colour are oriented within the same direction). Order parameter $\langle P_2 \rangle$ was computed through Outside, giving a value of 0.596, with respect to the director $\vec{n}$ =(0.09783;-0.76601;0.63534). This one is esteemed by Outside as the mean, over all molecules, of their main axes (defined through a triad of atoms, in our case N1, C6 and C12).

After a production time of 15 ns, the sample was replicated and then cut in order to build a 5CB column composed of 1000 molecules, with the base as wide as the PDMS surface. The column was placed on the top of the PDMS sample, and a simulation box was built, starting from a cell of the same size of the system PDMS-5CB, then extending its height of 100 Å leaving 50 Å of vacuum both above and below the system. Once the system was ready, we launched simulations in NVT ensemble at 300 K, letting them run for about 50 ns.
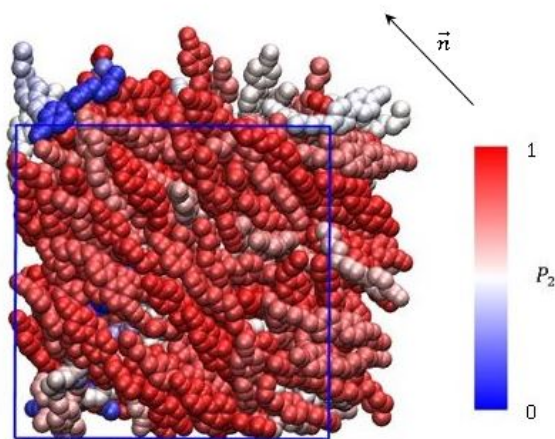
Figure 4.1: Rendering of a 5CB sample at 300 K and 1 bar. Colors indicates order parameter P_2 of molecules, according to the palette on the right. The simulation box is shown in blue. Director $\vec{n}$ is represented by the black arrow.

4.2 Results

The first sample we tested with 5CB was PDMS7. After a few ns of equilibration, we observed an unexpected phenomenon: some chains from the PDMS surface had torn away from it and were dissolved in the 5CB phase. At the same time, some 5CB molecules had penetrated throughout the PDMS surface, occupying void space left from not an efficient packing. In this way it was not possible to identify a well defined interface for studying the interaction between the two substances. However, we found that, near PDMS, 5CB molecules lost their alignment, while it was preserved far from the polymer (Figure 4.2, left). Repeating the simulation with PDMS20 sample, we managed to avoid the detachment of chains from the polymeric surface, probably thanks to the fact that longer chains are more impeded to move, since they are more tangled. Anyway a considerable amount of 5CB molecules had penetrated inside PDMS, suggesting that a chemical affinity between these two substances must exist. As for PDMS7, also in this case, 5CB orientational order was lost nearby the PDMS surface, while it was preserved at the void-exposed side (Figure 4.2, right).

In order to better quantify the rise of disorder in 5CB approaching the PDMS surface, order parameter $\langle P_2 \rangle$ for both samples was computed along z axis, as shown in Figure 4.3. The plot was obtained employing Outside, which allows to compute order parameter in regions with respect to a certain direction. The director is reassigned in each region depending on the average orientation of molecules in that layer. Both 5CB-PDMS7 and 5CB-PDMS20 systems exhibit
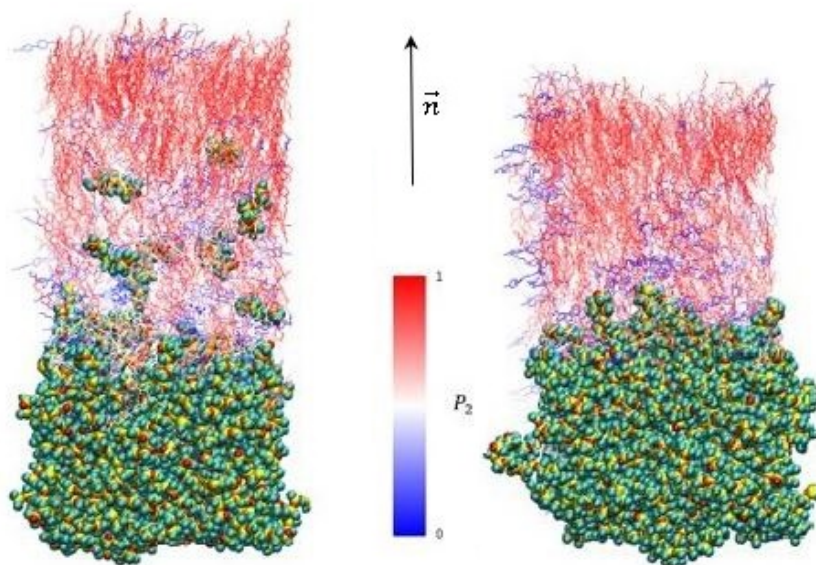
Figure 4.2: 5CB on PDMS7 (left) and PDMS20 (right). For 5CB molecules, colour represents orientation, according to the palette on the right. Director $\vec{n}$ is represented by the black arrow.

very low $\langle P_2 \rangle$ nearby the polymeric surface, around 0.2, which is well below the value we calculated for the nematic 5CB we started with ($\langle P_2 \rangle = 0.596$). This means that the interaction with PDMS caused 5CB to undergo a transition from nematic to isotropic phase. Far from the PDMS surface, instead, for both systems 5CB is still nematic, as highlighted by high values of $\langle P_2 \rangle$. The problems highlighted by the simulations on the PDMS7-5CB and PDMS20-5CB systems suggested that the PDMS employed was not suitable for our purpose, since it owned the features of a liquid, especially in case of short chains (PDMS7). Mobility of chains was too high, causing the surface not to be well defined. It became clear that, if we wanted to simulate a real PDMS surface behaviour, scrolling of chains had to be avoided. One possible solution was to fix backbones positions (an option available in NAMD, as already seen). This should have been certainly the simplest way to obtain a solid-like surface, since it does not affect the chemical structure of the sample. Anyway, such a method does not properly represent what happens in reality. PDMS, in fact, is never employed as a glassy material, where molecules are forbidden to flow, being allowed only to slightly vibrate around their position. This polymer is instead used as an elastomer, which means that chains can move in some extent, even if partly bonded. In order to obtain a more faithful to reality simulation, we chose to reproduce a cross-linked PDMS surface. As first step, we generated a sample composed of 3 chains, each made of 80 units (following the same method described for other samples).
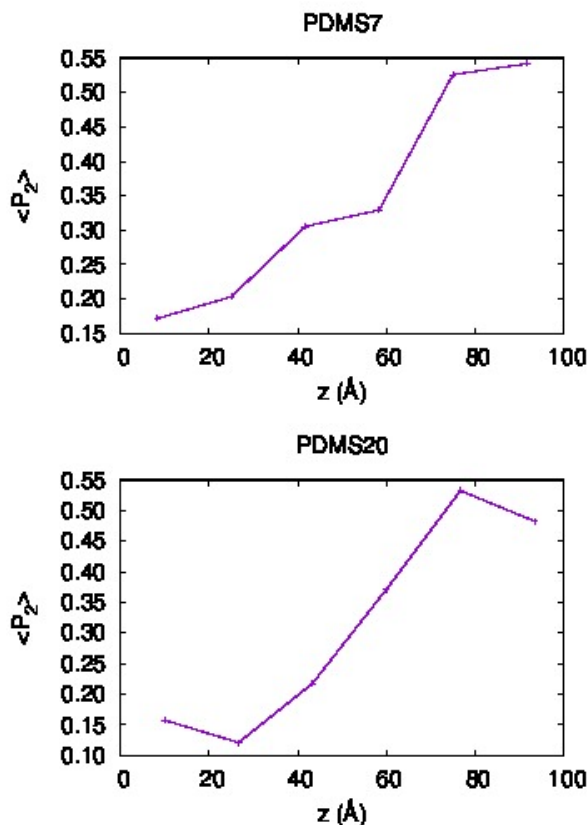
Figure 4.3: Order parameter $\langle P_2 \rangle$ computed along z axis for 5CB placed on PDMS7 (top) and PDMS20 (bottom). Each point is set in the middle of the z range where $\langle P_2 \rangle$ has been calculated.

Equilibration of this system was performed in a NPT ensemble, starting at 500 K and 400 bar. An initial temperature higher than that used for shorter chain samples was chosen in order to have a more fluid system. Once constant volume had been reached, the simulation proceeded for another 50 ns, then temperature was lowered by 50 K. This procedure was repeated until reaching 300 K. Then, the same method was applied for pressure decreasing, until the sample finally reached 300 K and 1 bar. The second step consisted in creating the links among the chains. For this purpose, we employed Avogadro [64], adding by hand short PDMS chains (about 10 units long) to the sample, and bonding their terminal residues to two different 80 units chains. Chemical bonds were established between methyls group of respective residues, so that, at the end, a new kind of bond, -CH_2-CH_2-, arose. For details about the adjustment in PDMS Force Field to take into account new interactions, see Chapter 5. Carrying on the linking among chains by hand, we did not manage to reach a high degree of reticulation: we simply added 6 short chains, so that each of the three macromolecules composing the sample was bonded to another one through two cross-linkers. As third step, through Outside, we
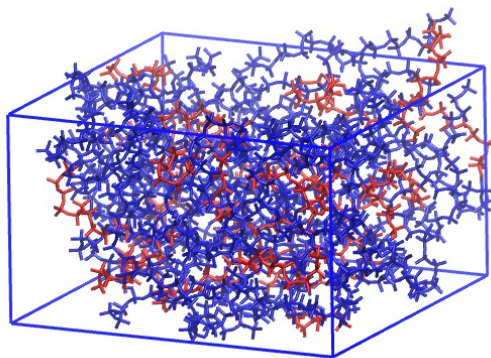
Figure 4.4: Perspective view of the cross-linked PDMS sample. Long 80 units chains are shown in blue, cross-linkers are shown in red.

replicated the system resulting from the previous step four times, then linked different replicas through other six cross-linkers. At the end of this time-consuming process, the system was made of 12 long chains and 30 cross-linkers, for a total of about 5000 atoms, a number big enough to build the surface we aimed at. A NPT equilibration of about 120 ns at 300 K was performed. A pressure of 1000 bar was applied along z direction, while 1 bar was applied to x and y direction, in order to flatten the sample (Figure 4.4). Once the cross-linked PDMS was ready, a 5CB sample made of 2000 molecules was placed on the top z face. Then, as made for the other systems, a NVT simulation at 300 K was launched for 50 ns. Figure 4.5 shows a sketch of the results we obtained. No significant differences can be observed with respect to PDMS20 sample for what concerns 5CB penetration through the PDMS surface. Some LC molecules have been still found inside the polymer bulk, even if in less extent than previous cases. One of the possible reasons is that the degree of reticulation was too low, causing the chains to be still too free to move. The limit of our work was that we did not use an automatic way to perform the cross-linking, so it resulted quite difficult to do it by hand, and an adequate degree of reticulation was not achieved. The most relevant aspect is the alternation along vertical direction, of zones with high and low orientational order, respectively. As for PDMS7 and PDMS20 samples, the 5CB layer immediately above PDMS underwent loss of orientational order. The overlying layer (around 100 Å) preserved it, while the upper part is disordered. Finally, in the top of the 5CB column, P_2 grows up again. Figure 4.6 shows the trend of order parameter $\langle P_2 \rangle$ computed along z direction from the bottom of the 5CB sample (0 Å, layer in contact with PDMS) to the top (200 Å, layer exposed to void).

As we can see, P_2 is really low nearby the surface, where the 5CB is isotropic, while greatly
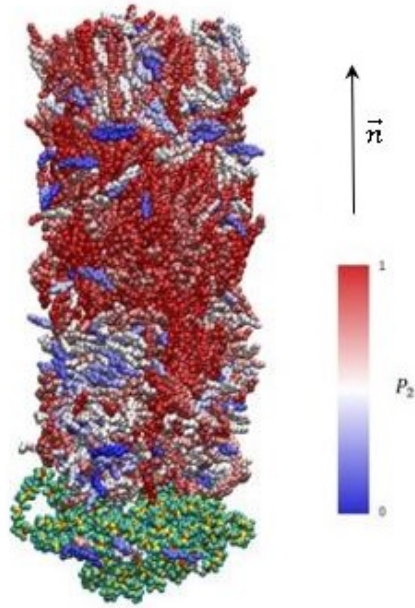
Figure 4.5: 5CB on cross-linked PDMS. For 5CB molecules, colour represents orientation, according to the palette on the right. Director $\vec{n}$ is represented by the black arrow.

grows around 100 Å height, assuming a value very similar to that obtained for nematic 5CB bulk at 300 K ($\langle P_2 \rangle$ = 0.596), than it decreases to about 0.47 in the top region. We do not clearly know if this effect is due to the fact that the 5CB sample employed in this case is two times bigger than those used previously. However evidence has been presented that a surface is able to affect LCs alignment only within few Å above the surface itself, as Roscioni et al. [4] found in their study about 5CB alignment on SAMs.
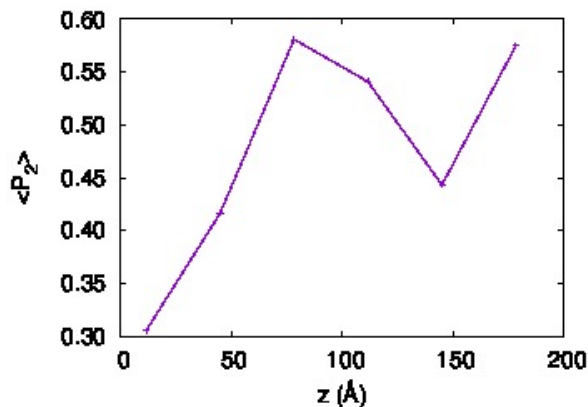

Figure 4.6: Order parameter $\langle P_2 \rangle$ computed along z axis for 5CB placed on cross-linked PDMS. Each point is set in the middle of the z range where $\langle P_2 \rangle$ has been calculated.

As last attempt, we decided to investigate the most flat PDMS surface possible, which is the one obtained by replicating a single straight polymeric chain along the two directions perpendicular to that of its extension. The sample we used is the same that has been described in Chapter 3, so here we will not explain again how we prepared it. We just remind that is was composed of 3 parallel layers, each one containing 17 chains with a length of 26 units. Mean and mean square roughness were computed (as described in Chapter 2 for PDMS7, PDMS13 and PDMS20 samples) in order to verify the smoothness of this surface (Figure 4.7), and values of 37.668 Å and 34.7278 Å^2 resulted, respectively. These values are quite lower than those obtained for PDMS7 and hugely lower than those computed for PDMS13 and PDMS20 (see Table 2.1).

In this system, the distance among chains is the lowest as to ensure atoms not to overlap.
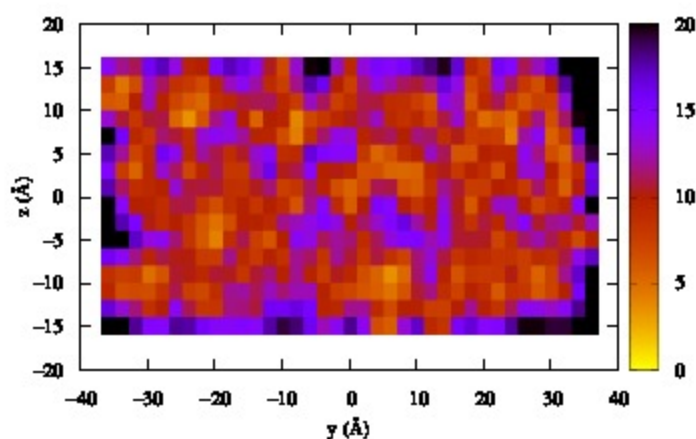
Figure 4.7: Surface coloured map for PDMS26. Depth is codified by the palette beside each plot: black is for maximum depth (20 Å in our case), yellow is for the minimum depth (0 Å).

Thus, degree of void is as little as possible. The 5CB sample used in this case was made of 2000 molecules. As usual, a NVT simulation at 300 K was performed, for about 30 ns, keeping PDMS backbones fixed in order to prevent the surface from changing during the run. Of course, it is not a completely realistic representation, since PDMS is used as an elastomer, hence chains are allowed to move at some extent. What we observed was that, this time, 5CB did not manage to penetrate PDMS: void spaces between chains are too little to allow 5CB transit across the surface (Figure 4.8).

For what concerns PDMS influence on 5CB orientation, we found that the anchoring on the surface is substantially planar, on the contrary of observations that result from experimental

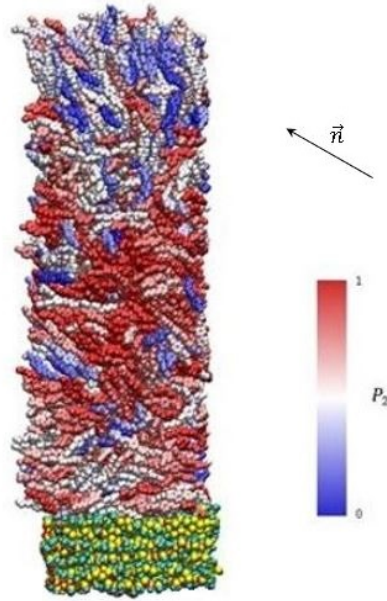**Figure 4.8:** 5CB on linear PDMS. For 5CB molecules, colour represents orientation, according to the palette on the right. Director $\vec{n}$ is represented by the black arrow.

works, where homeotropic anchoring occurs. As happens for the cross-linked PDMS case, orientation is not uniform along the 5CB column. Above the 5CB layer planar with respect to the PDMS surface, there is another layer where molecules are tilted and beyond this, we find a region where LCs are on average aligned within z axis. Figure 4.9 shows the trend of order parameter $\langle P_2 \rangle$ computed along z direction from the bottom of the 5CB sample (0 Å, layer in contact with PDMS) to the top (200 Å, layer exposed to void). What can be observed is that, inside the three regions we had located, $\langle P_2 \rangle$ is quite high (starting from bottom, 0.550 Å, 0.513 Å and 0.479 Å, respectively). These values are not much lower than that obtained for nematic 5CB bulk at 300 K ($\langle P_2 \rangle$ = 0.596). On the other hand, in between first and second region, and second and third region, $\langle P_2 \rangle$ falls down (0.374 Å and 0.224 Å, respectively), which means that orientational order is lost.

Another important aspect we purposed to investigate was the orientation of 5CB molecules in direct contact with PDMS surface with respect to the direction along which PDMS chains were aligned. Palermo et al. [5] had demonstrated that LCs orientation is not necessarily within the rubbing direction. In case of PMMA, 5CB molecules orient along the direction of chain stretch, but when PS is used, 5CB alignment is perpendicular to chains, due to the presence of phenyl groups. They in fact create sorts of rails stick-shaped molecules are induced to align with. It was our interest to study if any peculiar phenomenon could be observed for 5CB on
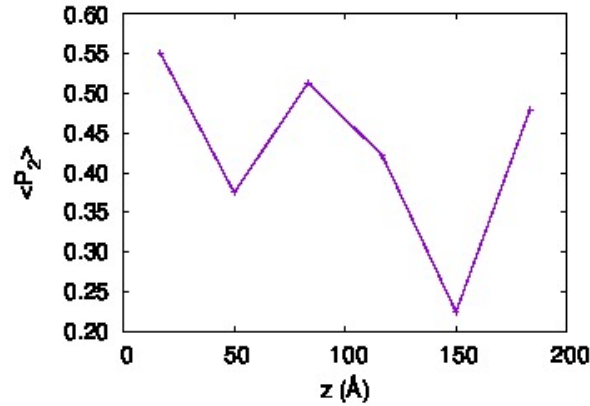
Figure 4.9: Order parameter $\langle P_2 \rangle$ computed along z axis for 5CB placed on linear PDMS. Each point is set in the middle of the z range where $\langle P_2 \rangle$ has been calculated.

a PDMS surface which had undergone rubbing (which is artificially obtained by employing straight chains). In order to get information about that, we considered a thin layer (10 Å) of 5CB lying on the PDMS surface, and then, with Outside, computed the average director of molecules belonging to this film, which was $\vec{n}$= (-0.039;-0.954;0.298). Since y component is one order of magnitude bigger than x component, and more than three times bigger than z component, then we can state that 5CB molecules are overall oriented along the y direction (Figure 4.10). PDMS chains, instead, are stretched along x direction. This means that 5CB alignment is perpendicular with respect to rubbing direction, as was found by Palermo et al. [5] for PS. In that article the cause was imputed by the presence of phenyl groups. Anyway, in the case of PDMS, side groups are methyls, which do not seem big enough to cause some steric effect as phenyls do. We do not clearly understand the reason why this phenomenon occurs.
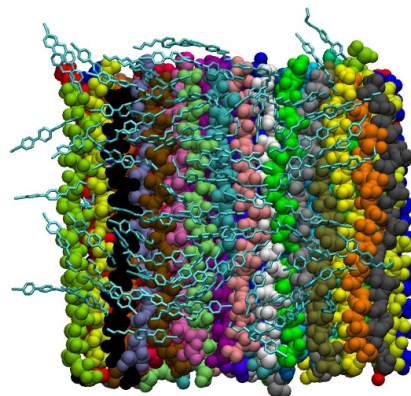

Figure 4.10: Top view showing the orientation of 5CB on the linear PDMS surface.

Chapter 5

Computation of Si-CH$_2$-CH$_2$-Si dihedral parameters via QM methods

Dealing with cross-linked rather than linear PDMS, for the simulation of a real solid surface, introduced a new type of bonds, those between two methyl groups (see Figure 1.26). Of course, parameters involving this bond were not present in Makrodimitri's FF [51], since it was developed to represent linear PDMS. As a consequence, the problem of obtaining these parameters arose. The parameters we needed were, in particular, those related to:

- bond stretching: CH$_2$-CH$_2$, Si-CH$_2$

- angle bending: Si-CH$_2$-CH$_2$, O-Si-CH$_2$, CH$_3$-Si-CH$_2$

- dihedral angles: Si-CH$_2$-CH$_2$-Si, Si-O-Si-CH$_2$, CH$_2$-CH$_2$-Si-CH$_3$, CH$_2$-CH$_2$-Si-O

The most accurate way to proceed would have been to calculate these values through QM computational techniques. However, this choice would have taken too much time and effort. For this reason, we decided to get missing parameters from others works, if available. Unfortunately, no FF for cross-linked PDMS has been developed yet, so we looked for works on molecules where the bonds we were interested in were present. Regarding stretching CH$_2$-CH$_2$ and Si-CH$_2$, and bending Si-CH$_2$-CH$_2$ parameters, we found in the work of Roscioni et al. [4] about SAMs. There, alkyl chains were attached to silica, hence Si-CH$_2$ bonds were formed. We did not find bending O-Si-CH$_2$ and CH$_3$-Si-CH$_2$ parameters anywhere else, so we assumed that they could be reasonably considered to be equal to O-Si-CH$_3$ and CH$_3$-Si-CH$_3$, respectively (those already available in Makrodimitri's FF). Dihedral angles Si-O-Si-CH$_2$, CH$_2$-CH$_2$-Si-CH$_3$ and CH$_2$-CH$_2$-Si-O parameters were instead taken from the universal Force Field MM2

[53]. In such a kind of FF, parameters are listed only specifying atoms involved in a certain interaction, without taking into account that this interaction occurs inside a well defined chemical system, hence same atoms could behave very differently depending on atoms they are bound to. In Table 5.1, values for the parameters we needed to simulate cross-linked PDMS are reported.

The only interaction whose parameters were not taken from another Force Field, but calcu-

bond stretching	k_l (kcal mol^{-1} Å^{-2})	l_0 (Å)	
CH$_2$-CH$_2$ [4]	303.1	1.535	
Si-CH$_2$ [4]	219.4	1.915	
bond bending	k_θ (kcal mol^{-1} rad^{-2})	θ_0 (°)	
Si-CH$_2$-CH$_2$ [4]	63.210	110.630	
O-Si-CH$_2$ [51]	50.000	109.5	
CH$_3$-Si-CH$_2$ [51]	50.000	109.5	
dihedral angle	k_ϕ (kcal mol^{-1})	n	g (°)
Si-O-Si-CH$_2$ [53]	0.100	3	0.0
CH$_2$-CH$_2$-Si-CH$_3$ [53]	0.167	3	0.0
CH$_2$-CH$_2$-Si-O [53]	0.167	3	0.0

Table 5.1: Missing parameters for cross-linked PDMS Force Field.

lated by our own, is the Si-CH$_2$-CH$_2$-Si torsion. These parameters were obtained throughout a fitting of energy values computed with QM techniques employing the software *Gaussian* (09 version) [65]. First of all, we built the molecule on which performing counts. Since QM calculations are much more computationally expensive than MD ones, we could not take into account the whole cross-linked PDMS system we then used in MD simulations. In general, for little molecules, the entire molecular system is taken into account. However, for large systems such as polymers, this is not possible or, anyway, it would be too time demanding. The solution is to consider a model molecule, large enough to reproduce molecular features quite well and, at the same time, small enough to ensure affordable computational costs. Figure 5.1 shows the model, representing cross-linked PDMS, we developed to perform calculations with Gaussian [65]. It contained, obviously, the Si-CH$_2$-CH$_2$-Si sequence of atoms we wanted to compute torsion parameters for. Then, substituents were added to silicons in order to create steric hindrance around the dihedral angle. In Figure 5.1, the left part of the molecule repre-

sents a little segment (3 units) of linear PDMS, while the right part represents the vynil tail of a cross-linker. This molecule was generated by hand using Molden [66], a program for molecular representation. Then, always with Molden, a geometry optimization was performed through MM calculations, using the MM2 Force Field.

Once equilibrium structure was obtained, various geometries were generated, starting from
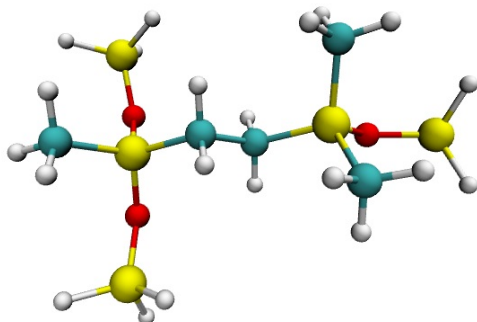

Figure 5.1: Model molecule of cross-linked PDMS for QM calculations. Silicons are shown in yellow, oxygens in red, carbons in blue, hydrogens in white.

the equilibrium structure, by simply rotating the Si-CH$_2$-CH$_2$-Si dihedral angle of 10° each time, from 0° to 180°. All the other degrees of freedom were left unchanged with respect to equilibrium structure. At this point, for each geometry, we performed energy minimization with Gaussian. At the beginning, a wB97XD/cc-pVTZ level of theory was chosen, according to the work of Roscioni et al. [4], where the calculation of torsional parameters for SAMs were computed with that level of theory. However, we realized it was too slow (more than a week was required for a single geometry optimization), so we decided to move to a faster method. At the beginning, a minimization at pm6 level of theory was performed, then we employed the more accurate B3LYP/6-31G* on the optimized geometries obtained with pm6. This method is fairly rougher than the wB97XD/cc-pVTZ adopted by Roscioni et al. [4], but it allows very fast calculations, while still being accurate enough, for our purpose. Thus we preferred it to a more precise but slower method. Since our molecule was symmetric with respect to the plane containing the central CH$_2$-CH$_2$ bond, we did not need to compute the energy for geometries with the Si-CH$_2$-CH$_2$-Si dihedral ranging from -180° to 180° (or, analogously, from 0° to 360°). The energy profile is expected to be symmetric too. This is the reason why we computed energy only for positive dihedrals from 0° to 180°. Optimizations were carried out by performing a relaxed scan, which means keeping Si-CH$_2$-CH$_2$-Si dihedral angle fixed, while allowing all the other molecular parameters to change. The energy trend obtained with

Gaussian, against Si-CH$_2$-CH$_2$-Si dihedral angle, is shown in Figure 5.2 (the lowest energy, which was that associated to 180°, was set to 0).
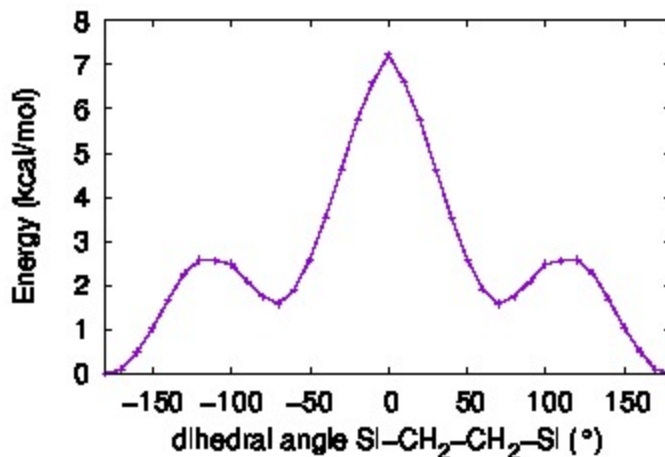

Figure 5.2: Energy calculated with Gaussian plotted against dihedral angle Si-CH$_2$-CH$_2$-Si.

Energies values for optimized geometries obtained with Gaussian are overall, i.e. they include all contributes to the total potential:

$$E_{QM} = E_{stretch} + E_{bend} + E_{tors,tot} + E_{non-bond}$$
$$= E_{stretch} + E_{bend} + (E_{tors,central} + E_{tors,others}) + E_{non-bond}$$

(5.1)

where E_{QM} is the energy calculated by Gaussian, $E_{tors,tot}$ is the total torsional energy, while $E_{tors,central}$ and $E_{tors,others}$ are torsional energies associated to the Si-CH$_2$-CH$_2$-Si dihedral and all the other dihedrals, respectively. Since we were interested in Si-CH$_2$-CH$_2$-Si torsional potential only, we had to subtract from total energy all other interactions: stretching, bending, non-bonded and other torsional (different from the one we are investigating) ones.

$$E_{tors,central} = E_{QM} - E_{stretch} - E_{bend} - E_{tors,others} - E_{non-bond}$$

(5.2)

At this purpose, we launched, for each optimized geometry, a so-called "run 0" MD simulation (with NAMD). This is not a real simulation, since it only computes the energy for the initial configuration, and is obtained by setting the number of steps to be simulated equal to 0. Operative conditions inserted in NAMD input file are neglected, so it does not mind what they are. Through the Force Field given as input, NAMD calculates each type of interaction separately. Regarding the unknown Si-CH$_2$-CH$_2$-Si torsion, its force constant was set to 0 in the parame-

ter file. In this way, this degree of freedom did not contribute to overall energy computed by NAMD, while it did in QM calculations. In conclusion, molecular energy arisen from "run 0" simulation differed from quantum mechanics energy by the torsional potential energy related to Si-CH$_2$-CH$_2$-Si dihedral angle.

$$E_{MD} = E_{stretch} + E_{bend} + E_{tors,others} + E_{non-bond}. \tag{5.3}$$

Subtracting E_{MD} to E_{QM}, we obtained, for each geometry, the torsional energy $E_{tors,central}$:

$$E_{tors,central} = E_{QM} - E_{MD}. \tag{5.4}$$

However, before doing that, it was necessary to refer energies of all geometries to the same energy, taken as 0. Since $E_{QM}(180°)$ was the lowest one, we chose it as reference value, in order to have other QM energies positive. Consequently, also the other kinds of energy were obtained subtracting to the original value the one corresponding to geometry with $\phi_{central} = 180°$. Table 5.2 shows various kinds of energy, both calculated with Gaussian and NAMD, for each geometry.

At this point, we calculated $E_{tors,central}$ with Equation 5.4 and then plotted these values against the dihedral angle $\phi_{central}$, as shown in Figure 5.3. As it can be seen, values at 20° (and -20°), 90° (and -90°) and 100° (and -100°) appear too low with respect to the trend of energy. The reason is that, for these geometries, atoms lie in a configuration that causes other types of interaction to be very strong. Hence, total energy is much greater than that of neighbour geometries. Since these geometries are predicted not to be explored by the molecule, due to their too high energy, it is reasonable to discard them for the fitting of torsional potential.
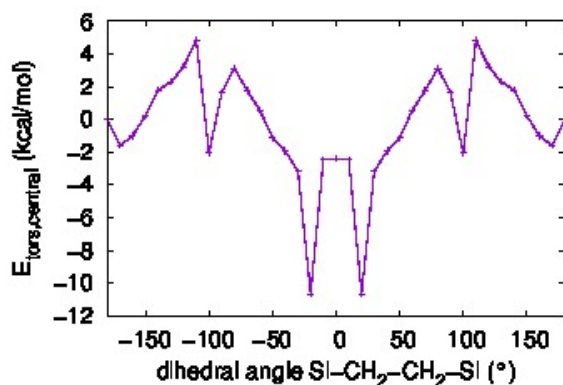

Figure 5.3: Torsional potential trend with respect to $\phi_{central}$ including all points of Table 5.2.

$\phi_{central}$ (°)	$E_{QM}\left(\frac{kcal}{mol}\right)$	$E_{MD}\left(\frac{kcal}{mol}\right)$	$E_{stretch}\left(\frac{kcal}{mol}\right)$	$E_{bend}\left(\frac{kcal}{mol}\right)$	$E_{tors,others}\left(\frac{kcal}{mol}\right)$	$E_{non-bond}\left(\frac{kcal}{mol}\right)$
0	7.2239	9.6228	0.3341	10.2970	2.2394	-3.2475
10	6.6014	9.0489	0.2796	10.0504	2.0466	-3.3277
20	5.7398	16.3939	0.2224	17.3900	2.0181	-3.2365
30	4.6298	7.8103	0.1700	11.6571	-0.7716	-3.2451
40	3.5404	5.4643	0.1749	6.3179	2.2236	-3.2520
50	2.5891	3.7212	0.1335	4.7735	2.1391	-3.3248
60	1.8995	1.3406	0.1269	2.9838	1.5221	-3.2921
70	1.5738	-0.1742	0.1243	2.2644	0.5952	-3.1580
80	1.7501	-1.3649	0.1552	1.1172	0.1381	-2.7753
90	2.0890	0.4554	0.1877	1.0618	1.3501	-2.1441
100	2.4812	4.5274	0.1002	4.8934	1.1549	-1.6210
110	2.5515	-2.2700	0.1612	1.4151	-2.2281	-1.6181
120	2.5722	-0.6415	0.2277	-0.5291	1.1426	-1.4826
130	2.2641	-0.0126	0.2029	-0.5277	1.4879	-1.1755
140	1.6824	-0.1166	0.1565	-0.8602	1.5352	-0.9480
150	1.0291	0.7930	0.0924	-0.6705	2.0218	-0.6507
160	0.4851	1.4938	-0.0222	0.3429	1.5085	-0.3353
170	0.0853	1.6864	-0.0256	0.0484	1.9038	-0.2401
180	0.0000	0.0000	0.0000	0.0000	0.0000	0.0000

Table 5.2: Energy values computed with Gaussian and NAMD for all the geometries analyzed.

As last step, the curve obtained was fitted with Gnuplot [67] using the following equation:

$$
\begin{aligned}
E_{tors,central}(\phi) =& k_1(1 + \cos\phi) + k_2[1 + \cos(2\phi - 180°)] + k_3(1 + \cos 3\phi) \\
&+ k_4[1 + \cos(4\phi - 180°)] + k_5(1 + \cos 5\phi) + k_6[1 + \cos(6\phi - 180°)]
\end{aligned}
\tag{5.5}
$$

where k_n, with n from 1 to 6, were the coefficients (expressed in kcal/mol) to be optimized in order to perform the fitting. The function was chosen according to NAMD representation of torsional potential, using the highest number of cosine functions allowed by this software (i.e. six). Figure 5.4 shows the curve obtained. As it can be seen, it works well except for ϕ near 180°. Of course, a better fitting would have needed with more than six terms, but this was the best we managed to do with the constraint we were imposed by NAMD.

The values obtained for the coefficients k_n are:

$$k_1 = \text{-1.78086 kcal/mol}$$

$$k_2 = 2.89047 \text{ kcal/mol}$$

$$k_3 = 0.702548 \text{ kcal/mol}$$

$$k_4 = -0.675114 \text{ kcal/mol}$$

$$k_5 = -0.0863571 \text{ kcal/mol}$$

$$k_6 = -0.366384 \text{ kcal/mol}$$

which have been included in the Force Field for cross-linked PDMS, as described in Chapter 4.
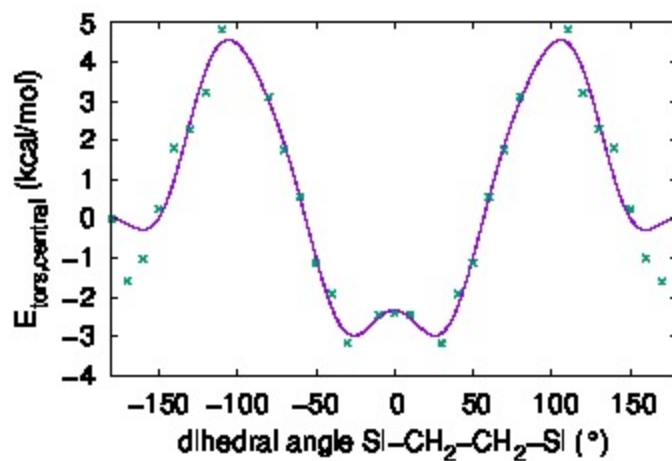

Figure 5.4: Fitting equation (purple line) of points calculated (green crosses) for torsional potential of Si-CH$_2$-CH$_2$-Si dihedral angle.

Chapter 6

Conclusions

In this dissertation I reported my work about the investigation on PDMS I carried on at the liquid crystal group at *"Toso Montanari"* department of the University of Bologna. The principal aim of my research was to study the features of the interaction between this polymer and the best known liquid crystal molecule, 5CB. In particular, we aimed at understanding the origin of the homeotropic anchoring of 5CB on a PDMS surface, as some experimental works report [6, 7, 8]. The methodology I employed for my investigation was that of Molecular Dynamics simulations. As regards to parameterization of energy, the Force Field developed by Makrodimitri [51] was employed. First of all, we focused on the characterization of PDMS, computing its radial distribution function, end-to-end distance, radius of gyration and dihedral distribution, analyzing how chain length affects bulk structure at ambient conditions (300K and 1bar). At the same time, we also computed surface roughness for PDMS samples with different chain length, and we found that a greater length induces a rougher surface, since molecules can not simply achieve a good degree of packing.

In order to get information about surface energy of PDMS, which constitutes, together with morphological aspects, the key for understanding the interaction with 5CB, we carried out a study on its surface tension. For this purpose, we investigated the evolution in shape of an initially cubic water droplet (modeled with TIP3P [63]) placed on a PDMS surface. When a mobile short chain (7 or 20 units) polymeric system was employed, we observed that a partial penetration of the droplet inside PDMS occurred, underlining that, if not cross-linked, PDMS is much more a liquid than a solid material. However, no dissolution of water was observed: they formed a compact mass that, when isolated, revealed a nearly spherical shape. Repeating the simulation employing a PDMS surface where backbones had been fixed, water penetration

did not occur any more, and the computation of contact angle gave a value of 133 °, typical of a strongly hydrophobic substance, as we expected from experimental data [8].

For what concerns 5CB interaction with a PDMS surface, we observed that, with very short chains (7 units), some of them detached from the surface, causing an effective dissolution in 5CB. At the same time, LC molecules penetrated inside the polymeric surface. Increasing the chain length to 20 units, dissolution phenomenon disappeared, but 5CB penetration inside PDMS still occurred. These first attempts showed us that linear PDMS was not suitable for our study. We then performed simulations on a cross-linked PDMS slab [40], but even in this case, 5CB molecules managed to penetrate the polymer to some extent, and the homeotropic alignment predicted by experimental works was not observed. Instead, a loss of orientational order resulted nearby the PDMS surface. One possible reason of this discrepancy with experimental evidence could be the low degree of reticulation; our sample was prepared by employing a ratio PDMS:cross-linkers which is less than half of that used for conventional PDMS elastomer [68]. Our system could be not enough entangled to reproduce what happens for the commercial PDMS (Sylgard 184) used in real experiments [69]. In particular, too mobile chains could be the cause of 5CB penetration below the surface. On the other hand, employing a straight-chain sample with fixed backbones, it was like dealing with a completely solid surface, which once again did not faithfully reproduce real features observed for the PDMS elastomer. Since chains were very close to each others, penetration of 5CB did not occur, but this time the flat surface induced planar anchoring of LC molecules, with the preferential orientation direction perpendicular to the direction of extension of chains. At this stage, it is not yet clear why this phenomenon occurs. In fact, it does not seem to us to observe any particular morphological feature that could induce this kind of alignment, on the contary Palermo et al. found for PS [5]. In conclusion, what we have reported in this dissertation is just the top of an iceberg that has still to be explored. A quite detailed characterization of PDMS has been already done, partly in this work, but a huge effort must still be done to clearly understand the reasons of homeotropic alignment of 5CB nearby a PDMS surface. At this purpose, both energetic and morphological aspects must be taken into account. Concerning the second ones, we found what an important role surface structure has, as testified by different results obtained starting from different samples. Certainly, MD simulations represent a very powerful mean of investigation for such complex issues, allowing the researcher to catch details that would be otherwise undetectable.

Bibliography

[1] G. Tiberio et al. "Towards in silico liquid crystals. Realistic transition temperatures and physical properties for n-cyano-biphenyls via molecular dynamics simulations". In: ChemPhysChem 10 (2009), pp. 125–136.

[2] S. H. Lee, S. L. Lee, and H. Y. Kim. "Electro-optic characteristic and switching principle of a nematic liquid crystal cell controlled by fringe-field switching". In: Applied Phyics Letters 73 (1998).

[3] O. M. Roscioni et al. "Predicting the anchoring of liquid crystals at a solid surface: 5-cyanobiphenil on crystobalite and glassy silica surfaces of increasing roughness". In: Langmuir 29 (2013), pp. 8950–8958.

[4] O. M. Roscioni, L. Muccioli, and C. Zannoni. "Predicting the conditions for homeotropic anchoring of liquid crystals at a soft surface. 4-n-Pentyl-4-cyanobiphenyl on alkylsilane self-assembled monolayers". In: Applied Materials Interfaces 9 (2017), pp. 11993–12002.

[5] M. F. Palermo et al. "Is the alignment of nematics on a polymer slab always along the rubbing direction? A molecular dynamics study". In: Liquid Crystals 44 (2017), pp. 1764–1774.

[6] D. Ahn et al. "Control of liquid crystal pretilt angles by using organic/inorganic hybrid interpenetrating networks". In: Optic Express 17 (2009), pp. 16603–16612.

[7] H. J. Lee et al. "Orientational control of liquid crystal molecules by re-formed poly(dimethylsiloxane) alignment layer via ion-beam irradiation". In: Materials Chemistry and Physics 126 (2001), pp. 628–631.

[8] Y. Xia et al. "Better actuation through chemistry: using surface coating to create uniform director fields in nematic liquid crystal elastomers". In: Applied Materials Interfaces 8 (2016), pp. 12446–12472.

[9]   C. Zannoni. "From idealized to predictive models of liquid crystals". In: Liquid Crystals (2018).

[10] C. J. Cramer. Essentials of computational chemistry. Theories and models. New York: Wiley, 2004.

[11] J. M. Haile. Molecular dynamics simulation. New York: Wiley, 1992.

[12] J. C. Phillips et al. "Scalable molecular dynamics with NAMD". In: Journal of Computational Chemistry 26 (2005), pp. 1781–1802.

[13] D. Frenkel and B. Smit. Understanding molecular simulations. 2nd ed. San Diego: Academic Press, 2001.

[14] H. C. Anderson. "RATTLE: a velocity version of the SHAKE algorithm for molecular dynamics calculations". In: Journal of Computational Physics 52 (1983), pp. 24–34.

[15] URL: http://isaacs.sourceforge.net/phys/rdfs.html.

[16] URL: https://commons.wikimedia.org/wiki/File:Simulated_ Radial_Distribution_Functions_for_Solid,_Liquid,_and_ Gaseous_Argon.svg.

[17] URL: https://commons.wikimedia.org/wiki/File:Periodic_ Boundary_Conditions_in_2D.png.

[18] G. Bussi, D. Donadio, and Parrinello M. "Canonical sampling thorugh velocity rescaling". In: The Journal of Chemical Physics 26 (2007), p. 014101.

[19] H. J. C. Berendsen et al. "Molecular dynamics with coupling to an external bath". In: The Journal of Chemical Physics 81 (1984), pp. 3684–3690.

[20] URL: https://ipfs.io/ipfs/ QmXoypizjW3WknFiJnKLwHCnL72vedxjQkDDP1mXWo6uco/wiki/ Dihedral_angle.html.

[21] D. Wolf et al. "Exact method for the simulation of coulombic systems by spherically truncated, pairwise r^{-1}" summation". In: The Journal of Physical Chemistry 110 (1999), p. 8254.

[22] adapted from. URL: http://www.chem.ucalgary.ca/courses/350/ mechanistic_etext/Ch02/ch2-2-1.html.

[23] C. R. Barber. "The sublimation temperature of carbon dioxide". In: British Journal of Applied Physics 17 (1966), p. 1651.

[24] adapted from. URL: `http : / / myforgottencoast . com / consider - this - phase - diagram - for - carbon - dioxide / consider - this - phase - diagram - for - carbon - dioxide - unique - phase - diagrams - chemistry-libretexts/`.

[25] URL: `https://www.tulane.edu/~sanelson/eens211/proplight.htm`.

[26] URL: `https://en.wikipedia.org/wiki/Liquid_crystal`.

[27] S. Ishihara et al. "The effect of rubbed polymer films on the liquid crystal alignment". In: Liquid Crystals 4 (1989), pp. 669–675.

[28] In: (). URL: `https : / / en . wikipedia . org / wiki / 4 - Cyano - 4 ' 27 - pentylbiphenyl`.

[29] G. Luckhurst and G. W. Gray. The molecular physics of liquid crystals. London: Academic Press, 1979.

[30] W. den Boer. Active matrix liquid crystal displays. Amsterdam: Newnes, 2005.

[31] URL: `http://www.wtec.org/loyola/dsply_jp/c4_s3.htm`.

[32] adapted from. URL: `https : / / www . pcworld . com / article / 251988 / tablets/digital-displays-explained.html?page=4`.

[33] adapted from. URL: `https://www.winstar.com.tw/technology/stn.html`.

[34] URL: `https : / / warwick . ac . uk / fac / sci / chemistry / research / rourke/rourkegroup/mesogens/`.

[35] S. K. Pal et al. "Triphenylene-based discotic liquid crystals: recent advances". In: Liquid Crystals 40 (2013).

[36] A. N. Cammidge. "The effect of size and shape variation in discotic liquid crystals based on triphenylene cores". In: Philosophical Transactions of the Royal Society of London A 364 (2006). adapted from, pp. 2697–2708.

[37] L. Y. Zhang et al. "Research progress of cholesteric liquid crystals with broadband re-
      flection characteristics in application of intelligent optical modulation materials". In:
      Chinese Physics B 25 (2016). adapted from, p. 96101.

[38] W. Zhang et al. "Unconventional high-performance laser protection system based
      on dichroic dye-doped cholesteric liquid crystals". In: Scientific Reports 7 (2017),
      p. 42955.

[39] URL: https://it.wikipedia.org/wiki/Polidimetilsilossano.

[40] N. Bosq et al. "Melt and glass crystallization of PDMS and PDMS silica nanocompos-
      ites". In: Physical Chemistry Chemical Physics 16 (Mar. 2014).

[41] U. Gaur and B. Wunderlich. "The glass transition temperature of polyethylene". In:
      Macromolecules 13 (1980), pp. 445–446.

[42] H. S. Bu, S. Z. D. Cheng, and B. Wunderlich. "Addendum to the thermal properties of
      polypropylene". In: Macromolecular Rapid Communications 9 (1988), pp. 75–77.

[43] M. Kosaki, K. Sugiyama, and M. Ieda. "Ionic jump jistance and glass transition of
      polyvinyl chloride". In: Journal of Apllied Physics 42 (1971), p. 3388.

[44] I. M. Ward. "The temperature dependence of extensional creep in polyethylene tereph-
      thalate". In: Polymer 5 (1964), pp. 59–66.

[45] D. A. Chang-Yen, R. K. Eich, and B. K. Gale. "A monolithic PDMS waveguide system
      fabricated using soft-lithography techniques". In: Journal of Lightwave Technology 23
      (2005), pp. 2088–2093.

[46] Y.   Xia   and   G.   M.   Whitesides.   "Soft   lithography".   In:
      Annual Review of Materials Research 28 (1998), pp. 153–184.

[47] R. M. Sok, H. J. C. Berendsen, and van Gunsteren W. F. "Molecular dynamics
      simulation of the transport of small molecules across a polymer membrane". In:
      Journal of Chemical Physics 96 (1992), p. 4699.

[48] A. L. Frischknecht and J. G. Curro. "Improved united atom force field for
      poly(dimethylsiloxane)". In: Macromolecules 36 (2003), pp. 2122–2129.

[49] H. Sun. "COMPASS: an ab initio Force-Field optimized for condensed-phase
      applications. Overview with details on alkane and benzene compounds". In:
      The Journal of Physical Chemistry B 102 (1998), pp. 7338–7364.

[50] J. S. Smith, O. Borodin, and G. D. Smith. "A quantum chemistry based Force Field for poly(dimethylsiloxane)". In: The Journal of Physical Chemistry B 108 (2004), pp. 20340–20350.

[51] Z. A. Makrodimitri, R. Dohrn, and I. G. Economou. "Atomistic simulation of poly(dimethylsiloxane): Force Field development, structure, and thermodynamic properties of polymer melt and solubility of n-alkanes, n-perfluoroalkanes, and noble and light gases". In: Macromolecules 40 (2007), pp. 1720–1729.

[52] J. H. Suh et al. "Control of surface anchoring properties of liquid crystal by thermo-transfer printing of siloxane oligomers". In: Liquid Crystals 42 (2015), pp. 1236–1242.

[53] T. R. Stouch and Y. C. Martin. "A giant's shoulders: a perspective from professor Norman L. Allinger". In: Journal of Computer-Aided Molecular Design 25 (2011), pp. 293–294.

[54] L. Martínez et al. "Packmol: a package for building initial configurations for molecular dynamics simulations". In: Journal of Computational Chemistry 30 (2009), pp. 2157–2164.

[55] W. Humphrey, A. Dalke, and K. Schulten. "VMD - Visual Molecular Dynamics". In: Journal of Molecular Graphics 14 (1996), pp. 33–38.

[56] A. Rohatgi. WebPlotDigitizer. 4.1. Austin, Texas, USA: Newnes, 2018. URL: `https://automeris.io/WebPlotDigitizer`.

[57] E. P. Degarmo, J. T. Black, and R. A. Kohser. Materials and processes in manufacturing. 9th ed. Wiley, 2003, p. 223.

[58] URL: `https://it.wikipedia.org/wiki/Tensione_superficiale`.

[59] URL: `https://flywithmeproductions.com/blog/?attachment_id=23775`.

[60] URL: `https://en.wikipedia.org/wiki/Surface_tension`.

[61] A. E. Ismail et al. "Interfacial structure and dynamics of ailoxane aystems: PDMS-vapor and PDMS-water". In: Macromolecules 42 (2009), pp. 3186–3194.

[62] N. Meyer et al. "Rotational and translational dynamics of the SPC/E water model". In: Journal of Molecular Liquids (2018).

[63] P. Mark and L. Nilsson. "Structure and dynamics of the TIP3P, SPC, and SPC/E water models at 298 K". In: Journal of Physical Chemistry A 105 (2001), pp. 9954–9960.

[64] M. D. Hanwell et al. "Avogadro: an advanced semantic chemical editor, visualization and analysis platform". In: Journal of Cheminformatics 4 (2012), p. 17.

[65] M. J. Frisch et al. Gaussian09 Revision E.01. "Gaussian Inc. Wallingford CT 2009".

[66] G. Schaftenaar, E. Vlieg, and G. Vriend. "Molden 2.0: quantum chemistry meets proteins". In: Journal of Computer-Aided Molecular Design 31 (2017), p. 789.

[67] T. Williams and C. Kelley. "Gnuplot 4.6: an interactive plotting program". In: (2013). URL: http://gnuplot.sourceforge.net/.

[68] URL: http://www.farnell.com/datasheets/1599873.pdf?_ga=2.118270345.1266334474.1537731285-1991628630.1537731285.

[69] I. D. Johnston et al. "Mechanical characterization of bulk Sylgard 184 for microfluidics and microengineering". In: Journal of Micromechanics and Microengineering 24 (2014).